A fundamental, new solar process has been introduced, the **STEP** process, which efficiently removes carbon from the atmosphere and generates the staples needed by society, ranging from fuels, to metals, bleach and construction materials, at high solar efficiency and without carbon dioxide generation.
By using the full spectrum of sunlight, **STEP** captures more solar energy than the most efficient solar cell or photoelectrochemical processes.
*-**STEP**'s concentrated sunlight drives new high temperature molten CO_2-free syntheses at industrial production rates.*

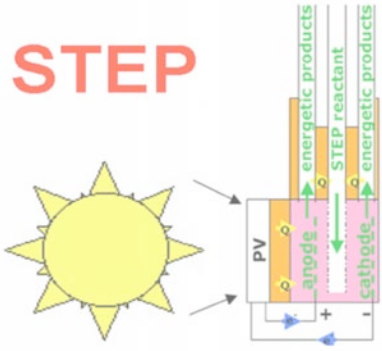

Included are Technical Write-ups of:

1) STEP CO_2 converted to carbon nanofibers 2015

2) STEP Fertilizer 2014

3) STEP Fuels 2014/15

4) STEP Iron 2013

5) STEP Cement 2012

6) STEP 2011 -Includes theory, solar efficiency, and individual STEP processes for Fuels, Metals, Bleach and Desalinization.

7) The import of electrochemistry in solar energy conversion Nature cover article 1987

Further information available at Licht research group sites:
http://home.gwu.edu/~slicht/index.html
http://chemistry.columbian.gwu.edu/stuart-licht

The **Licht research group** has taken on the challenge of *a comprehensive solution to climate change*. We're working towards changing today's fossil fuel, to a renewable chemical economy, replacing the largest greenhouse gas emitters, including iron & fuel production, by new, inexpensive, solar, CO_2-free, chemistries.

NANO LETTERS

Letter

pubs.acs.org/NanoLett

One-Pot Synthesis of Carbon Nanofibers from CO_2

Jiawen Ren,[†] Fang-Fang Li,[†] Jason Lau,[†] Luis González-Urbina,[†] and Stuart Licht*[,†]

[†]Department of Chemistry, The George Washington University, Washington, DC 20052, United States

Supporting Information

ABSTRACT: Carbon nanofibers, CNFs, due to their superior strength, conductivity, flexibility, and durability have great potential as a material resource but still have limited use due to the cost intensive complexities of their synthesis. Herein, we report the high-yield and scalable electrolytic conversion of atmospheric CO_2 dissolved in molten carbonates into CNFs. It is demonstrated that the conversion of $CO_2 \rightarrow C_{CNF} + O_2$ can be driven by efficient solar, as well as conventional, energy at inexpensive steel or nickel electrodes. The structure is tuned by controlling the electrolysis conditions, such as the addition of trace transition metals to act as CNF nucleation sites, the addition of zinc as an initiator and the control of current density. A less expensive source of CNFs will facilitate its adoption as a societal resource, and using carbon dioxide as a reactant to generate a value added product such as CNFs provides impetus to consume this greenhouse gas to mitigate climate change.

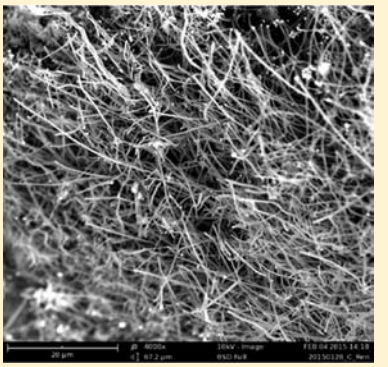

KEYWORDS: *Carbon nanofibers, carbon composites, carbon capture, climate change, solar energy*

The synthesis of nano carbon fibers and modified CNFs has been of increasing interest, with applications ranging from capacitors, Li-ion batteries, and electrocatalysts to the principal component of lightweight, high strength building materials; today, CNF demand is mainly limited by the complexity and cost of the synthetic process, which requires 30−100-fold higher production energy compared to aluminum.[1,2] Carbon nanofibers have been synthesized from a variety of materials including pitch, rayon, polyacrylonitrile,[3] solid carbon materials,[4,5] acetone,[6] or hydrocarbon gases,[7,8] by employing electrospinning/carbonization, chemical vapor deposition (CVD), arc/plasma techniques,[9,10] etc. Recent interests are focusing on renewable feedstocks, i.e., ligin and cellulose,[11,12] rather than conventional chemicals from the natural gas or petroleum industry. Here, we synthesize a valuable commodity, CNFs, directly from atmospheric CO_2 in a one-pot synthesis. The "production of CNFs by electrolysis in molten lithium carbonate is impossible" according to a prior report in the literature.[13] Yet here, we present exactly that a high yield process for the electrolytic conversion of CO_2, dissolved in molten carbonates, directly to CNFs at high rates using scalable, inexpensive nickel and steel electrodes. The structure is tuned by controlling the electrolysis conditions, such as the addition of trace nickel to act as CNF nucleation sites, the concentration of added oxide, the addition of zinc as an initiator, and the control of current density. CO_2 is a greenhouse gas that impacts climate change.[14,15] CNFs formed from CO_2, can contribute to lower greenhouse gases for example by consuming, rather than emitting CO_2, and by providing a carbon composite material that can be used as an alternative to steel, aluminum, and cement whose productions are associated with massive CO_2 emissions.[16−18] Carbon composites will further decrease emissions by facilitating both wind turbines and lightweight, low-carbon-footprint transportation.[19]

Prior to the recognition of a variety of unique carbon nanoscopic structures such as fullerenes, nanotubes, and nanofibers, the reduction of carbonates to (macroscopic) carbons in inorganic molten electrolytes from hydroxides and a barium chloride/barium carbonate melt was recognized as early as the late 1800s.[20] There are few known routes to the synthesis of carbon nanofibers, and the existing syntheses are energy, equipment, time, and cost-extensive. The electrochemical synthesis of CNFs has not been widely explored. Solid carbon electrodes have been electrolytically converted to nanostructures such as nanotubes in molten halide solutions via alkali metal formation, intercalation into, and exfoliation of the carbon.[5] Instead of the conversion of solid carbon, the rate of the direct reduction of CO_2 studied with carbon and platinum electrodes is limited by the low solubility of CO_2 in molten halides and requires high (15 atm) CO_2 pressure. This conversion is also accompanied by corrosion of the electrodes.[21,22] A study of 5−10% Li_2CO_3 in molten chloride concluded that "production of CNTs and nanofibers by electrolysis in molten lithium carbonate is impossible" because "reduction and carbon deposition occurred by Li discharge and intercalation into the cathode".[13] That assessment was correct but did not anticipate the alternative Ni nuclei growth mechanism with zinc initiated paths from molten Li_2CO_3 observed here.

Materials and Methods. Experimental details of the solar thermal electrochemical process, STEP, synthesis of a variety of

Received: June 18, 2015
Revised: July 16, 2015

DOI: 10.1021/acs.nanolett.5b02427
Nano Lett. XXXX, XXX, XXX−XXX

Scheme 1. Molten Carbonate Electrolysis Pathways Converting CO_2 Leading to a High Yield, Uniform CNF Product

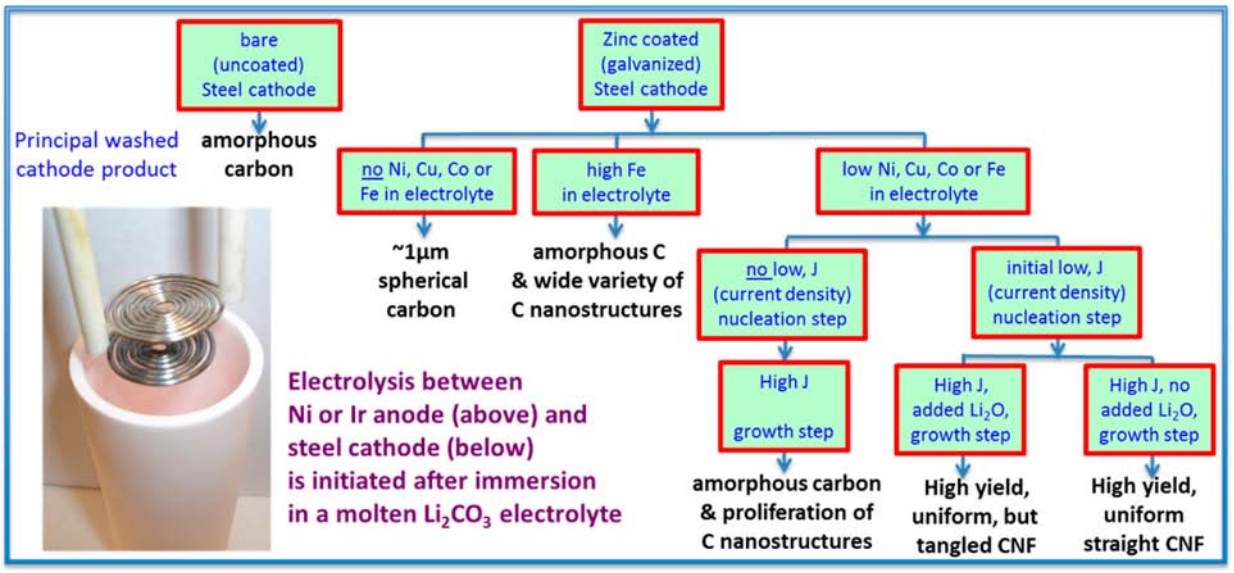

societal staples and carbon capture have been detailed in previous publications.[16−18,23−29] This study focuses primarily on the STEP for carbon electrochemical reactor component to form a high-yield CNF component. Barium carbonate (Alfa Aesar, 99.5%), lithium carbonate (Alfa Aesar, 99%), lithium oxide (Alfa Aesar, 99.5%), and calcium carbonate (Alfa Aesar, 98%) are combined to form various molten electrolytes. Copper(II) and cobalt(II) oxides are from Alfa Aesar, and zinc(II) oxide is from Nanotec.

Electrolyses are driven at a 2.3 A (amp) at the maximum power point of the illuminated concentrator photovoltaic (as shown in Figure S8) or galvanostatically at a set constant current as described in the text. The electrolysis is contained in a pure alumina (AdValue, 99.6%) crucible or pure nickel crucible (Alfa Aesar). Alumina crucible electrolyses used coiled Ni wire (Alfa Aesar, 99.5%) as the (oxygen generating) anode or in scale-up experiments cylinders formed from pure Ni shim (McMaster 9707K5), while electrolyses in the Ni crucibles used the inner walls of the crucible as the anode. Ir anodes were composed of 25 mm × 25 mm × 1 mm 99.7% iridium foil Alfa Aesar 11432 and platinum from Surepure. A wide variety of steel wires for coiled cathodes are effective, an economic form (used in this study) is Fi-Shock 14 gauge, galvanized steel wire model BWC-14200. During electrolysis, the carbon product accumulates at the cathode, which is subsequently removed and cooled. Details of solar (STEP methodology) electrolyses are provided in refs 16, 23, and 25. Subsequent to electrolysis, the product remains on the cathode but falls off when the cathode is extracted, cooled, and uncoiled. The product is washed with either DI water or up to 6 m HCl (both yield similar product, but the latter solution accelerates the washing process) and separated from the washing solution by either paper filtration or centrifugation (both yield similar product, but the latter accelerates the separation process).

The carbon product is washed and analyzed by PHENOM Pro-X energy dispersive spectroscopy on the PHENOM Pro-X SEM; by XRD analysis conducted at a sweep rate of 0.12 degree per minute on a Rigaku Miniflex diffractometer with a 0.01 degree slit width, analyzed using the Jade software package (JADE, 6:1; Materials Data, Inc. Livermore, CA, 2002) and by higher resolution with a Carl Zeiss Sigma VP field emission scanning electron microscope with energy dispersive X-ray detector. Raman spectroscopy was measured with a LabRAM HR800 Raman microscope (HORIBA) with 532.14 wavelength incident laser light, with a high resolution of 0.6 cm^{-1}.

Results and Discussion. Here, we show a facile high yield route of carbon nanostructure formation on inexpensive electrodes via molten carbonate electrolysis. The consumed carbonate is directly replaced by absorbed CO_2. Hence, we show the first demonstration in which this atmospheric carbon dioxide generates carbon nanofibers. Molten carbonates, such as pure Li_2CO_3 (mp 723 °C) or low melting eutectics such as $LiNaKCO_3$ (mp 399 °C) or $LiBaCaCO_3$ (mp 620 °C), mixed with highly soluble oxides, such Li_2O and BaO, can sustain rapid absorption of CO_2 from atmospheric or stack-exhaust CO_2. Equilibrium constraining lithium or lithium/barium oxide absorption has been presented, and in the context of atmospheric or smoke stack CO_2 the lithium case is described as[16−18,23]

$$CO_{2(\text{atmospheric or stack})} + Li_2O_{(\text{dissolved})} \rightleftharpoons Li_2CO_{3(\text{molten})} \quad (1)$$

Scheme 1 presents the successive synthetic variations described in this study that led to the high yield electrolysis of straight uniform CNFs from CO_2 in molten carbonate. Air contains 0.04% CO_2; this is only 1.7×10^{-5} mol of tetravalent carbon per liter, whereas molten carbonate contains ~20 mol of reducible tetravalent carbon per liter. A separate process to concentrate atmospheric CO_2 is not needed in electrolytic CO_2 to CNF conversion. By absorbing CO_2 from the air, molten carbonates provide a million-fold concentration increase of reducible tetravalent carbon available for splitting (to carbon) in the electrolysis chamber. Carbonate's higher concentration of active, reducible tetravalent carbon sites logarithmically decreases the electrolysis potential and can facilitate charge transfer at low electrolysis potentials. CO_2 is bubbled into the molten carbonate, and during electrolysis, oxygen is evolved at the anode, while a thick solid carbon builds at the cathode (Figure 1).

We observe that carbonate is readily split to carbon approaching 100% Coulombic efficiency (Coulombic efficiency is determined by comparing the moles of applied charge to the

DOI: 10.1021/acs.nanolett.5b02427
Nano Lett. XXXX, XXX, XXX−XXX

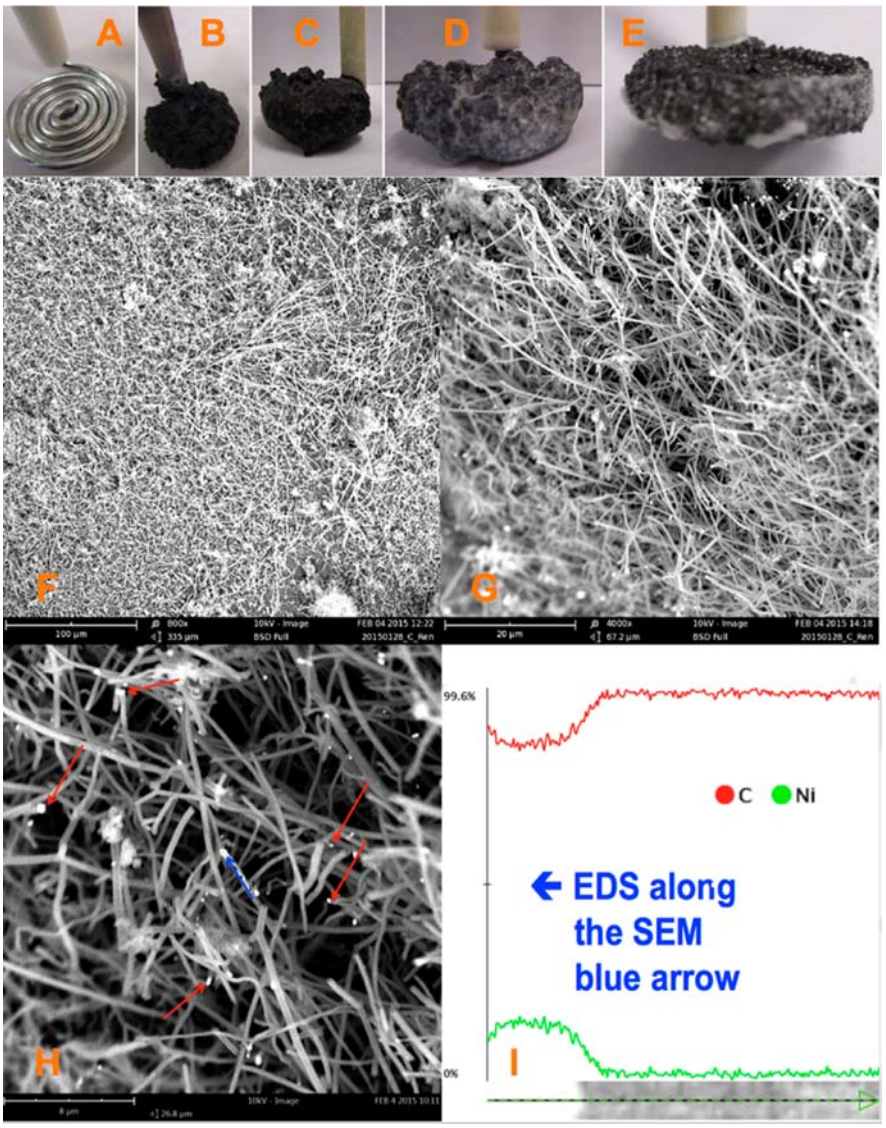

Figure 1. CO_2 to carbon nanofibers formed at a a coiled galvanized steel wire cathode with a nickel anode during 0.05 A; then 1 A constant current electrolysis. No Li_2O is added to the 730 °C molten Li_2CO_3 electrolyte. SEM F to H are shown at various magnifications of the product removed from the cooled, washed cathode. "A" shows the 10 cm^2 coiled wire (0.12 cm diameter) cathode prior to electrolysis. The anode is the inner wall of a 20 mL Ni crucible containing the electrolyte. "B−E" exemplify the typical maximum variation of observed cathodes subsequent to removal from carbonate electrolytes after a long (4 Ah) electrolysis in molten carbonate. Red arrows in SEM "H" indicate typical Ni nucleation sites. The blue arrow originates at one Ni site and moves along the CNF path. "I": EDS composition mapping along the 6 μ blue arrow path shown in SEM "H".

moles of product formed, where each mole of solid carbon product formed depends on four moles of electrons);[16−18,23−28] that is unless carbonates are mixed with hydroxides. In the latter case, H_2 and carbon products are cogenerated.[25] High current densities (>1 A cm^{-2}) of carbon formation are sustained, and we observe similar sustained currents at carbon, platinum, or steel cathodes (each cathode effectively become a carbon electrode during the product deposition). Full cell electrolysis potentials range from less than 1 V under conditions of higher temperature (e.g., 800 °C), low current density (e.g., ≤ 10 mA cm^{-2}), and high oxide concentration (e.g., 6 molal Li_2O), to several volts at high current density (e.g., ≥ 500 mA cm^{-2}). Conditions that increase carbonate electrolysis voltage are high current density, lower temperature, or lower oxide concentration. Below 800 °C, the product is carbon (and oxygen) and at higher temperatures, the product gradually shifts to a mix of carbon and (the 2 electron reduction to) carbon monoxide. It becomes pure CO (and $1/2O_2$) by 950 °C.[24] The ≤800 °C four-electron processes is given by

$$Li_2CO_{3(molten)} \rightarrow C_{(solid)} + Li_2O_{(dissolved} + O_{2(gas)} \quad (2)$$

For a net reaction with eq 1:

$$CO_{2(atmospheric\ or\ stack)} \rightarrow C_{(solid)} + O_{2(gas)} \quad (3)$$

The cathode product of dissolved carbon dioxide in molten carbonate tends to be an uncontrolled mix of graphites and amorphous carbons (Supporting Information). However, the cathode electrolysis product shown in the SEM of Figure 1 consists of controlled carbon fibers with metal nucleation points (as shown in the figure by EDS using with Ni nucleation). The vast majority of the Ni nanoparticles in the SEM are located at nanofiber tips, while a relative few seem to be aside from, and not associated with, CNF growth. The fibers

DOI: 10.1021/acs.nanolett.5b02427
Nano Lett. XXXX, XXX, XXX−XXX

are homogeneous throughout the cathode product, characterized by uniform diameters of 200 to 300 nm, and with length of 20 to 200 μm. The fibers are prepared by electrolysis at a 10 cm^2 coiled galvanized steel wire cathode (shown) and an oxygen generating nickel anode in 730 °C molten Li_2CO_3, initiated by a low current of 5 mA/cm^2 cathode, followed by constant current electrolysis at high current (100 mA cm^2) for 2 to 4 Ah. The cooled product consists of fibers mixed with solidified electrolyte. Product readily falls of the cooled cathode when it is uncoiled. The Coulombic efficiency is over 80% (and approaches 100% with carefully recovery of all product after washing); the product (after washing off the electrolyte) consists of >80% pure carbon nanofibers. SEM are shown after washing electrolyte from the product. The washed cathode product is further characterized by X-ray powder diffraction, XRD, and Raman spectroscopy in Figure 2.

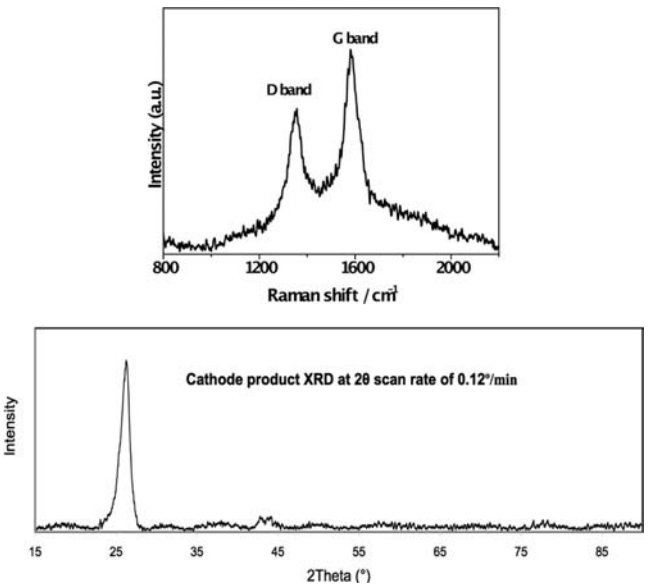

Figure 2. Top: Raman of the carbon products. Bottom: X-ray powder diffraction of the cathode carbon product.

The XRD diffraction peaks in Figure 2 at 26° and 43° are assigned to the hexagonal graphite (002) and diffraction planes (JCPDS card files no. 41-1487) within the CNF (specifically, the stacking of parallel graphene layers and the size of graphene layer, respectively).[19] The resolved XRD peaks at 43° (100 plane) and 44° (101 plane) is evidence of homogeneity of the synthesized CNFs. Raman spectrum was recorded to study the degree of graphitization of the carbon nanofibers. The Raman spectrum exhibits two sharp peaks observed at 1350 and 1580 cm^{-1}, which correspond to the disorder-induced mode (D band) and the high frequency E_{2g} first order mode (G band), respectively. The intensity ratio between D band and G band (I_D/I_G) is an important parameter to evaluate the graphitization and is 0.70 in our case, which is consistent with commercial hollow carbon nanofiber samples.[30] All of the above information indicates the formation of good CNFs.

In the absence of a nucleating metal, such as Ni, CNFs are not evident during molten electrolysis. This is shown in the Supporting Information in which a Pt or Ir anode is used instead of the Ni electrode. Subsequent to electrolysis in a Ni-free environment (Li_2CO_3 at 730 °C with 6 molal Li_2O utilizing either a Pt or Ir, rather than Ni, anode), amorphous and platelet structures are seen instead of fibers, indicative of partially formed multilayered graphene/graphite structures. Electron dispersive spectroscopy elemental analysis indicates that the amorphous and platelet structures are composed of >99% carbon.

We had not previously anticipated the oxygen-generating anode effects on the structure of the carbon formed at the cathode during carbonate electrolysis. As demonstrated here, these anode effects promote significant carbon nanofiber formation. We have investigated Pt, Ir, and Ni, and each can be effective as molten carbonate oxygen generating anodes.[7,8,23−29] Whereas Ir exhibits no corrosion following hundreds of hours use in molten carbonates, the extent of Ni corrosion is determined by the cation composition of the carbonate electrolyte. A nickel anode undergoes continuous corrosion in a sodium and potassium carbonate electrolyte,[25] it is stable after initial minor corrosion in lithium carbonate electrolytes,[8] and no corrosion of the nickel anode is evident in barium/lithium carbonate electrolytes.[22,25] In lithium carbonate electrolytes, we have quantified the low rate of nickel corrosion at the anode as a function of anode current density, electrolysis time, temperature, and lithium oxide concentration.[17] The Ni loss at a 100 mA cm^{-2} Ni anode in Li_2CO_3 at 750 °C with 0 or 5 molal added Li_2O is respectively 0.5 or 4.1 mg cm^{-2} of anode subsequent to 600 s of electrolysis and increases to 4.6 or 5.0 mg cm^{-2} subsequent to 1200 or 5400 s of electrolysis. The Ni loss increases to 7.0 mg or 13.8 mg cm^{-2}, respectively, subject to higher current (1000 mA cm^{-2}) or higher temperature (950 °C). Each of these nickel losses tends to be negligible compared to the mass of Ni used in the various Ni wire or Ni shim configured anodes. Nickel oxide has a low solubility of 10^{-5} mol NiO per mol of molten Li_2CO_3,[31] equivalent to 10 mg Ni per kg Li_2CO_3. This low, limiting solubility constrains some of the corroded nickel to the anode surface as a thin oxide overlayer, with the remainder as soluble oxidized nickel available for reduction and redeposition at the cathode.

The characteristic CNF structure is observed when the electrolysis is initiated at a gradually increasing current density, or with an initial low current (1 h of 5 mA cm^{-2} at the cathode) followed by an extended high current electrolysis such as at 100 mA cm^{-2} (for several hours). However, when the electrolysis starts directly at only a high (100 mA cm^{-2}) current density. The cathode product is principally amorphous (and only ~25% CNF). The linear EDS map on the middle, right lower side of Figure 1 shows elemental variation along the 6 μm path of the EDS scan from pure Ni at the start of the fiber to pure carbon along the remainder of the fiber. We interpret this mechanistically as follows: due to its low solubility and lower reduction potential, nickel (in this case originating from the anode) is preferentially deposited at low applied electrolysis currents (5 or 10 mA cm^{-2}). This is evidenced by the low observed electrolysis voltage (<0.7 V) and sustains the formation of nickel metal cathode deposits, which appear to be necessary to nucleate CNF formation. The high concentration of electrolytic $[CO_3^{2-}] \gg [Ni^{2+}]$ and mass diffusion dictates that higher currents will be dominated by carbonate reduction. The subsequent higher electrolysis voltage thermodynamically required to deposit carbon[24] is only observed at higher applied currents (>20 mA cm^{-2}). Hence, without the initial application of low current, amorphous carbon will tend to form, while the CNF structures are readily formed following the low current nickel nucleation activation. The lithium carbonate electrolyte has an abundant Li ion

DOI: 10.1021/acs.nanolett.5b02427
Nano Lett. XXXX, XXX, XXX−XXX

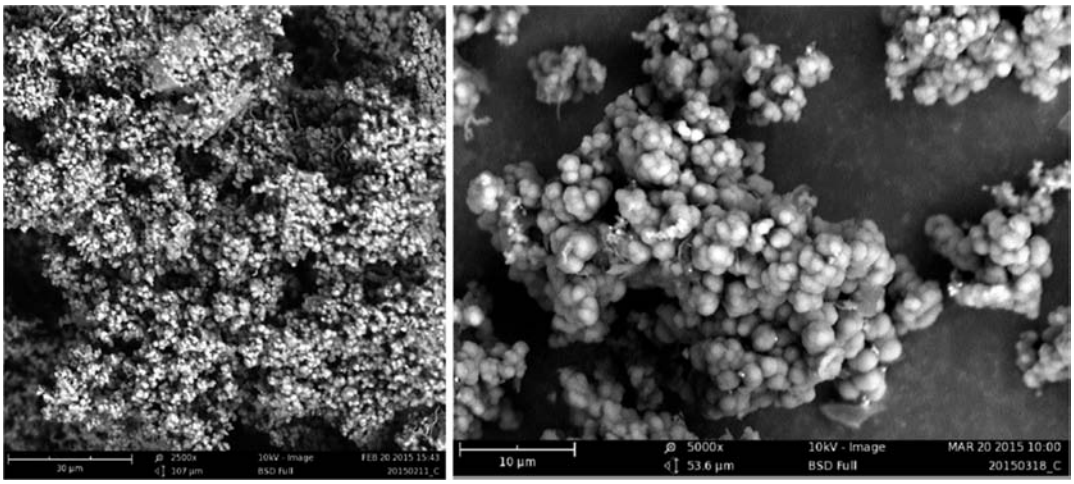

Figure 3. Zn effect (without Ni, Co, or Cu) on SEM of the carbon product formed at the cathode following electrolysis in Li_2CO_3 (without added Li_2O) between a planar, square 2.5 by 2.5 cm iridium anode and a coiled wire 10 cm^2 galvanized (Zn coated) steel cathode. Each electrolysis is conducted at a low initial (0.05A) current to initiate any metal nucleation at the cathode followed by a 1 A electrolysis for 2 h (2 Ah). The observed product is the same without (left side) and with (right side) 0.06 m ZnO added to the 770 °C molten Li_2CO_3 electrolyte.

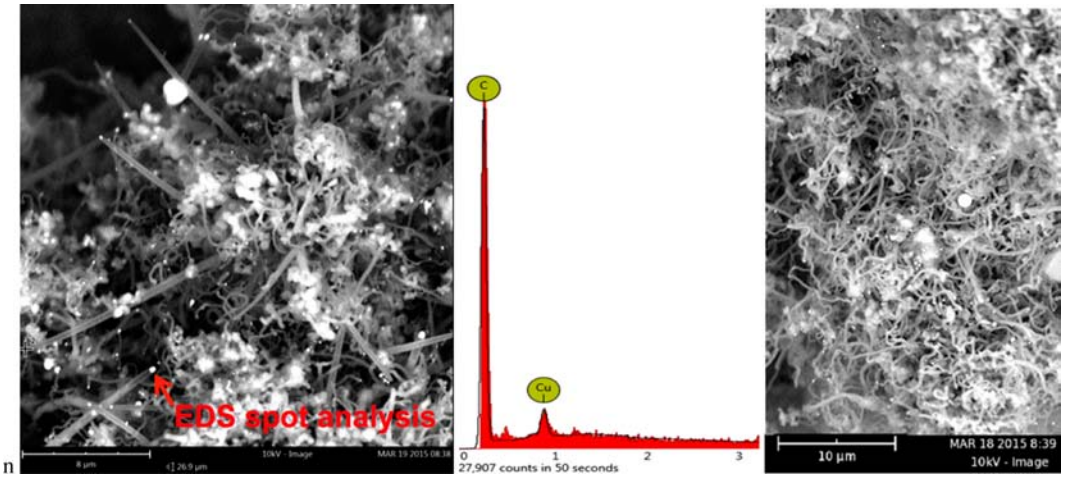

Figure 4. Cu or Co effect (without Ni) on SEM of the carbon product formed at the cathode following electrolysis in Li_2CO_3 (without added Li_2O) between a planar, square 2.5 by 2.5 cm iridium anode and a coiled wire 10 cm^2 galvanized (Zn coated) steel cathode. Top: with 0.06 m CuO; bottom right: with 0.06 m CoO added to the 770 °C molten Li_2CO_3 electrolyte. Bottom: left EDS analysis of spot shown from the CuO cathode product. Each electrolysis is conducted at a low initial (0.05) current to initiate any metal nucleation at the cathode followed by a 1 A electrolysis for 2 h (2 Ah).

concentration, and we see no evidence that Li ion intercalation interferes with the CNF growth. Li intercalation can still occur, but not the explosive exfoliation of the graphite associated with lithium metal deposition (the applied potential is too low to allow Li metal growth).

Rather than the *straight, uniform diameter* CNFs observed in Figure 1, when Li_2O is added to the molten Li_2CO_3 electrolyte the electrolysis product is a proliferation of *tangled* CNFs of a *wide variety of diameters* as shown in the Supporting Information. Evidently, high concentrations of oxide localized in the CNF formation region leads to torsional effects (tangling).

The cathode consists of galvanized (zinc coated steel. This zinc metal is a critical activator to the observed high-yield CNF production but acts in a manner different than the nickel metal type of nucleation. Unlike Ni, Zn melts at 420 °C and is a liquid at the electrolysis temperature. Figure 3 presents the action of Zn (in the absence of nickel), whether present only as zinc metal on the galvanized steel cathode surface, or additionally as added as 0.06 m ZnO to the molten Li_2CO_3 electrolyte on the carbon nanostructures formed at the cathode. In either case, carbon is formed on a 10 cm^2 cathode as photographed in the top left of Figure 1, but the anode instead of nickel is a planar 6.3 cm^2 square iridium electrode. The observed cathode product conformation consists of spherical ~1 μm carbon structures gathered in 3 to 6 μm clusters. In addition, a small fraction (<10%) of the washed product is seen to contain CNFs. *In the absence of zinc* (using either iron or nongalvanized steel cathodes) but in the presence of nickel, produced amorphous graphites and uncontrolled nanofiber structures with diameters ranging from 0.2 to 4 μm and either circular or rectangular duct-like cross sections as shown in the Supporting Information.

Figure 4 presents evidence that in addition to Ni, Cu and Co can also act as nucleation sites in the high yield formation of CNFs at the cathode during electrolysis of molten carbonates. Each electrolyte yields CNFs. In the top SEM of the CuO cathode product, EDS analysis of the bright spot shown at the

DOI: 10.1021/acs.nanolett.5b02427
Nano Lett. XXXX, XXX, XXX−XXX

beginning of the carbon nanofiber exhibits pure copper and carbon, providing evidence that the deposited copper acts as a nucleation point to initiate CNF formation. Each of the nucleation metals which we have observed that promote CNF growth have in common that they require a low reduction/deposition potential (which is less than that required for carbon growth) and lead to higher CNF yield when deposited from low concentrations at low electrochemical current density. This range of metals including nickel, copper, iron, and cobalt enhancing the high yield production of CNFs by molten electrolysis correlates with the metals that catalyze CVD growth of CNFs.[10,19]

As observed in Figures 1 and 4, and as further delineated in the Supporting Information, Ni, Cu, Co, or Fe nucleates the high-yield, high-rate production of carbon nanofiber formation in the presence of zinc metal. However, little or uncontrolled CNF formation is observed in the absence of zinc. In each of the prior experiments, zinc metal (which melts at 420 °C) is present in the form of the coating over the steel cathode formed from conventional, galvanized steel wire. A high fraction of the carbon product is consistently CNFs when galvanized (with zinc) steel is used as the cathode and is not when either iron wire or 316 stainless steel shim was employed as the cathode.

As noted, we observe that electrolyses initiated at a high current generated a profusion of amorphous graphites, and a variety of carbon nanostructures rather than a high yield of nanofibers, while electrolyses initiated with a low current step prior to the high current can generate a high yield of uniform CNFs. Deposition of Ni, Co, Cu (or Fe) at low current density, from electrolytes which have a low concentration of the metal, dissolved as the oxide, lead to small, isolated nucleation sites on the cathode, as evidenced by EDS, which promote CNF growth. A solid metal cathode does not have these characteristics and does not lead to homogeneous CNF growth. As seen in the SI, an overabundance of Fe leads to uncontrolled growth, which in the extreme would tends toward an undefined randomly distributed (amorphous) carbon. Combined with an absence of zinc metal, the absence of this low current step produced amorphous graphites (Supporting Information) or a profusion of nanofiber structures (Supporting Information) with diameters ranging from 0.2 to 4 μm and either circular or rectangular duct-like cross sections. It will be of interest in future studies to isolate conditions that refine the distribution of these different structures. As previously noted, the low current step occurs at a potential of <0.7 V, which is sufficient to form metal nucleation sites at the cathode, but is thermodynamically energetically insufficient to reduce carbonate to solid carbon.

A proposed mechanism of the observed high yield CNF that is consistent with the observed zinc activation and metal nucleation effects is presented and the observation that the STEP CNF electrolysis chamber is readily scalable are described in the Supporting Information. The demonstrated CNF synthesis can be driven by any electric source. As an alternative to conventionally generated electrical, we have also driven the CNF synthesis using electric current as generated by an illuminated efficient concentrator photovoltaic operating at maximum power point (SI).

Conclusions. Here, we show a new high yield pathway to produce carbon nanofibers directly from atmospheric or exhaust CO_2 in an inexpensive molten electrolysis. Formation of a highly valued, compact, readily stored form of carbon directly from carbon dioxide may provide a new pathway to mitigate this greenhouse gas. Today, carbon nanofibers require 30- to 100-fold higher production energy compared to aluminum production. We present the first high yield, inexpensive synthesis of carbon nanofibers from the direct electrolytic conversion of CO_2, dissolved in molten carbonates to CNFs at high rates using scalable, inexpensive nickel and steel electrodes. The structure is tuned by controlling the electrolysis conditions, such as the addition of trace nickel to act as CNT nucleation sites, limits to the electrolytic oxide concentration, inclusion of zinc, and control of current density. New infrastructure and merchandise built from CNFs would provide a repository to store atmospheric CO_2. The Raman, XED, and SEM characterization provides fundamental evidence of the high yield and purity of the CNF synthesis. Future papers will explore application level testing of the strength, thermal, and electrical conductivities and lithium ion intercalation properties of the CNFs synthesized from CO_2 in molten salts tuned for applications under various electrochemical conditions. It is evident in the Supporting Information that a range of carbon nanostructures is attainable and future studies will probe conditions to characterize and optimize growth of these structures.

■ ASSOCIATED CONTENT

Supporting Information

The Supporting Information is available free of charge on the ACS Publications website at DOI: 10.1021/acs.nanolett.5b02427.

(i) Conventional CO_2 to carbon formation in carbonates, (ii) Ni catalyzed CO_2 to CNF formation, (iii) other metals' action on molten electrolytic carbon formation, (iv) a mechanism of high yield electrolytic CNF formation, (v) scalability of the CNT formation, and (vi) high rate CO_2 splitting in carbonates at high solar efficiency (PDF)

■ AUTHOR INFORMATION

Corresponding Author

*E-mail: slicht@gwu.edu.

Notes

The authors declare no competing financial interest.

■ ACKNOWLEDGMENTS

This project was supported in part by a grant from the United States National Science Foundation 1230732. We are grateful to the Director of the George Washington University Institute for Nanotechnology Prof. Michael Keidar and his research group members Dr. Alexey Shashurin and Xiuqi Fang for their help in attaining the Raman spectroscopy.

■ REFERENCES

(1) pluscomposites, *Composites: Materials of the Future*: Part 4: Carbon fibre reinforced composites, at: http://www.pluscomposites.eu/publications, directly accessed July 16, 2015 at: http://www.pluscomposites.eu/sites/default/files/Technical%20series%20-%20Part%204%20-%20Carbon%20fibre%20reinforced%20composites_0.pdf.

(2) Kim, H. C.; Fthenakis, V. *J. Ind. Ecol.* **2013**, *17*, 528−541.

(3) Greiner, A.; Wendorff, J. H. *Angew. Chem., Int. Ed.* **2007**, *46*, 5670−5703.

(4) Shen, Y.; Yan, L.; Song, H.; Yang, J.; Yang, G.; Chen, X.; Zhou, J.; Yu, Z.-Z.; Yang, S. *Angew. Chem., Int. Ed.* **2012**, *51*, 12202−12205.

DOI: 10.1021/acs.nanolett.5b02427
Nano Lett. XXXX, XXX, XXX−XXX

(5) Hsu, W. K.; Hare, J. P.; Terrones, H. W.; Kroto; Walton, D. R. M. *Nature* **1995**, *377*, 687.
(6) Kodumagulla, A.; Varanasi, V.; Perace, R. C.; Wu, W. C.; Hensley, D. K.; Tracey, J. B.; McKnight, T. E.; Melechko, A. V. *Nanomater. Nanotechnol.* **2014**, *115*, 1464−1473.
(7) Vander Wal, R. L.; Hall, L. J. *Chem. Phys. Lett.* **2001**, *349*, 178−184.
(8) Mahammadunnisa, S.; Reddy, E. L.; Ray, D.; Subrahmanyam, C.; Whitehead, J. C. *Int. J. Greenhouse Gas Control* **2013**, *16*, 361−363.
(9) Iijima, S. *Nature* **1991**, *354*, 56−58.
(10) Ebbesen, T. W.; Ajayan, P. M. *Nature* **1992**, *358*, 220−222.
(11) Lallave, M.; Bedia, J.; Ruiz-Rosas, R.; Rodríguez-Mirasol, J.; Cordero, T.; Otero, J. C.; Marquez, M.; Barrero, A.; Loscertales, I. G. *Adv. Mater.* **2007**, *19*, 4292−4296.
(12) Wu, A.-Y.; Li, C.; Liang, H.-W.; Chen, J.-F.; Yu, S.-H. *Angew. Chem., Int. Ed.* **2013**, *52*, 2925−2929.
(13) Dimitrov, A. T. *Maced. J. Chem. Chem. Eng.* **2009**, *28*, 111−118.
(14) Bardgett, R. D.; Putten, W. H. *Nature* **2014**, *515*, 505−511.
(15) Giosan, L.; Syvitski, J.; Constantinescu, J.; Day, J. *Nature* **2014**, *516*, 31−33.
(16) Licht, S. *Adv. Mater.* **2011**, *23*, 5592−5612.
(17) Licht, S.; Wu, H. *J. Phys. Chem. C* **2011**, *115*, 25138−25157.
(18) Licht, S.; Wu, H.; Hettige, C.; Wang, B.; Lau, J.; Asercion, J.; Stuart, J. *Chem. Commun.* **2012**, *48*, 6019−6021.
(19) Song, Y.; Youn, J.; Gutowski, T. *Composites, Part A* **2009**, *40*, 1257−1265.
(20) Burkhardt, Z. *Chem.* **1870**, *13*, 213. as referenced in Haber, F.; Tolloczko, St. *Z. Anorg. Chem.* **1904**, *41*, 407.
(21) Dimitrov, A.; Tomova, A.; Grozdanov, A.; Popovski, O.; Paunović, P. *J. Solid State Electrochem.* **2013**, *17*, 399−407.
(22) Novoselova, I.; Oliinyk, N.; Voronina, F.; Volkov, S.; Konchits, A.; Yanchuk, I.; Yefanov, V.; Kolesnik, S.; Darpets, M. *Phys. E* **2008**, *40*, 2231−2237.
(23) Licht, S.; Cui, B.; Wang, B. *J. CO2 Utilization* **2013**, *2*, 58−63.
(24) Licht, S.; Wang, B.; Ghosh, S.; Ayub, H.; Jiang, D.; Ganley, J. *J. Phys. Chem. Lett.* **2010**, *1*, 2363−2368.
(25) Li, F.-F.; Liu, S.; Cui, B.; Lau, J.; Stuart, J.; Wang, B.; Licht, S. *Adv. Energy Materials* **2015**, *5*, 1−7.
(26) Licht, S. *J. Phys. Chem. C* **2009**, *113*, 16283−16292.
(27) Cui, B.; Licht, S. *Green Chem.* **2013**, *15*, 881−884.
(28) Licht, S.; Wang, B. *Chem. Commun.* **2010**, *46*, 7004−7006; **2011**, *47*, 3081−3083.
(29) Licht, S.; Cui, B.; Wang, B.; Li, F.-F.; Lau, J.; Liu, S. *Science* **2014**, *345*, 637−640.
(30) Saravanan, M.; Sennu, P.; Ganesan, M.; Ambalavan, S. *J. Electrochem. Soc.* **2012**, *160*, A70−A76.
(31) Ota, K.; Mitshuima, S.; Kato, S.; Asano, S.; Yoshitake, H.; Kaymiya, N. *J. Electrochem. Soc.* **1992**, *139*, 667−671.

DOI: 10.1021/acs.nanolett.5b02427
Nano Lett. XXXX, XXX, XXX−XXX

Supporting Information for:

One-pot synthesis of carbon nanofibers from CO_2

*Jiawen Ren,[†] Fang-Fang Li,[†] Jason Lau,[†] Luis González-Urbina,[†] and Stuart Licht,[†,] **

[†]Department of Chemistry, The George Washington University, Washington, DC, 20052, USA

Corresponding Author

*E-mail: slicht@gwu.edu.

I. Conventional CO_2 splitting (an example without nano-size control or CNF formation) in carbonates

The SEM in Fig. S1 evidences no CNF in the carbon product deposited at the cathode subsequent to carbonate electrolysis in a nickel-free environment (Li_2CO_3 at 730°C with 6 molal Li_2O in the absence of nickel, or added iron oxides, and utilizing either a Pt or Ir anode rather than a Ni anode). Amorphous and platelet structures are seen, with the platelets indicative of partially formed multi-layered graphene/graphite. Electron dispersive spectroscopy elemental analysis indicates that the amorphous and platelet structures are composed of > 99% carbon. Similarly, little CNF (< 10%) formation was observed in the cathode product when the electrolysis was instead conducted with a Ni anode in a corrosion-free lower temperature (630°C) $Li_{1.6}Ba_{0.3}Ca_{0.1}CO_3$ electrolyte. Low temperature and the addition of the alkali earth cations suppresses Ni oxidation and anodic dissolution into the molten carbonate.[23,25]

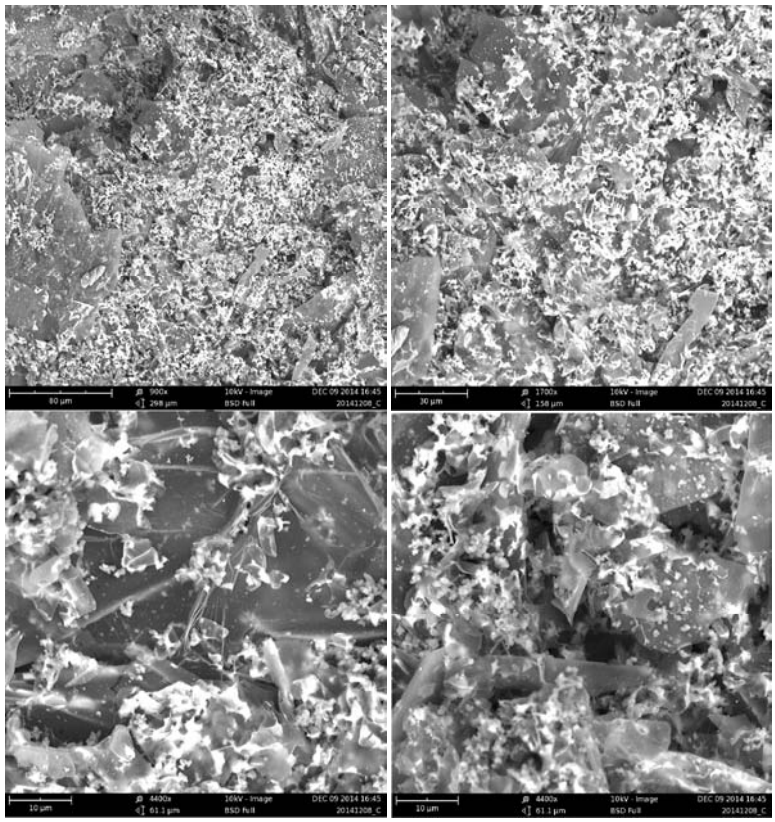

Figure S1. CO_2 electrolysis to carbon in molten carbonate without carbon nanofibers in a no-nickel environment (using a Pt anode). No carbon nanofibers are evident. SEM of the washed cathode product subsequent to a nickel-free, 1.5 hour, 1 A constant current electrolysis in 730°C molten Li_2CO_3 with 6 m Li_2O using a 10cm^2 Pt foil anode and a 10cm^2 coiled steel wire (0.12 cm diameter) cathode, in a Ni-free crucible.

II. **Ni catalyzed carbon nanofiber formation from CO_2 splitting in carbonates**

Nickel originating from corrosion of the anode can deposit onto the galvanized (zinc coated) cathode and catalyze carbon nanofiber formation. As illustrated in Fig. S2, higher nickel release during the carbonate electrolysis, which can be controlled by the amount released due to the size of the nickel anode, results in a proliferation of CNFs of various diameters. As illustrated in Fig. S3, a lower concentration of controlled release of nickel results in the generation of highly homogeneous, smaller diameter carbon nanofiber structures. Both products were formed during electrolysis on a steel wire cathode in 730°C Li_2CO_3 with added Li_2O. The Figure S2 carbon product was generated in a cell containing a purposefully oversized Ni anode, and the wide variety of carbon nanofibers generated in this single experiment range from ~0.2 to 4 μm in diameter and are up to 100μm in length.

Straight, rather than tangled, CNT/CNF formation: The high nickel electrolysis product examined in the SEM of Figure S2 present a proliferation of tangled carbon nanofibers of a wide variety of diameters. The nickel initiated electrolysis product examined in the SEM of Figs. S3 and S4 present a tangle of homogeneous-diameter carbon nanofibers. Each of those electrolyses utilized a molten Li_2CO_3 electrolyte with 6 m added (dissolved) Li_2O. Evidently, high concentrations of oxide localized in the nanofiber formation region leads to torsional effects (tangling). As shown in Figure 1 of the main text carbon nanofibers grown by electrolysis in pure molten Li_2CO_3 (without added Li_2O) are consistently untangled, uniform and long. The CNTs range from 300 to 1000 nm in width and 20 to 200 μm long. The better resolved XRD peaks at 43° (100 plane) & 44° (101 plane) in Fig. 2 compared to Fig. S2 is evidence of better homogeneity of the CNTs synthesized under the Ni-limited conditions.

The predominant carbon nanofiber structured cathode product is observed when the electrolysis is initiated at low current, typically at 5 mA cm^{-2}, followed by an extended high current electrolysis such as at 100 mA cm^{-2}. The cathode product is principally amorphous (and only ~25% CNF), when the electrolysis starts directly at only a high (100 mA cm^{-2}) current density. We interpret this mechanistically as follows: due to its low solubility and lower reduction potential, nickel (in this case originating from the anode) is preferentially deposited at low applied electrolysis currents (5 or 10 mA cm^{-2}). This is evidenced by the low observed electrolysis voltage (<0.7V) and sustains the formation of nickel metal cathode deposits, which appear to be necessary to nucleate carbon nanofiber formation. The concentration of electrolytic

$[CO_3^{2-}]$ >> $[Ni^{2+}]$, and mass diffusion dictates that higher currents will be dominated by carbonate reduction. The subsequent higher electrolysis voltage thermodynamically required to deposit carbon[24] is only observed at higher applied currents (> 20 mA cm^{-2}). Hence, without the initial application of low current, amorphous carbon will tend to form, while the carbon nanofiber structures are readily formed following the low current nickel nucleation activation. In our typical high yield electrolyses, the current is increased from 50 to 1000 mA at a 10 cm^{-2} steel cathode over 15 minutes, followed by a constant current electrolysis at 1000 mA.

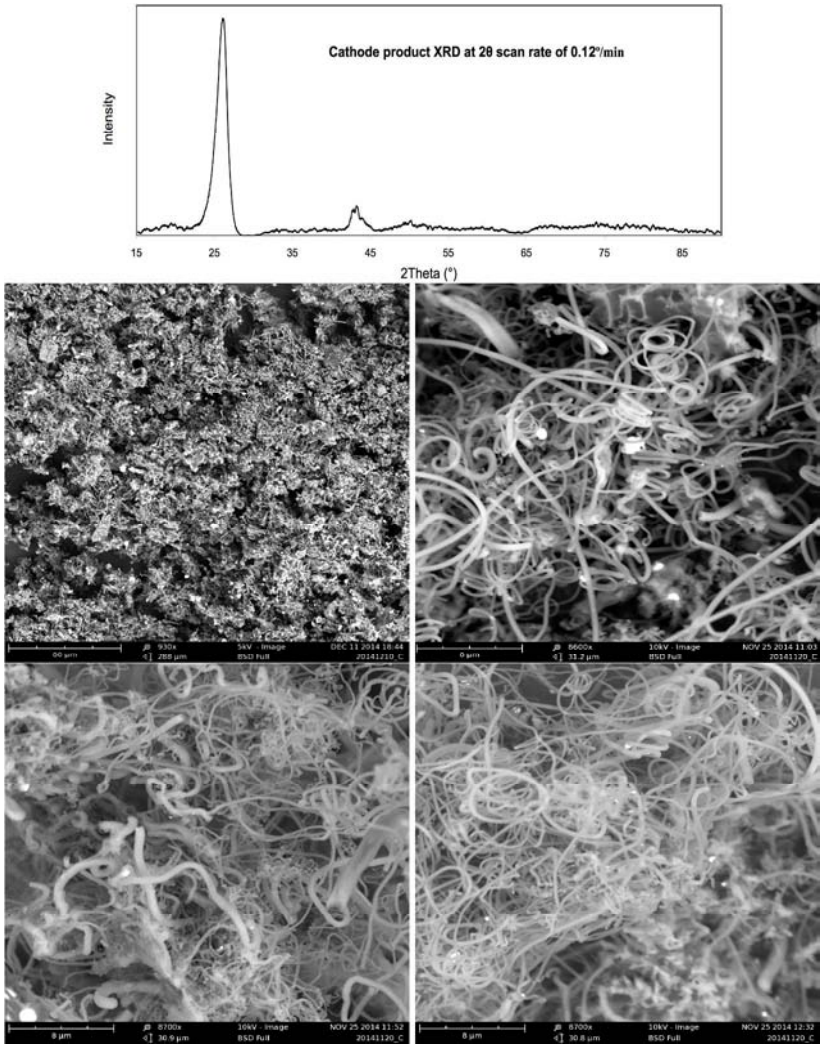

Figure S2. CO_2 to a diverse range of carbon nanofibers from high nickel media (subsequent to electrolysis with an oversized nickel anode, the inner wall of a 50 ml Ni crucible, at 0.05 A, then 1 A constant current electrolysis for 2 hours in 730°C molten Li_2CO_3 with 6 m Li_2O using a 10cm^2 coiled, 0.12 cm diameter steel wire). Top: X-ray powder diffraction of the carbon product. Middle, bottom: SEM of the washed cathode product subsequent to electrolysis with an oversized nickel cathode (the inner wall of a 50 ml Ni crucible. Consistent tangled fiber product with a wide range of diameter are observed throughout. Typical constant current electrolysis potentials range from 0.5 to1.5 V as the current density is increased from 0.05 A to 1A.

The CNFs synthesized in Fig. S3 utilized the same cathode and same composition electrolyte as in the Figure S2 synthesis, but with a controlled, limited amount of nickel released to limit the Ni nucleation points forming on the cathode. This was accomplished by using a smaller (by one third) surface area of nickel anode in the electrolysis cell. As illustrated in Fig. S4 a lower concentration of controlled release of nickel results in the generation of highly homogeneous CNFs with a smaller, consistent diameter of ~0.2 μm .

As seen in the electron dispersive spectroscopy in Figure S3, the SEM bright spots are Ni deposits on the cathode. This is consistent with the known alternative CVD CNF growth mechanism, in which Ni acts as nucleation sites to initiate CNF growth.[7] The washed cathode product is further characterized by x-ray powder diffraction, XRD in Figures 2 and S2. The XRD diffraction peaks at 26° and 43° are assigned to the hexagonal graphite (002) and diffraction planes (JCPDS card files no. 41-1487) within the CNF (specifically, the stacking of parallel graphene layers and the size of graphene layer, respectively).[19] The resolved XRD peaks at 43° (100 plane) & 44° (101 plane) in Figure 2 is evidence of homogeneity of the synthesized CNFs.

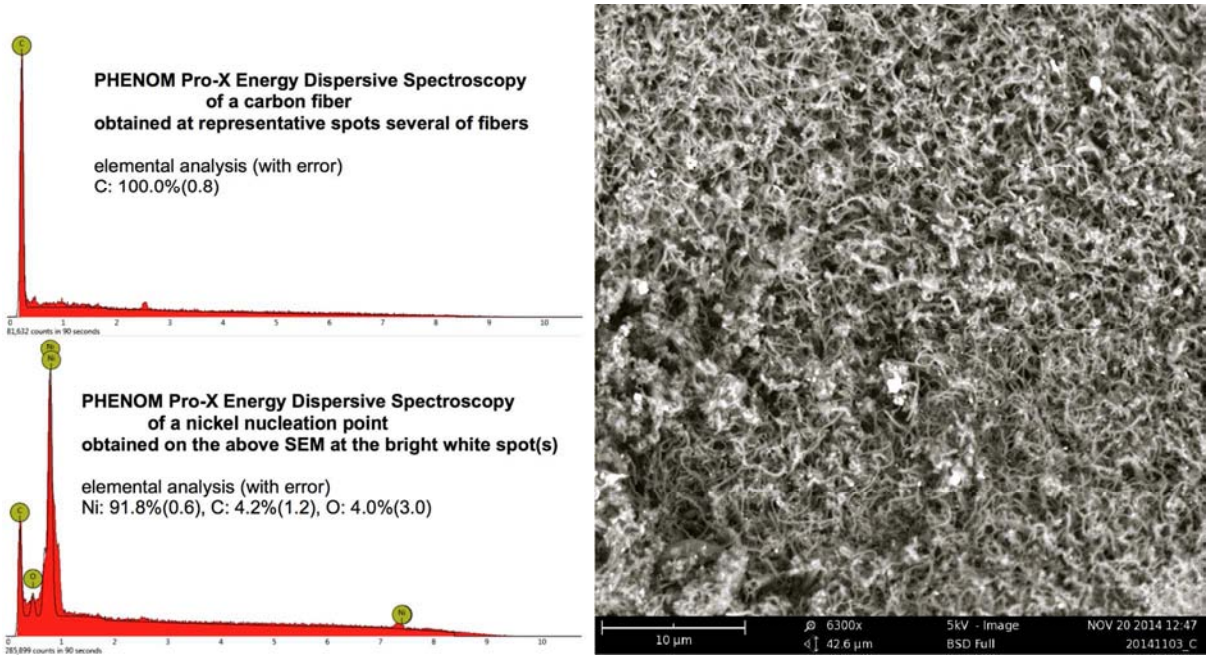

Figure S3. CO_2 to homogenous set of carbon nanofibers from controlled nickel media, 6 m added Li_2O electrolyte. Left, middle: (repeated, representative of) EDS on fiber showing high carbon concentration; EDS right: (repeated, representative) EDS on bright spot showing high nickel concentration top) and on a CNF (bottom). Right, bottom: SEM of washed cathode product subsequent to electrolysis with a smaller nickel cathode (the inner wall of a 20 ml Ni crucible), 0.05 A, then 1 A constant current electrolysis in 730°C molten Li_2CO_3 with 6 m Li_2O using a 10cm^2 coiled steel wire (0.12 cm diameter). Throughout the sample the SEM consistently exhibited the same diameter of carbon nanofiber structures.

III. Other metals' action on molten electrolytic carbon formation

The action of metals other than nickel on carbon nanostructures formed in the cathode product during electrolysis in molten carbonate is probed by (i) adding no Li_2O to the molten carbonate (ii) replacing the nickel anode with an iridium anode, and (iii) adding metal oxide to the electrolyte. As previously described[17] the iridium, while expensive, is extremely stable and exhibits no evidence of corrosion, dissolution or cathodic redeposition (as measured by EDS of the cathode) during extended use (hundreds of hours) as an anode in molten lithium carbonates without added lithium oxide.

Fig. S4 presents SEM of the effect of added nickel (top) or iron oxide (bottom) on the carbon product formed during electrolysis in molten Li_2CO_3 electrolyte in the nickel-free (iridium) anode electrolysis cell. The 0.06 m added NiO to the electrolyte provides a large supersaturation excess of Ni(II) and undissolved NiO remains evident at the bottom of the electrolysis cell. As evident in the large anode (high Ni) case of the SEM in Fig. S2, a wide variety of type diameters are evident, but additionally in this Fig. S4 case a larger proportion (~25%) of non-fiber carbon nanostructures are evident. We hypothesize that the more controlled release of Ni(II) from the nickel anode in the Fig. S3 example, rather than as dissolved excess NiO in Figure S2, provides for more uniform nucleation of nickel at the cathode leading to the observed even higher fraction of carbon nanofiber structures. Unlike nickel oxide, we have previously discovered that iron oxide is highly soluble (~10 m) in lithiated carbonate electrolytes, dissolving as $Fe_2O_3 + Li_2O \rightarrow 2LiFeO_2$.[27,28] The concentration of iron oxide as a source for reduction to form iron nucleation points for CNT formation is more difficult to control, particularly when using an iron (metal) based cathode. The SEM shown in the lower portion of Fig. S4, shows that this level (0.06 molal) of dissolved $LiFeO_2$ results in a profusion of carbon nanofiber structures.

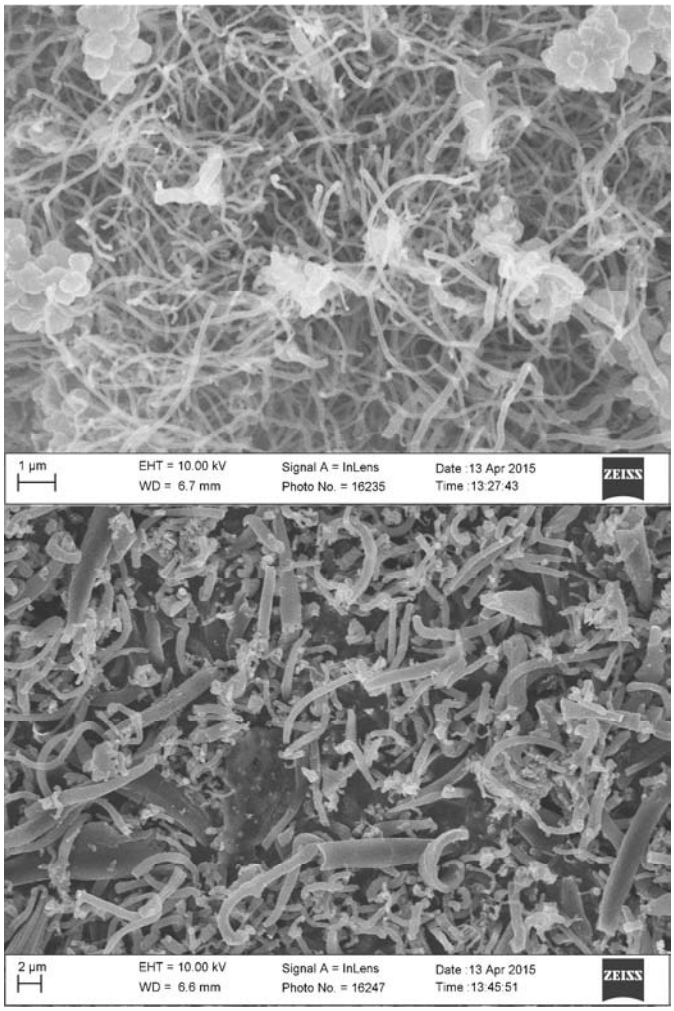

Figure S4. Fe or Ni effect, added as the oxide to the electrolyte, on the SEM of the carbon product formed at the cathode following electrolysis in Li_2CO_3 (without added Li_2O) between a planar, square 2.5 by 2.5 cm iridium anode and a coiled wire 10 cm^2 galvanized (Zn coated) steel cathode. Top: with 0.06 m NiO; bottom: with 0.05 m $LiFeO_2$ added to the 770°C molten Li_2CO_3 electrolyte. Each electrolysis is conducted at a low initial (0.05) current to initiate any metal nucleation at the cathode followed by a 1A electrolysis for 2 hours (2Ah).

IV. A mechanism of high yield electrolytic CNF formation

As observed, nickel nucleates the high-yield, high-rate production of carbon nanofiber formation in the presence of zinc metal. However, it is interesting to note in the SEM at the top of Fig. S5 that little or uncontrolled CNF formation is observed in the absence of zinc. In each of the prior experiments zinc metal (which melts at 420°C) is present in the form of the coating over the steel cathode formed from conventional, galvanized steel wire. A high fraction of the

carbon product is consistently CNFs when galvanized (with zinc) steel is used as the cathode, and is not when either iron wire, or 316 stainless steel shim was employed as the cathode.

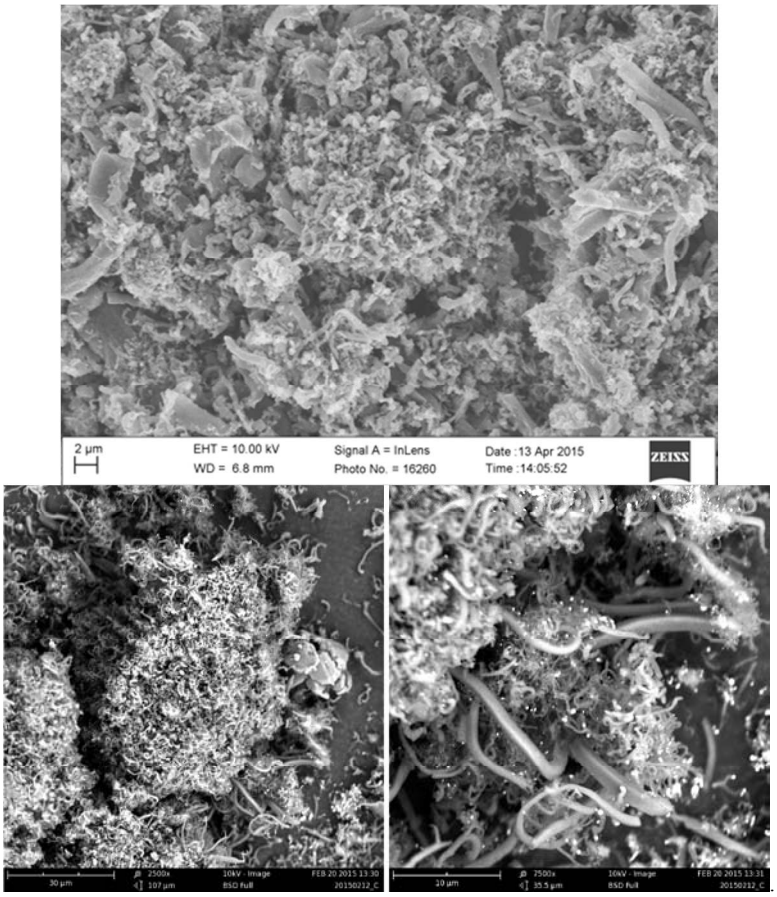

Figure S5. Top: SEM showing the lack of CNF, despite the presence of a Ni anode (as the inner wall of a 20 ml Ni crucible), specifically when carbonate is electrolyzed at a zinc free iron cathode and without an initial, low current activating current step. The electrolyses are conducted a 1A electrolysis for 2 hours (2Ah) using a 10cm^2 coiled iron wire (0.12 cm diameter), rather than galvanized steel wire. Bottom: a low fraction of CNFs is observed when the a zinc free cathode is used with a 2.5 by 2.5 cm iridium anode and with 0.06 m NiO added to the electrolyte.

As previously noted, we observed that electrolyses initiated at a high current generated a profusion of amorphous graphites, graphenes, and electrolyses initiated carbon nanostructures rather than a high yield of nanofibers, while electrolyses initiated with a low current step prior to the high current can generate a high yield of uniform CNFs forms. Combined with an absence of zinc metal, the absence of this low current step produced amorphous graphites (top of Fig. S5) or a profusion of nanofiber structures (bottom of Fig. S5) with diameters ranging from 0.2 to 4 µm and either circular or rectangular duct-like cross-sections. It will be of interest in future studies to isolate conditions that refine the distribution of these different structures. As previously noted,

the low current step occurs at a potential of < 0.7V, which is sufficient to form metal nucleation sites at the cathode, but is thermodynamically energetically insufficient to reduce carbonate to solid carbon.

As shown in the calculated electrolysis potentials in the top of Fig. S6, zinc is thermodynamically unusual compared to nickel, copper, cobalt or iron, in that the energy required to form zinc metal from zinc oxide is greater than the energy needed to reduce tetravalent carbon (in the form of carbon dioxide dissolved in carbonate) to solid carbon, and hence carbon will be preferentially formed from the oxide compared to zinc from the oxide. However, as also evident from the lower two curves in the figure, zinc metal is energetically sufficient to chemically spontaneously react (without the need for an applied potential), to form both solid carbon from carbonate and form nickel (or other CNT nucleation site metals) from the oxide. The experimental carbon and iron deposition onset potentials we observe are 0.5V less than the thermodynamic potentials shown in Fig. S6, which is consistent with the Nernst voltage shift associated with the large amount of dissolved reactant (tetravalent carbon or Fe(III)) that is available or may be dissolved in molten lithium carbonate. As with the reaction of Zn with nickel oxide (shown), the reactions of Zn with cobalt, iron, cobalt and copper are also exothermic (with respective electrolysis potentials E°(25°C) of -0.4, -0.6 and -1.0V).

When zinc is absent from the cathode, carbon formation initiates only at much higher (~1V or higher) potentials, leading to larger higher current density formed nucleation sites, which are not conducive to CNF confined growth and the observed profusion of mixed, amorphous graphite, graphene, and various-shaped carbon nanostructures. The presence of the zinc metal acts as a beneficial aid as it is energetically sufficient to activate both (i) the spontaneous formation of solid carbon from carbonate and (ii) the spontaneous formation of metal catalyst nuclei that aid initiation of the controlled structure growth of nanofibers at the nucleation site; zinc thereby facilitates subsequent high-yield CNF growth from the greenhouse gas CO_2 dissolved in molten carbonate. This sets the stage for base structures conducive to the subsequent high growth carbon solvation/diffusion/precipitation application of higher current densities, advantageous (to rate of formation) without hydrogen, laser ablation or plasma assistance. The preferred mechanism of high yield electrolytic CNF formation is illustrated in the right portion of Fig. S6.

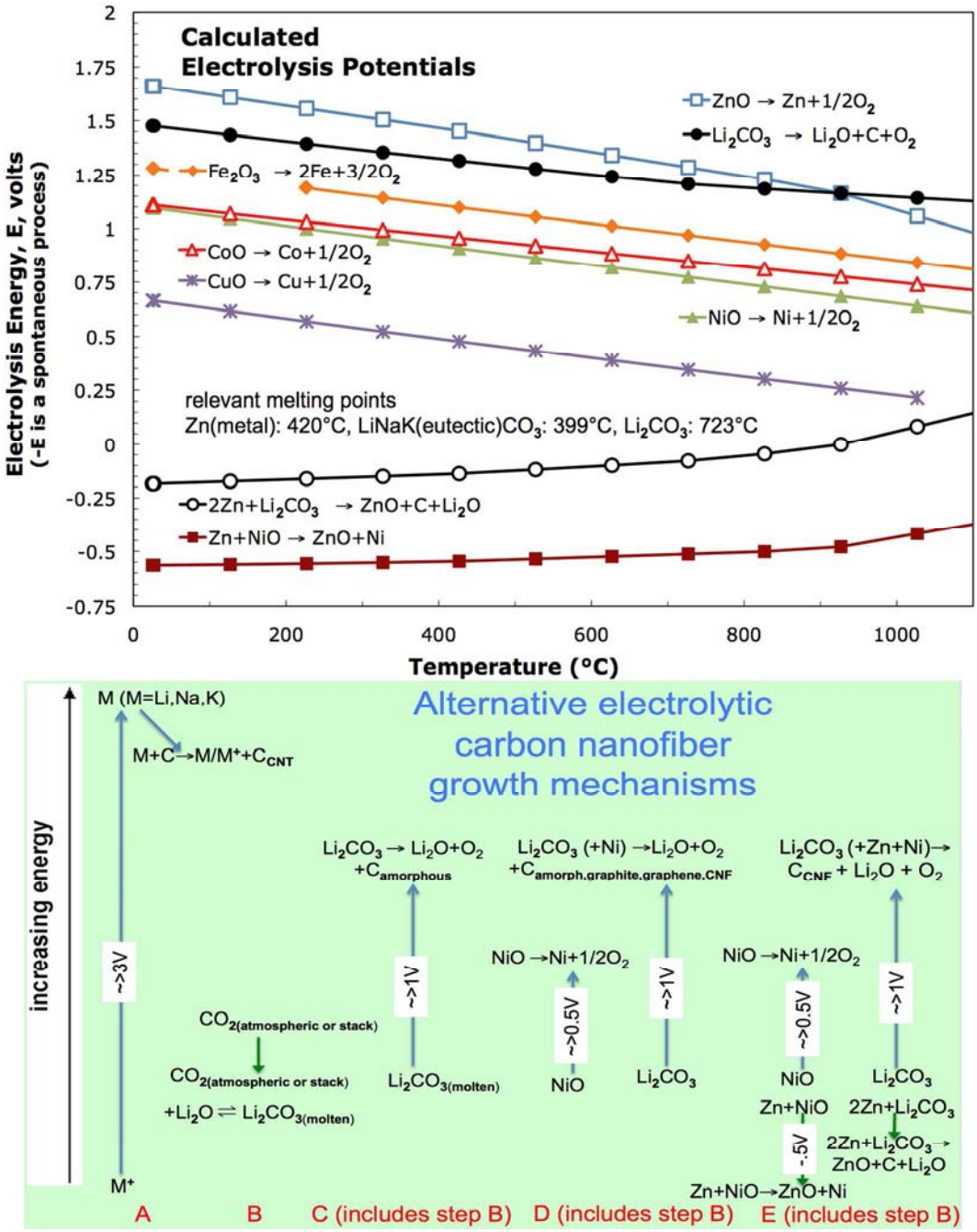

Figure S6. Left: Calculated (using thermochemical data from: reference I. Barin, Thermochemical Data of Pure Substances, part II, VCH publishers, New York, **1989**; *ibid,* part I, 3rd edition, **1995**.) electrolysis potentials relevant to the high yield electrolytic formation of CNTs from molten carbonates. The reduction of iron is shown as calculated from conventional hematite, Fe_2O_3; calculated rest potentials for the lithium soluble form, $LiFeO_2$ or magnetite Fe_3O_4 of iron oxide are similar (1.4V and 1.3V respectively at 25°C) and exhibit similar endothermic trends with increasing temperature. Right: Electrolytic CNT growth mechanisms; A: High voltage electrolysis of alkali metals followed by exfoliation and alkali intercalation into a solid carbon electrode; B: in lieu of solid carbon, spontaneous absorption of CO_2 into molten carbonate as a low voltage & greenhouse gas source of carbon; C: Lower voltage reduction of lithium carbonate; D: metal catalyst, such as nickel (shown), cobalt or iron nucleation of an assortment of carbons (including CNTs) at the cathode. E: Zn metal assisted deposition of catalyst and initial carbon to generate a high-yield of electrolytic CNTs.

V. Scalability of the CNT formation

The STEP CNF electrolysis chamber is readily scalable (Fig. S7); we have scaled from 1A to 100A using 300 cm^2 (shown) and electrode cells driven with a Xantrex XTR 0-100 A DC power supply, which scale the smaller cells both in lower carbon splitting potentials (1-1.5 V) and high (80-100 %) 4 electron coulombic efficiency of carbon product formation. The larger cells use a cylindrical galvanized steel cylinder as a cathode sandwiched within concentric, cylindrical nickel anode anodes, and as shown a hammer to separate the product from the cathode. Note that whereas 1A generates 0.1 gram of carbon per hour, the 100 A generates 10 g/h. We are currently preparing for a 660A test of a further scaled up 800 cm^2 cell.

Figure S7. Scaled-up electrolysis chamber splitting CO_2 operated at 100 amp. Driven with a Xantrex XTR 0-100 A DC power supply, 1.5V, and approaching 100% coulombic efficiency of the 4 electron reduction to carbon.

VI. High rate CO_2 splitting in carbonates at high solar efficiency

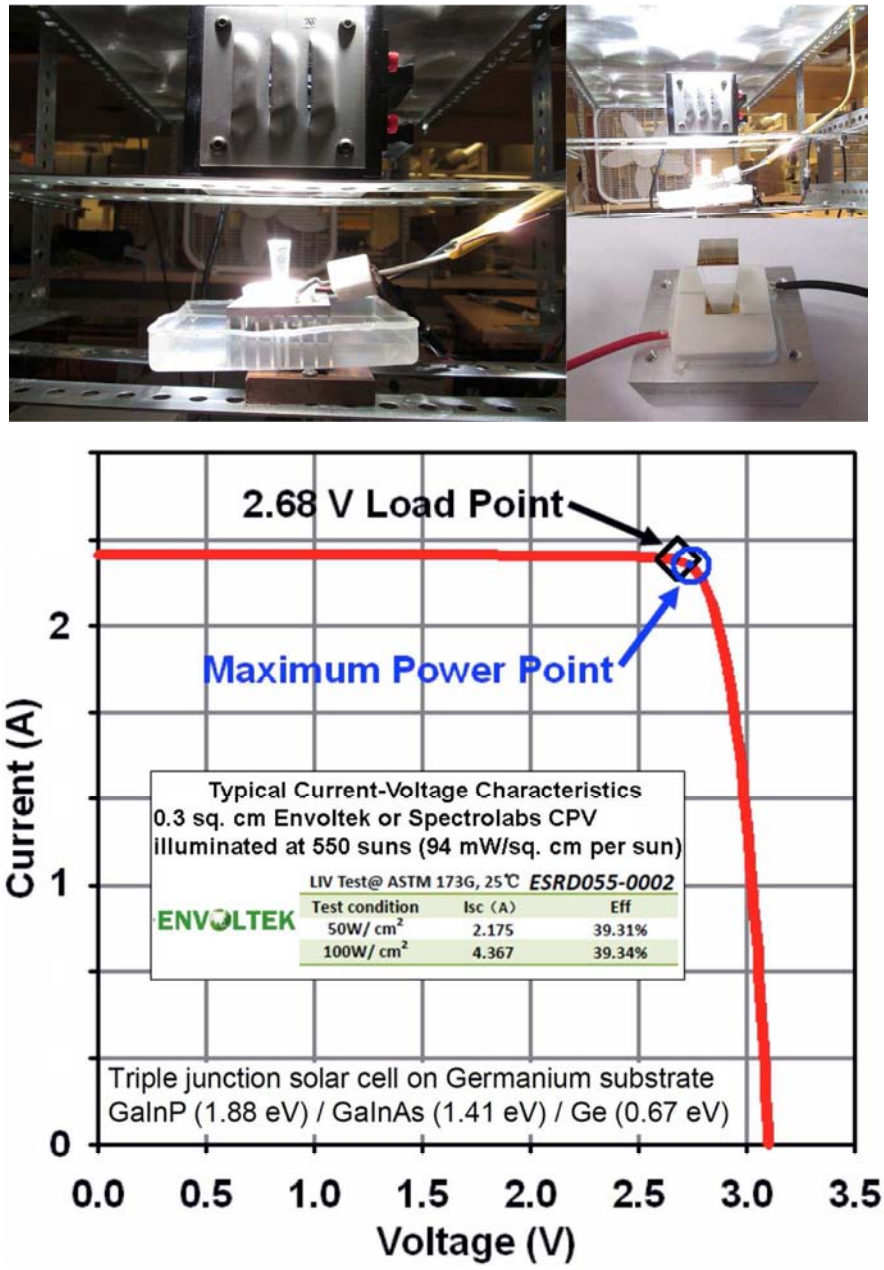

Figure S8. Concentrator photovoltaic driving CNF synthesis. Driven with a Xantrex XTR 0-100 A DC power supply, 1.5V, and approaching 100% coulombic efficiency of the 4 electron reduction to carbon.

The demonstrated CNF synthesis can be driven by any electric source. As an alternative to conventionally generated electrical, we have also driven the synthesis using electric current as generated by an illuminated efficient concentrator photovoltaic (CPV) operating at maximum power point. We have previously heated CO_2 as a reactant for the electrolysis cell by (i) initially

passing it over and under the CPV, and then (ii) heating it to the electrolysis temperature using sub-band gap (infrared) thermal light split from concentrated sunlight (via a hot mirror) prior to absorption by the CPV.[16,24] In this study, to demonstrate the efficient solar synthesis of CNFs, we use a previously characterized indoor solar simulator,[29] and a 39% solar efficient CPV operating at 550 suns concentration (Figure S8), which has a maximum power point voltage of 2.7 V to drive two in-series (1.35V x 2) CNF electrolyzers at 2.3A. STEP CNFs are efficiently formed from CO_2 in air, using inexpensive Ni and steel electrodes at high solar efficiency.

Here, we show a new high yield pathway to produce carbon nanofibers directly from atmospheric or exhaust CO_2 in an inexpensive process. Such formation of a highly valued, compact, readily stored form of carbon directly from carbon dioxide may provide a new pathway to mitigate this greenhouse gas. Today, carbon nanofibers require 30- to 100-fold higher production energy compared to aluminum production. We present the first high yield, inexpensive synthesis of carbon nanofibers from the direct electrolytic conversion of CO_2, dissolved in molten carbonates to CNTs at high rates using scalable, inexpensive nickel and steel electrodes. The structure is tuned by controlling the electrolysis conditions, such as the addition of trace nickel to act as CNT nucleation sites, limits to the electrolytic oxide concentration, inclusion of zinc, and control of current density. New infrastructure and merchandise built from CNFs would provide a repository to store atmospheric CO_2.

Science
AAAS

REPORTS

AMMONIA SYNTHESIS

Ammonia synthesis by N_2 and steam electrolysis in molten hydroxide suspensions of nanoscale Fe_2O_3

Stuart Licht,[1]* Baochen Cui,[1] Baohui Wang,[1] Fang-Fang Li,[1] Jason Lau,[1] Shuzhi Liu[1]

The Haber-Bosch process to produce ammonia for fertilizer currently relies on carbon-intensive steam reforming of methane as a hydrogen source. We present an electrochemical pathway in which ammonia is produced by electrolysis of air and steam in a molten hydroxide suspension of nano-Fe_2O_3. At 200°C in an electrolyte with a molar ratio of 0.5 NaOH/0.5 KOH, ammonia is produced at 1.2 volts (V) under 2 milliamperes per centimeter squared (mA cm^{-2}) of applied current at coulombic efficiency of 35% (35% of the applied current results in the six-electron conversion of N_2 and water to ammonia, and excess H_2 is cogenerated with the ammonia). At 250°C and 25 bar of steam pressure, the electrolysis voltage necessary for 2 mA cm^{-2} current density decreased to 1.0 V.

The Haber-Bosch process annually hydrogenates over 120 million metric tons of N_2 from the atmosphere (*1*, *2*) to produce ammonia for fertilizer (Eq. 1) (*3*). Today, hydrogen for ammonia synthesis is produced primarily through steam reformation, which consumes 3 to 5% of the world's natural gas production and releases large quantities of CO_2 to the atmosphere (*1*):

$$N_2 + 3H_2 \rightarrow 2NH_3 \quad (1)$$

$$CH_4 + 2H_2O \rightarrow 4H_2 + CO_2 \quad (2)$$

The ammonia hydrogenation reaction is separate from the steam-reforming reaction (Eq. 2) that generates the hydrogen. Renewable energy–driven water splitting could provide an alternative H_2 source, but economic, non–CO_2-emitting sources of H_2 have yet to be proven on the industrial scale. Although ammonia hydrogenation is exothermic, it is kinetically disfavored at ambient temperature and pressure. In the Haber-Bosch process, this kinetic limitation is overcome via an iron-based catalyst, repeated cycling, high pressure, and elevated temperature. The last-named conditions are energy-intensive and consume 2% of the world's energy production (*1*).

Several electrochemical processes have been pursued to provide alternative syntheses of NH_3. The electrolytic formation of nitrides from nitrogen gas in molten alkali chlorides was studied before 1980 (*4*, *5*), including subsequent reactions with hydrogen to yield ammonia, but such studies have not led yet to commercial production of ammonia because of challenges including the competing back-reaction of nitride to nitrogen (*6*–*10*). In 1985, room-temperature electrolytic synthesis of ammonia was introduced, albeit at low rates, via protolysis of $W(N_2)_2(PMe_2Ph)_4$ (*11*). Ammonia was synthesized from H_2 and N_2 in aqueous sulfate solutions using metal-phthalocyanine ($C_{32}H_{18}N_8$) complexes loaded into carbon black as a cathode and Pt loaded into carbon black as an anode, again at a low rate; note that tin, rather than iron, phthalocyanines exhibited the highest efficiency and stability (*12*). Density functional calculations have been used to evaluate hydrogen and nitrogen adsorption and/or reduction on a variety of transition metals as possible electrocatalysts in ammonia formation (*13*). The solid-state electrochemical synthesis of ammonia in two-compartment cells with either proton or oxide ion conductors has been reviewed, with the highest rate reported at 80°C and 2 V using a Nafion membrane (*14*).

There are few reports in the literature about using water or steam as a reactant in lieu of hydrogen for the electrosynthesis of ammonia, as one means to avoid the CO_2 emissions of Eq. 2. The rate of ammonia formation is lower by several orders of magnitude, and the coulombic efficiency drops to less than 1%, when water, rather than H_2, is used (*14*). One study used a strontia-ceria-ytterbia oxide proton-conducting solid electrolyte at 450° to 700°C and a Ru-based catalyst but reported that the conversions with respect to nitrogen or steam were low, primarily because of the poor conductivity of the working electrode (*15*). Using a Nafion separator in aqueous 2 M KOH with a Ru on C cathode enabled ammonia synthesis from water and nitrogen at a rate and maximum coulombic efficiency of 2.8×10^{-12} mol NH_3 s^{-1} cm^{-2} and 0.9% at 20°C and, at 90°C, a maximum rate of 2.1×10^{-11} mol s^{-1} cm^{-2} at 0.2% efficiency (*16*). Using Pt/C on a gas diffusion layer at both electrodes and room temperature Nafion as the electrolyte yielded NH_3 at a higher rate of 1.1×10^{-9} mol s^{-1} cm^{-2}, which consumed water at the anode and air at the cathode at 0.6% coulombic efficiency (*17*). Recently, ammonia was formed at 0.8% coulombic efficiency and a similar rate of 0.9×10^{-10} mol s^{-1} cm^{-2} by using Pt/C electrodes and a Nafion membrane (*18*). The related literature for alkaline electrochemical water splitting (*19*–*21*) is substantially larger than for water-air ammonia electrosynthesis. We became intrigued by a molten hydroxide (a NaOH-KOH eutectic electrolyte) ammonia fuel cell (*22*) in which $NH_{3\text{-gas}}$ (as fuel) and air reacted to produce electricity and unspecified products. A subsequent paper used the NaOH-KOH eutectic cell to split water (*23*) into hydrogen and oxygen in a manner similar to our earlier molten NaOH water splitting protocol (*24*):

$$H_2O \rightarrow H_2 + 1/2O_2 \quad (3)$$

By effectively reversing the NH_3 fuel cell, we present an electrochemical pathway to produce ammonia from air and steam at 200°C with simple materials (molten hydroxide, Ni electrodes,

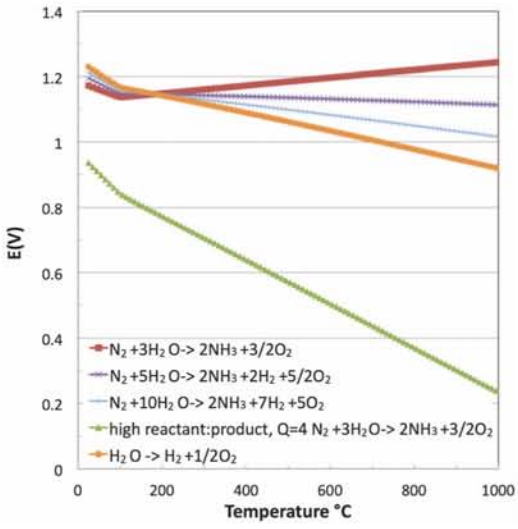

Fig. 1. Thermodynamic electrolysis potentials for water splitting and for water-based ammonia syntheses. Calculations of potentials are based on the temperature variation of the individual species' thermochemical data. The upper curves are calculated at unit activity, whereas the lower curve is calculated at a high ratio of reactants to products given by $Q = 4 = \log(10{,}000)$, that is $a_{NH3}{}^2 a_{O2}{}^{3/2} / a_{N2} a_{H2O}{}^3 = 10{,}000$. Electrolysis provides control of the relative amounts of reactant and generated product in a system. A substantial activity differential ($Q > 1$) can also lower E(V) to drive STEP improvement at elevated temperature.

[1]Department of Chemistry, George Washington University, Washington, DC 20052, USA.
*Corresponding author. E-mail: slicht@gwu.edu.

and nano-Fe_2O_3), in one pot without a separator. We reasoned that combining Eq. 3 with Eq. 1 in a highly conductive molten hydroxide for the hydrogen generation, in the presence of an appropriate ammonia-generating catalyst such as iron, should provide a one-pot medium for the electrolytic synthesis of ammonia from air and water:

$$x\mathrm{N_2} + y\mathrm{H_2O} \xrightarrow{(6x + y)e^-/h+,\ \text{iron/iron oxide, molten hydroxide}} 2x\mathrm{NH_3} + (y - 3x)\mathrm{H_2} + y/2\mathrm{O_2} \quad (4)$$

The thermodynamic potentials for water splitting and the reaction of nitrogen with water are plotted in Fig. 1; they exhibit similar redox potentials at room temperature. We also calculated alternative ammonia-producing reactions, such as the reaction of N_2 with several water molecules, shown in Fig. 1 that could occur in a molten hydroxide medium. In each case, the electrolysis potential is calculated from the known temperature variation of the entropy and enthalpies of the reactants and products by using the convention to describe the positive potential necessary to drive a nonspontaneous potential, $E_T = \Delta G(T)/nF$ (*25*–*28*), where the Gibbs free energy is calculated at a temperature (T) and n is the electrons transferred and F is Faraday's constant. On the basis of these calculations, when three H_2O molecules, rather than H_2, act as the hydrogen source for the NH_3 (Eq. 5), the potential decreases up to the water boiling point, but then increases with temperature.

$$\mathrm{N_2} + 3\mathrm{H_2O} \rightarrow 2\mathrm{NH_3} + 3/2\mathrm{O_2};$$
$$E(25°\mathrm{C}, 100°\mathrm{C}, \text{or } 750°\mathrm{C}) = 1.18\ \mathrm{V}, 1.13\ \mathrm{V}, \text{or } 1.22\ \mathrm{V} \quad (5)$$

With more than three H_2O equivalents per N_2, as in Eq. 6, hydrogen is cogenerated as a product along with ammonia, and as seen in Fig. 1, the electrolysis potential decreases with increasing water.

$$\mathrm{N_2} + 10\mathrm{H_2O} \rightarrow 2\mathrm{NH_3} + 5\mathrm{O_2} + 7\mathrm{H_2};$$
$$E(25°\mathrm{C}, 100°\mathrm{C}, \text{or } 750°\mathrm{C}) = 1.21\ \mathrm{V}, 1.15\ \mathrm{V}, \text{or } 1.06\ \mathrm{V} \quad (6)$$

The free energy and, hence, potential variation with activity, a, of the reaction is

$$\Delta G(T,a) = \Delta G°(T) + RT\ln\left[\prod_{i=1\ \text{to}\ x} a(R_i)^{r}{}_i \Big/ \prod_{i=1\ \text{to}\ y} a(C_i)^{c}{}_i\right] = \Delta G°(T) + 2.303\mathrm{RT}Q;$$

where

$$Q = \log\left[\prod_{i=1\ \text{to}\ x} a(R_i)^{r}{}_i \Big/ \prod_{i=1\ \text{to}\ y} a(C_i)^{c}{}_i\right] \quad (7)$$

R is the gas constant, T is the Kelvin temperature, and R_i and C_i represent the products and reactants. Q in Eq. 7 combines the log of the reaction quotient and n into a single term to assess the magnitude of this Nernst effect and reflects the relative activity of the reactants compared with the products. Reaction 5 yields $Q = \log(a_{NH3}{}^2 a_{O2}{}^{3/2}/a_{N2}a_{H2O}{}^3)/6$. As shown in Fig. 1, with appropriate choice of medium, this Eq. 7 Nernst effect can generate a dramatic energy decrease in the required electrolysis potential, for example, in molten electrolytes when the water reactant and nitrogen concentrations are high and the product concentration is relatively low. The effect is enhanced proportionally to the relative increases in the Kelvin temperature. Compared with $Q = 1$ in Eq. 5:

$$Q = 4\text{: } \mathrm{N_2} + 3\mathrm{H_2O} \rightarrow 2\mathrm{NH_3} + 3/2\mathrm{O_2};\ E(25°\mathrm{C}, 100°\mathrm{C}, \text{or } 750°\mathrm{C}) = 0.94\ \mathrm{V}, 0.83\ \mathrm{V}, \text{or } 0.39\ \mathrm{V} \quad (8)$$

As measured at 200°C, the molten hydroxide electrolyzer efficiently splits water, bubbled in as steam. As expected, H_2 was produced at a 2:1 ratio to O_2 when the electrolyzer did not contain nitrogen or an effective ammonia generation surface. A range of LiOH, NaOH, KOH, and CsOH eutectic mix (*29*) electrolytes (such as a molar ratio of 0.5 NaOH/0.5 KOH) were effective for water electrolysis below 300°C. The pure alkali hydroxides each melt only at temperatures above 300°C. Based on common materials, the NaOH-KOH eutectic is of particular interest and melts at 170°C. At 200°C, this electrolyte approached 100% of the electrolysis efficiency for water splitting. The variation of the water-splitting electrolysis voltage as a function of current density and temperature at 1 atmosphere was measured between planar Ni electrodes and is presented in Fig. 2. Alternative, textured, and/or alloyed electrodes and modifications of the cell configuration have been widely studied (*19*–*21*) and can decrease the electrolysis voltage at higher water-splitting current densities.

Experimentally, we observed high rates of ammonia generation when the 200°C molten hydroxide (NaOH-KOH) electrolyte was mixed with high–surface area Fe_2O_3 to provide iron as a reactive surface and when nitrogen and water vapor were in the cell. The medium was electrolyzed between a planar nickel anode and a mesh nickel–monel cathode. Initially, the H_2-evolving mesh cathode had been used to enclose the iron oxide, but the mesh openings were too large to contain the nano-Fe_2O_3. Therefore, nano-Fe_2O_3 was simply added to the electrolyte. Both water-saturated nitrogen and CO_2-scrubbed air (bubbled through a 1 M NaOH solution to remove CO_2) yielded similar efficiencies of ammonia generation. In lieu of air, 99.999% nitrogen was saturated with water at room temperature by bubbling the nitrogen through doubly deionized water en route to the electrolyzer. Unlike the water-splitting electrolysis, the efficiency of the ammonia generation by electrolysis was lower at higher current densities.

Ammonia generation by electrolysis here refers to the global reaction of nitrogen, water, and electrons to form ammonia (and oxygen), and the efficiency is calculated based on the moles of electrons consumed compared with the equivalents of ammonia ($3e^-/NH_3$) generated. This efficiency was >30% at 20 mA through 10 cm^2 electrodes compared with ~7% at 250 mA. This suggests that the conversion efficiency is not limited by the available hydrogen, but rather by the available surface area of the nano-Fe_2O_3 to promote the nitrogen and hydrogen conversion to ammonia.

The measured efficiency of ammonia evolution in time in 200°C NaOH-KOH molten electrolyte under a variety conditions is shown in Fig. 3, including a constant current of either 0 or 20 mA between the 10 cm^2 Ni electrodes. Evolved ammonia was collected and measured in a room-temperature water trap. The constant current of electrolysis was measured. The three electron equivalents of ammonia, measured as described in the supplementary material, were divided by this integrated electrolysis charge to determine the electrolysis efficiency to synthesize ammonia. The electrolysis efficiency to produce ammonia was high, in excess of 30% when we used either wet air or wet nitrogen reactants and with nano-Fe_2O_3 to provide iron as a reactive surface (*30*). This observed >30% efficiency for the conversion of electrons, air, and water to ammonia compares with the highest values of <1% previously noted for the generation of ammonia from air or nitrogen and water (*16*–*18*). The cogeneration of H_2, as measured by a Micro IV hydrogen analyzer (GfG Instrumentation) is consistent with the remaining (~65%) electrolysis current (*30*). At 20 mA applied current, the cogeneration of ammonia and hydrogen is consistent with the net reaction: $N_2 + 8H_2O \rightarrow 2NH_3 + 4O_2 + 6H_2$, but, as will be shown, the ratio of H_2 to NH_3 grows with increasing applied current. As seen in Fig. 3, ammonia is not generated if current is not applied. Iron oxide–iron mixes are catalysts for the traditional chemical synthesis of ammonia. The high surface area of the nano-Fe_2O_3 in the new electrochemical synthesis appears critical to the

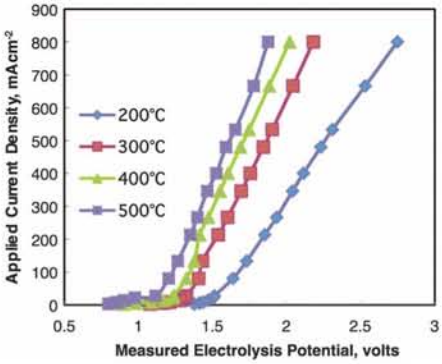

Fig. 2. Measured electrolysis potential. The measured electrolysis potential at 200°C of a molar molten mix of 0.5 NaOH/0.5 KOH at 1 atmosphere between two 2.5- by 1.5-cm planar nickel electrodes. Steam is bubbled into the cell to saturate each electrolyte with water. For example, the 200°C molten NaOH-KOH electrolyte contains ~8% weight water. At 200°C, the coulombic water-splitting efficiency approaches 100% as measured for currents of 25 to 1000 mA cm^{-2}. Water-splitting coulombic efficiency in the open air drops with increasing temperature as the molten electrolyte dehydrates with increasing temperature. At 300°C, the coulombic efficiency has dropped to ~90%, and by 500°C, the coulombic efficiency has decreased to 25%. Note that measured potentials are ~0.1 V lower when lithiated Ni anodes and monel mesh cathodes are used in lieu of planar nickel (*30*).

process. As seen in Fig. 3, the cell with no Fe_2O_3, or conventional (99.4%, J.T. Baker), rather than nanoscopic, Fe_2O_3, did not generate discernible ammonia. The 20- to 40-nm Fe_2O_3 remains colloidal throughout the electrolysis, whereas the conventional Fe_2O_3 descends and collects at the bottom of the electrolysis cell. After we milled conventional Fe_2O_3 at 300 rpm for 2 hours in a Retsch PM100 ball mill, discernible ammonia still was not generated during electrolysis, and the Fe_2O_3 still collected at the bottom of the cell. However, ball milling at 600 rpm for 2 hours, which decreased the particle size to ~200 nm, sustained a colloidal suspension throughout the electrolysis and generated a small, but discernible, quantity of ammonia at ~0.03 times the rate of the 20- to 40-nm Fe_2O_3 electrolysis cell. As delineated in the supplementary materials, when the 20- to 40-nm Fe_2O_3 was placed above (in the headspace), rather than in, the electrolyte, ammonia was not generated. Ammonia also was not generated when 20- to 40-nm Fe_2O_3 was first heated under argon to desorb any nitrogen before its addition to the molten electrolyte, and when argon (saturated with water vapor), rather than nitrogen, was bubbled into the cell during the electrolysis. However, as seen in Fig. 3, when wet (water-saturated) argon, rather than nitrogen, was bubbled into the cell, and nano-Fe_2O_3 without this desorption pretreatment was added to the electrolyte, a low level of ammonia was initially generated until nitrogen, evidently preadsorbed onto the nano-Fe_2O_3, was depleted.

Ammonia was also initially generated under conditions without water vapor in the nitrogen. However, as seen in Fig. 3, this ammonia production tapered off rapidly in time. This appears to be consistent with consumption of the molten hydroxide as an alternate source of water:

$$2MOH \rightarrow M_2O + H_2O \ (M = \text{alkali}) \quad (9)$$

In accord with Eq. 9, ammonia production continued until the molten hydroxide became dehydrated and oxide enriched.

The full cell voltage to drive molten hydroxide electrolysis of wet nitrogen or air to ammonia at 200°C in the presence of nano-Fe_2O_3 was 1.23 (±0.02) V when the applied current was 20 mA between the 10 cm^2 Ni electrodes (2 mA cm^{-2}) in the molten NaOH-KOH electrolyte; it increased to 1.44 (±0.02) V when the current increased to 250 mA (25 mA cm^{-2}), and then to 2.4 V for 2000 mA (200 mA cm^{-2}). At 2 mA cm^{-2}, under these conditions, ammonia evolved at a rate of 2.4×10^{-9} mol s^{-1} cm^{-2}, and hydrogen was cosynthesized at 6.6×10^{-9} mol s^{-1} cm^{-2}. At 25 mA cm^{-2} the ammonia synthesis rate increased to 6.7×10^{-9} mol NH_3 s^{-1} cm^{-2}, and the rate of hydrogen coproduction increased to 1.0×10^{-7} mol H_2 s^{-1} cm^{-2}. Hence, with increasing current density, the observed produced ratio of H_2 to NH_3 increased, that is the hydrogen coproduction rate increased more rapidly than the ammonia production rate, and the global (NH_3 + H_2) coulombic efficiency remained high at current densities of both 2 and 25 mA cm^{-2}. At the highest current density of 200 mA cm^{-2}, the ammonia production rate was 1.0×10^{-8} mol NH_3 s^{-1} cm^{-2}. Cesium has been observed to enhance the catalytic activity of iron and iron oxides in ammonia production (*31*, *32*). At 200°C when the NaOH-KOH electrolyte was replaced by a CsOH electrolyte (containing 30 wt % water to maintain the liquid-molten state at 200°C) the 25 mA cm^{-2} rate increased from 6.7×10^{-9} to 7.7×10^{-9} mol NH_3 s^{-1} cm^{-2}. At the measured current densities and temperature, the variation of the electrolyte cation has not been observed to affect the electrolysis potentials. The same electrolysis potentials were observed when the 0.5:0.5 NaOH-KOH molten electrolyte was replaced by a 0.48:0.52 molar ratio NaOH-CsOH, a 0.7:0.3 NaOH-LiOH, or a 0.7:0.3 KOH-LiOH eutectic electrolyte. Presumably, higher current densities and higher temperature potential will be affected by the cation, which will affect electrolyte conductivity and water retention.

The energy consumption of this ambient pressure process varies with rate (which affects the voltage) and the ammonia-only or global current efficiency (including both ammonia and hydrogen). Hydrogen cogenerated with the ammonia is not lost energy and is available for storage, or use as a fuel, or as a chemical reactant. As a first estimate of the energy consumption, we use the 1.2 V at 2 mA cm^{-2} (= 2.4×10^{-9} cm^{-2} MJ s^{-1}). This produces 2.4×10^{-9} s^{-1} cm^{-2} mol NH_3 (= 4.1×10^{-11} s^{-1} cm^{-2} kg NH_3); that is, 59 MJ is consumed per kg NH_3 produced. The energy content of the recovered H_2 is 120 to 142 MJ/kg (with or without the heat of water vaporization). This energy consumption estimate does not include the associated engineering losses, or the energy of heating to 200°C, as the optimal operating temperature needs to be determined.

In the absence of the nano-Fe_2O_3, water is simply electrolyzed into hydrogen at the cathode and oxygen at the anode in the 200°C molten hydroxide chamber. In the presence of nano-Fe_2O_3, two alternative mechanisms of the ammonia synthesis can be considered. In the first, electrochemical reduction of water to hydrogen occurs at the cathode, which then diffuses to react with adsorbed nitrogen on the nano-Fe_2O_3 surface to form ammonia. An alternative mechanism to consider is the electrochemical reduction of nitrogen and water at the nano-Fe_2O_3 to form ammonia. The latter mechanism would necessitate electron transfer from the nickel cathode to the dispersed, electrolyte-suspended nano-Fe_2O_3. The latter mechanism could be ruled out in the 200°C molten hydroxide electrolyte with the high–surface area Fe_2O_3 if ammonia were to be formed when no electrochemical current was applied, as in the case where H_2 and N_2 (rather than H_2O and N_2) were instead added as chemical reactants. That situation would preclude the electrochemical reduction of nitrogen and water at the suspended Fe_2O_3 and yet facilitate ammonia formation. It was interesting that little or no ammonia was formed in this case when gas phase H_2 and N_2, with or without O_2, were introduced to this cell without current. As one experiment, H_2 was used as the inlet reactant (with O_2, N_2, and H_2O) after generation by room-temperature electrolysis at 2000 mA in an aqueous solution of 4 m NaOH and 4 KOH. This generated gas containing 2:1 H_2 to O_2, and forming 15 ml min^{-1} of H_2, was mixed with 5 ml min^{-1} of water saturated N_2 as the inlet gas. This procedure converts the one-pot synthetic chamber into a two-pot chamber (in which hydrogen is formed by electrolysis in the preliminary room-temperature pot and bubbled into the second molten electrolyte pot through the nickel tube and nickel mesh). In this case, ammonia was formed at a marginal, but discernible, rate compared with that observed when the 2000 mA of current was applied directly to the 200°C electrolysis chamber (0.2×10^{-9} versus 1.0×10^{-8} mol NH_3 s^{-1} cm^{-2}). As a second experiment, without any electrolysis, 15 ml/min pure H_2 and 5 ml/min pure N_2 gases were bubbled through water and used as the inlet gas. Again, ammonia was only formed at a marginal, but discernible, rate (0.2×10^{-9} versus 1.0×10^{-8} mol NH_3 s^{-1} cm^{-2}). We posit that these experiments provide supporting evidence that the second mechanism (electrochemical reduction of the nitrogen and water at the nano-Fe_2O_3) of ammonia

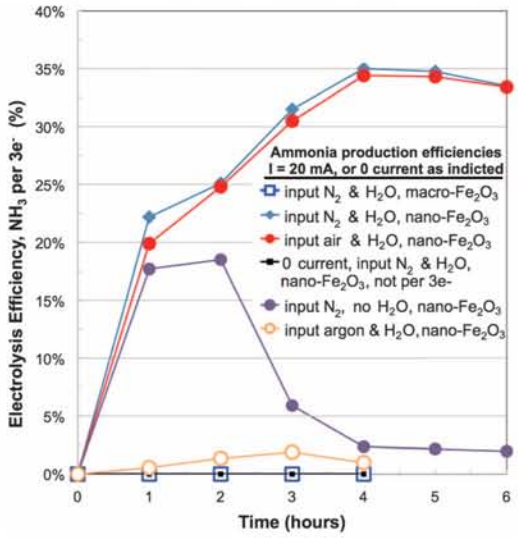

Fig. 3. Efficiency of current conversion of ammonia product. Experimental quantification of ammonia from air or nitrogen, either saturated with water or dry, by one-pot synthesis. The input gas was added to molten hydroxide at 200°C and electrolyzed in the presence of nano- or micron-sized Fe_2O_3. The indicated constant current was applied between 10 cm^2 Ni electrodes. The product gas was bubbled through a water trap quantitatively analyzed for ammonia and compared with the applied, integrated electrolysis charge to determine the electrolysis efficiency.

synthesis dominates. However, alternative factors such as a (smaller, more reactive) H_2 bubble size for the in situ generated (one-pot) versus ex situ hydrogen may contribute to the lack of the observed reaction of gas phase hydrogen to ammonia.

The simple dispersion of the nano-iron oxides in the electrolyte, as demonstrated in this study, was not conducive to long-term stability of the cell, as electrostatics tend to coagulate the nanoparticles over time. During the last 2 hours of a 200°C (NaOH-KOH) 6-hour, 2 mA cm^{-2} run, the ammonia production rate fell to 85% of its average value over the first 4 hours. Better mixing and excess nitrogen and water vapor significantly stabilized the rate. When the water-saturated nitrogen increased from 4 to 111 ml min^{-1} (retaining all other conditions at the 20 mA applied current), the ammonia production fell only 3% (to 97% of the average rate over the first 6 hours). We are exploring providing a rigid structure to immobilize the dispersed nano-iron oxides in a solid framework.

In this study, we also introduced a solar thermal water self-pressurizing, low electrolysis energy path system. Solar thermal energy is readily absorbed at conversion efficiency in excess of 65% (*33*–*35*), and here provides an efficient energy source and mechanism to maintain a high reactant pressure. Specifically, the NaOH-KOH electrolyte under N_2 gas is heated with varying amounts of water in a confined volume. As expected, heating in a constrained volume evaporates water and yields up to a demonstrated increase in water pressure from 0.03 bar at room temperature to 60 bar at 275°C, and a concurrent decrease in the ammonia electrosynthesis potential in hydroxide electrolytes as ammonia is formed, and as described in the supplementary materials (*30*). The generated high water pressure is in accord with improved high Q /low ammonia energy synthesis conditions theoretically predicted by Eqs. 7 and 8, as seen by the lower voltage curve of Fig. 1. At 250°C and 25 bar of steam pressure, the observed electrolysis potentials were 0.78V, 1.01V, and 1.31V, respectively, at 0.1, 2, and 25 mA cm^{-2}. The last-named potentials are 0.2 V more favorable than observed at ambient pressure and 200°C. The measured 2 mA cm^{-2} rate of ammonia synthesis of 2.4×10^{-9} mol cm^{-2} s^{-1} at high pressure is similar to that observed at ambient pressure, but the coproduction of H_2 is not observed at this lower potential (*30*).

There is ample room for advances of this pathway. Fe_2O_3 was utilized as the reactive surface, whereas today's Haber-Bosch catalysts use Fe_2O_3 or ruthenium-based catalysts with a wide variety of carefully optimized additives (*31*, *32*, *36*), which may also improve this electrochemical process.

REFERENCES AND NOTES

1. V. Smil, *Enriching the Earth: Fritz Haber, Carl Bosch, and the Transformation of World Food Production* (MIT Press, Cambridge, MA, 2004).
2. J. Rockström *et al.*, *Nature* **461**, 472–475 (2009).
3. R. Strait, M. Nagvekar, Carbon dioxide capture and storage in the nitrogen and syngas industries. *Nitrogen+Syngas* **303** (Jan.-Feb.), 1–3 (2010); www.kbr.com/Newsroom/Publications/Articles/Carbon-Dioxide-Capture-and-Storage-in-the-Nitrogen-Syngas-Industries.pdf.
4. A. Bonomi, M. Hadat, C. Gentaz, *J. Electrochem. Soc.* **124**, 982–986 (1977).
5. A. Bonomi, M. Hadat, F. Breda, *J. Electrochem. Soc.* **126**, 248–251 (1979).
6. T. Murakami, T. Nishikiori, T. Nohira, Y. Ito, *J. Am. Chem. Soc.* **125**, 334–335 (2003).
7. Y. Ito, T. Goto, *J. Nucl. Energy* **344**, 128–135 (2005).
8. T. Murakami, T. Nohira, Y. H. Ogata, Y. Ito, *Electrochem. Solid-State Lett.* **8**, D12–D14 (2005).
9. T. Murakami *et al.*, *Electrochem. Solid-State Lett.* **10**, E4–E6 (2007).
10. N. Serizawa *et al.*, *J. Electrochem. Soc.* **159**, E87–E91 (2012).
11. C. J. Pickett, J. Talarmin, *Nature* **317**, 652–653 (1985).
12. N. Furuya, H. Yoshiba, *J. Electroanal. Chem.* **291**, 269–272 (1990).
13. E. Skúlason *et al.*, *Phys. Chem. Chem. Phys.* **14**, 1235–1245 (2012).
14. I. Amar, R. Lan, C. Petit, S. Tao, *J. Solid State Electrochem.* **15**, 1845–1860 (2011).
15. A. Skodra, M. Stoukides, *Solid State Ion.* **180**, 1332–1336 (2009).
16. V. Kordali, G. Kyriacou, C. Lambrou, *Chem. Commun. (Camb.)* **2000**, 1673–1674 (2000).
17. R. Lan, J. T. S. Irvine, S. Tao, *Sci. Rep.* **3**, 1145 (2013).
18. R. Lan, S. Tao, *RSC Adv.* **3**, 18016–18021 (2013).
19. J. R. McKone, S. C. Marinescu, B. S. Bruneschwig, J. R. Winkler, H. B. Gray, *Chem. Sci.* **5**, 865–878 (2014).
20. D. Santos, C. A. C. Sequeira, J. L. Figueiredo, *Quím. Nova* **8**, 1176–1193 (2013).
21. K. Zeng, D. Zhang, *Progr. Energy Combust. Sci.* **36**, 307–326 (2010).
22. J. Ganley, *J. Power Sources* **178**, 44–47 (2008).
23. J. Ganley, *Int. J. Hydrogen Energy* **34**, 3604–3611 (2009).
24. S. Licht, L. Halperin, M. Kalina, M. Zidman, N. Halperin, *Chem. Commun. (Camb.)* **2003**, 3006–3007 (2003).
25. M. W. Chase, *J. Phys. Chem. Ref. Data* **9**, 1 (1998).
26. Thermochemical data from (*25*) are available online at U.S. National Institute of Standards and Technology ChemWeb: http://webbook.nist.gov/chemistry/form-ser.html.
27. Glenn Research Center, National Aeronautics and Space Administration (NASA), ThermoBuild access to NASA Glenn thermodynamic CEA database (2006); data available at www.grc.nasa.gov/WWW/CEAWeb/ceaThermoBuild.htm.
28. S. Licht, *J. Phys. Chem. C* **113**, 16283–16292 (2009).
29. A. Pelton, K. Hack (and codevelopers), *283 binary salt phase diagram*, [Facility for the Analysis of Chemical Thermodynamics (FACT), Centre for Research in Computational Thermochemistry (CRCT), University of Montreal, rev. ed., 2012]; www.crct.polymtl.ca/FACT/documentation/FTsalt/FTsalt_Figs.htm.
30. Materials and methods are detailed in the supplementary materials on *Science* Online.
31. A. Hellman *et al.*, *J. Phys. Chem. B* **110**, 17719–17735 (2006).
32. M. Appl, Ammonia 2 production processes, *Ullman's Encyclopedia of Industrial Chemistry*, doi: 10.1002/14356007 (Wiley-Verlag, Weinheim, Germany, ed. 7, 2012), pp. 139–210.
33. S. Licht, *Adv. Mater.* **47**, 5592–5612 (2011).
34. R. Pitz-Paal, in *Solar Energy Conversion and Photoenergy Systems*, J. B. Galvez, S. M. Rodriguez, Eds. (EOLSS Publishers, Oxford, 2007).
35. T. Hahm, H. Schmidt-Traub, B. Leßmann, *Sol. Energy* **65**, 33–41 (1999).
36. W. Ziqing, Z. Kiuming, L. Jianxin, W. Rong, W. Kemei, *J. Catal.* **33**, 377–378 (2013).

ACKNOWLEDGMENTS

Full materials and methods and a section on solar thermal–constrained volume pressurization are presented in the supplementary materials. The authors are grateful for partial support of this research by the Office of Naval Research (award N00014-13-1-0791). A related provisional U.S. patent has been filed.)

SUPPLEMENTARY MATERIALS

www.sciencemag.org/content/345/6197/637/suppl/DC1
Materials and Methods
Supplementary Text
Figs. S1 to S5
Table S1
References

1 April 2014; accepted 23 June 2014
10.1126/science.1254234

www.sciencemag.org/content/345/6197/637/suppl/DC1

Supplementary Materials for

Ammonia synthesis by N_2 and steam electrolysis in molten hydroxide suspensions of nanoscale Fe_2O_3

S. Licht,* B. Cui, B. Wang, F.-F Li, J. Lau, S. Liu

*Corresponding author. E-mail: slicht@gwu.edu

Published 8 August 2014, *Science* **345**, 637 (2014)
DOI: 10.1126/science.1254234

This PDF file includes

Supplementary Materials

Ammonia synthesis by N_2 and steam electrolysis in molten hydroxide suspensions of nanoscale Fe_2O_3

Stuart Licht,[1]* Baochen Cui,[1] Baohui Wang,[1] Fang-Fang Li,[1] Jason Lau,[1] Shuzhi Liu[1]

Materials

Anhydrous sodium hydroxide (Sigma-Aldrich S5881), potassium hydroxide (sigma-aldrich P1767, KOH•½H_2O), cesium hydroxide (99.9% CsOH•1-2H_2O Alfa-Aesar 13233) and lithium hydroxide (anhydrous, 98%, Acros Organics 37918) are combined to form various eutectic molten hydroxide electrolytes each with melting points < 300°. The pure anhydrous akali hydroxides each melt only at temperatures > 300°C; LiOH (T_{mp} = 462°C), NaOH (T_{mp} = 318°C), KOH (T_{mp} = 406°C), CsOH (T_{mp} = 339°C). Whereas, molar ratios of 0.3:0.7 LiOH/NaOH, 0.3:0.7 LiOH/KOH, 0.5:0.5 NaOH/KOH, 0.44:0.56 KOH/CsOH, respectively melt at 215°C, 225°C, 170°C and 195°C (*22*), and are even lower when hydrated hydroxide salts are used. Conventional microscopic (99.4%, JT Baker) or high surface area nanoscopic (20-40 nm particle, 30-60 m^2/g AlfaAesar 45007, NanoArc; used lot L20Y042: Alfa Aesar Certificate of analysis, 99.9% iron oxide, 35 nm average particle size, 33 m^2 g^{-1} BET) Fe_2O_3 are added to the molten hydroxide electrolyte to promote ammonia formation.

Gas input to the electrolysis chamber consisted of either A: wet (1) 99.999% nitrogen (ultra high purity nitrogen generator 3000 cc/min Dominick Hunter G2-110W), or (2) Ar, bubbled through double deionized water to water saturation at room temperature (2.6% water at 22°C), or (3) air bubbled through a 1 M KOH solution to remove carbon dioxide and saturate with water at room temperature, B: the dry gases. Gas flow was maintained at 4.1 ml min^{-1} in the 20 mA electrolyses and 111 ml min^{-1} in the 250 mA electrolyses. For mass balance the wet (water saturated) gases provide sufficient water ($8x10^{-8}$ or $2x10^{-6}$ mol H_2O/s, respectively) for the hydrogen generation component of the electrolysis and excess nitrogen. It is a challenge to design higher input gas flow rates into the current cell design, and the 2000 mA experiment is conducted with flow of 222 (and also a slow flow experiment of 2.2) ml min^{-1}. The latter, 2000 mA slow flow 2.2 ml min^{-1} experiment constrains steam and nitrogen entering the cell and yields only 0.62 of the initial ammonia production rate of the fast flow experiment, and respectively after 4 or 6 hours exhibited an ammonia rate of only 13% or 5% of the initial two hour average rate. As described in the text, excluding either nitrogen or water from the cell decreased (zeroed) the ammonia output from the electrolysis cell. The electrolysis is conducted in a pure alumina crucible (AdValue, 99.6%). In the alumina crucible cell, the anode consists of a pure Ni (McMaster 200) shim cut to 10 cm^2, the 10 cm^2 Ni cathode consists of 200 mesh woven wire cloth (Alloy 400, Monel, McMaster 9225T361). This Monel cathode mesh is stable in the molten 200°C hydroxide, whereas 316 stainless steel mesh is observed to (slowly) react forming hydrogen. The electrodes are connected externally by spot welded Ni wire (99.5% Alfa Aesar 41361).

Calculations

Thermodynamic electrolysis potentials for water splitting and ammonia synthesis with water are calculated from the unit activity thermochemical data for the individual species, using the convention to describe the positive potential necessary to drove a non spontaneous potential (*19-21*), from the reactions: $\sum_{i=1 \text{ to } x} r_i R_i \rightarrow \sum_{i=1 \text{ to } y} c_i C_i$; using

$E_T = \Delta G(T)/nF$

and $\Delta G°(T) = \sum_{i=1 \text{ to } y} c_i(H°(C_i,T)-TS°(C_i,T)) - \sum_{i=1 \text{ to } x} r_i(H°(R_i,T)-TS°(R_i,T))$.

Electrolysis provides control of the relative amounts of reactant and generated product in a system. A substantial activity differential can also drive **STEP** improvement at elevated temperature. The free energy and hence potential variation with activity, a, of the reaction is,

$$\Delta G(T,a) = \Delta G°(T) + RT\ln\left(\left(\prod_{i=1 \text{ to } x} a(R_i)^{r_i} / \prod_{i=1 \text{ to } y} a(C_i)^{c_i}\right)\right)$$

$$= \Delta G°(T) + 2.303RTQ; \text{ where } Q = \log\left(\left(\prod_{i=1 \text{ to } x} a(R_i)^{r_i} / \prod_{i=1 \text{ to } y} a(C_i)^{c_i}\right)\right)$$

Methods

A single chamber electrolysis configurations was used to electrolyze water saturated air or N_2 to NH_3. In addition a double chamber cell configuration was only used to confirm that ammonia was separately generated at the cathode and oxygen at the anode. The latter configuration is described in the subsequent paragraph. The single chamber configuration is photographed in Fig. S1. A stainless steel (316 alloy) cover is cut with a groove on the lower side that matches the circumference of the alumina crucible (100 ml alumina crucible Advent AL-2100). The cover to crucible seal is gas-leak free when the groove is filled with a high temperature adhesive (Resbond 907 heavy grade adhesive) and the cover is compressed to the crucible by four outer bolts through the cover and a bottom plate as seen in the figure. 0.25" Inconel (McMaster 89865K) or alumina tubes (McMaster 8746K) pass through the cover into the electrolyzer, and are gas-leak free when sealed with the Resbond 907. The middle alumina tube becomes the outlet gas exit, which is bubbled through an ammonia trap (described below). The anode connecting wire seen on the left is in an alumina tube. The inconnel tube, seen on the right side, functions as both the cathode electrical connection and as the gas inlet. Either N_2 or air, and water vapor enters through this inlet The anode and cathode tubes are also sealed at the cover with Resbond 907 adhesive In addition the cathode tube is connected to the inlet gas (either N_2 or air and water vapor). The cell is situated within a 1700 W Band Heater (McMaster 8160T21), and insulated by (1) alumina silica ceramic fiber ultra high insulation with an aluminum facing on one side (McMaster 9379K93) and (2) rigid thermal shock resistant ceramic insulation without binder (McMaster 9359K75). Temperature is monitored by thermocouple and controlled by DIN Compact Temperature Controller (Omega CN2100-R20). The full cell voltage to drive molten hydroxide electrolysis of wet N_2 or air to ammonia at 200°C in the presence of nanoscopic Fe_2O_3 is 1.2V when the applied current is 20 mA between the 10 cm^2 Ni electrodes, and increases to 1.4 V when the current is increased to 250 mA. In each case, when current is applied

the electrolysis potential rises from 0V to 60% of the final voltage within the initial 30 seconds of electrolysis, and to 80% of the final potential within the first 5 minutes of the electrolysis. We observe that Ni, Pt (*18*) and lithiated Ni (*17*) are effective anodes. The lithiated Ni is prepared by anodization at 1 mA cm^{-2} for 24 hours in 100°C 3M LiOH, and drives the electrolysis at a ~0.07V lower potential. However, in this study, commercial, pure (Ni 200) shim is employed as the anode to demonstrate ease of process. At these current densities and temperature, variation of the cation has not been observed to affect these electrolysis potentials. The same electrolysis potentials are observed when the equimolar NaOH/KOH molten electrolyte, is replaced by an 0.48:0.52 molar ratio NaOH/CsOH, an 0.7:3 NaOH/LiOH, or an 0.7:3 KOH/LiOH eutectic electrolyte. Presumably, higher current densities and higher temperature potential will be affected by the cation, which will affect electrolyte conductivity and water retention.

The product gas from the electrolysis chamber is bubbled (sparged) through an ammonia trap containing 500 ml doubly deionized water, changed regularly for ammonia analysis. Ammonia concentration was determined by triple redundant methodologies (1) UV/vis absorption, (2) ion selective electrode analysis (Hach 2348700 Ammonia ISE Analysis package) and (3) ammonia test strips (Hach 2755325, dilution required on more concentrated samples). In each case, redundant measurements yield similar ammonia measurements, with the observed reproducibility of first two methodologies $\pm$2% and the test strips to $\pm$5%. Initially, two water traps (in series) were used to probe whether all ammonia was collected by the first water trap. No ammonia was measured in the second water trap, even under high ammonia production conditions, and only a single water trap was used in subsequent experiments. A (single 500 ml) millimolar acid water trap was also effective. High ammonia concentrations required a dilution prior to analysis by the ammonia test strips. The ammonia ISE is calibrated with a series of $NHCl_4$ solutions, and 2 ml pH of ionic strength adjustor (Orion ISA 951210) added to 100 ml of analyte. The ammonia ISE responds quickly to moderate and high ammonia concentrations, however required several minutes to reach a limiting voltage (concentration) when analyzing dilute ammonia concentrations. Hence, UV/vis was the preferred method of analysis. The UV/vis ammonia determination is measured by absorption at 697 nm on Perkin Elmer Lambda 35 in a conventional 1 cm path length cuvette by the salicylic method, as calibrated with standard aqueous ammonium chloride (NH_4Cl) solutions. The method is delineated in reference 30, and in brief absorption is measured following the additions of 0.36 M salicylic acid ($C_6H_4(OH)COOH$) in 0.32 M aqueous NaOH, aqueous 0.032 sodium nitroprusside ($Na_2[Fe(CN)_5NO]\bullet 2H_2O$), and 0.1M sodium hypochlorite (NaClO) in 0.75 M aqueous NaOH. Ammonia measured under a variety of discharge conditions is presented in Table S1.

H_2 was measured directly by a Micro IV hydrogen analyzer (GfG Instrumentation) or, in the case of high hydrogen concentrations, following serial dilution by added nitrogen; at lower N_2 inlet flow rates, H_2 was redundantly determined by the volume of H_2 & O_2 gas collected (after corrections for the partial volumes of N_2 and H_2O_{vapor}). H_2 was redundantly measured, along with O_2, by GC (HP 5890 series II gas chromatograph) with 3 ml/min argon flow using a Carboxen-1010 column, injecting a 250µL sample, which yields H_2 and O_2 peaks respectively at 2.15 and 3.7 minutes.

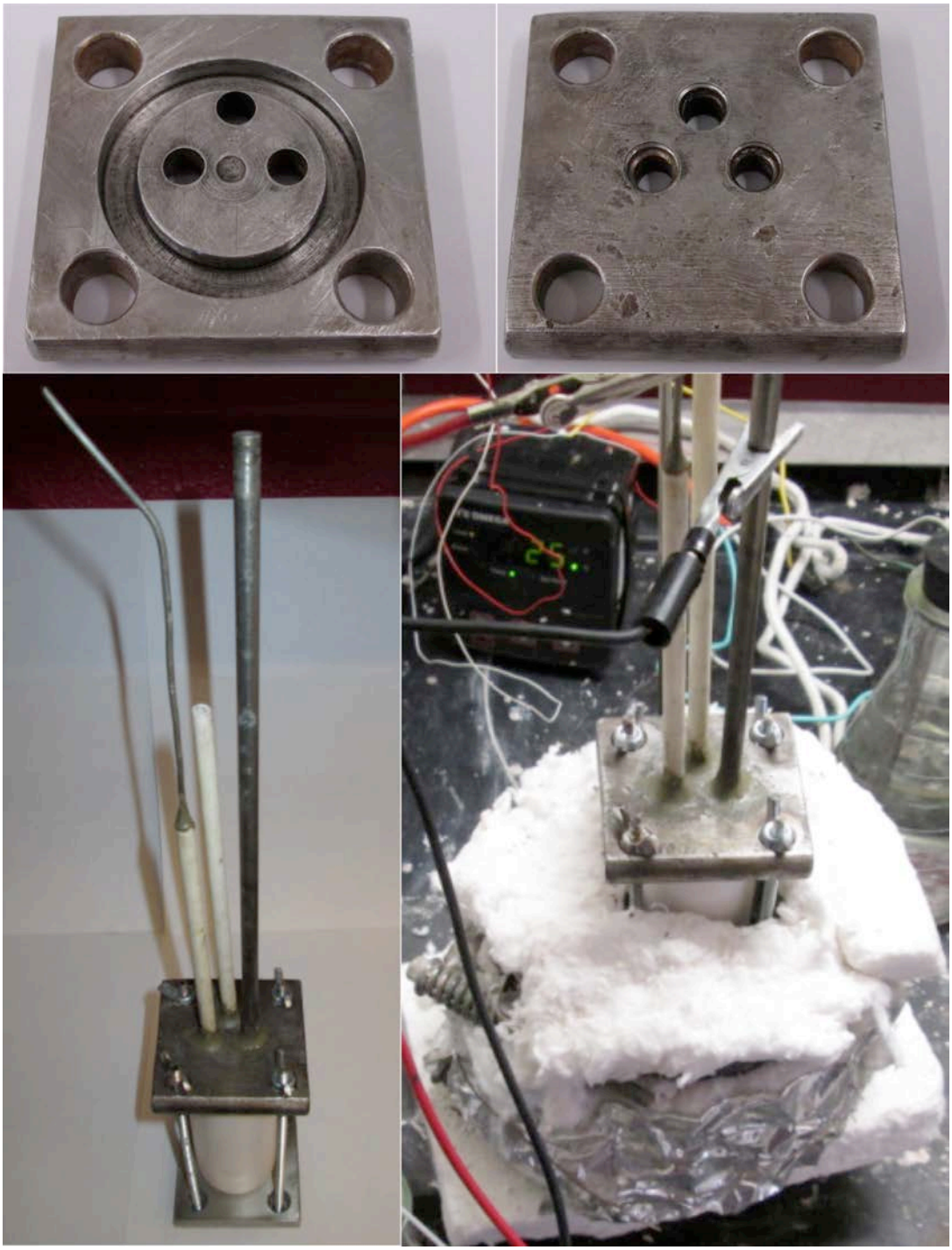

Fig. S1. The single chamber electrolysis cell configuration as described in the text and used to confirm that ammonia was produced at the cathode and oxygen at the electrode. Top left and right photos: underside and top of cell cover. Bottom left: alumina crucible situated in the cover groove and bolted closed. Above the cell, from left to right is the electrical connection of the anode that is sheathed in alumina, the alumina gas outlet, and on the right side an Inconnel tube functioning as both the gas inlet & the cathode electrical connection. Bottom, right: the electrolyzer sitting within the band heater (not visible) and surrounded by insulation.

Table S1. Measured ammonia produced as a function of time in the Fig. S1 electrolysis cell at either 0 or 20 mA applied current and at 200°C in a molten Na/KOH electrolyte. In the table NH_3 is the mg of measured NH_3 analyzed as detailed in the text. EE is the electrolysis efficiency, that is $NH_3/3e^-$ (%) calculated from the charge, q, and measured ammonia as: 100%*mol NH_3/(q /3). In the case of q =0, EE =NH_3 (measured). Nano-Fe_2O_3 above the electrolyte (columns 14 & 15) is maintained in the headspace, and kept separate from the electrolyte by fiber alumina wool. Specifically, three cm above the molten electrolyte a platform was formed in the headspace of the electrolysis chamber which consisted of (i) Ni shim pierced with holes and covering the diameter of the alumina crucible, (ii) fine (400) 316 stainless mesh, and (iii) Cotronics 300 porous alumina paper with through holes for the alumina tubes covering the electrodes, (iv) then the nano-Fe_2O_3, (v) a top layer of Cotronics 300 porous alumina paper, and finally packed with (vi) high temperature fiber alumina wool (McMaster 9379K93 with foil-face removed).

current:	I= 0 mA	I = 20 mA	macro-Fe_2O_3		nano-Fe_2O_3		nano-Fe_2O_3 Ar preheated		nano-Fe_2O_3		nano-Fe_2O_3		nano-Fe_2O_3, above, not in, electrolyte		nano-Fe_2O_3	
additive:	nano-Fe_2O_3															
inlet gas:	wet N_2		wet N_2		wet Ar		wet Ar		dry N_2		wet N_2		wet N_2		wet air	
Time (hr)	NH_3	q,Faraday	NH_3	EE	NH_3	EE	NH_3	EE	NH_3	EE	NH_3	EE	NH_3	EE	NH_3	EE
0	0 mg	0.00E+00	0 mg	0%	0.00	0%	0.00	0%	0.00	0%	0.00	0%	0.00	0%	0	0%
1	0 mg	7.46E-04	0 mg	0%	0.02	0.6%	0.00	0%	0.75	17.7%	0.94	22.2%	0.00	0%	0.84	19.9%
2	0 mg	7.46E-04	0 mg	0%	0.06	1.4%	0.00	0%	0.78	18.5%	1.06	25.1%	0.00	0%	1.05	24.8%
3	0 mg	7.46E-04	0 mg	0%	0.08	1.9%	0.00	0%	0.25	5.9%	1.33	31.5%	0.00	0%	1.29	30.5%
4	0 mg	7.46E-04	0 mg	0%	0.04	1.0%	0.00	0%	0.10	2.4%	1.48	35.0%	0.00	0%	1.46	34.4%
5	0 mg	7.46E-04	0 mg	0%					0.09	2.2%	1.47	34.8%			1.45	34.3%
6	0 mg	7.46E-04	0 mg	0%					0.08	2.0%	1.42	33.5%			1.41	33.4%

A second, double chamber cell is shown in Fig. S2. An alumina crucible (not shown) sits in the outer groove of the cell cover, while an inner alumina tube sits in the inner groove. The outer chamber, situated between the crucible and the inner alumina tube contains an Inconnel tube (left side) which functions both as an inlet of water saturated air or nitrogen, and as an electrical connector for the nickel 400 mesh cathode. The outer chamber also contains an alumina tube outlet to one (of two) water traps for gas analysis. The inner chamber, situated within the alumina tube, contains the nickel anode connected externally by a nickel wire sheathed in an alumina tube, as well as a second alumina tube outlet to the second water trap for gas analysis. This configuration exhibits higher cell voltages due to the long electrolyte path between anode and cathode and was only used to confirm that ammonia was produced at the cathode and oxygen at the anode. While this configuration exhibits higher cell voltages, it is interesting to note that we never observed an improvement in efficiency (that is we did not observe an increase in the ammonia produced) in these experiments in which oxygen was partially (with air as the inlet gas) or fully (with nitrogen as the inlet gas) excluded from the cathode chamber, which suggested that there is no observable reaction of ammonia with oxygen in the 200°C molten hydroxide electrolyte.

Fig. S2. The double chamber electrolysis cell configuration as described in the text and used to confirm that ammonia was produced at the cathode and oxygen at the electrode. Top left and right photos: underside and top of cell cover. Bottom photos, left: alumina tube with cathode outside and anode inside, prior to addition of electrolyte and outer crucible. Right: Double chamber cell prior to closure with bolts showing from right to left inconnel tube for gas inlet & cathode electrical connection, outer chamber gas outlet, inner chamber electrical connection to anode, and inner chamber gas outlet.

The electrolyzer current was supplied by power supply in initial experiments and is now provided by an efficient concentrator photovoltaic in lab under 1 kW Xenon, daylight color (5600K) AM1(air mass) illumination as described in Fig. S3.

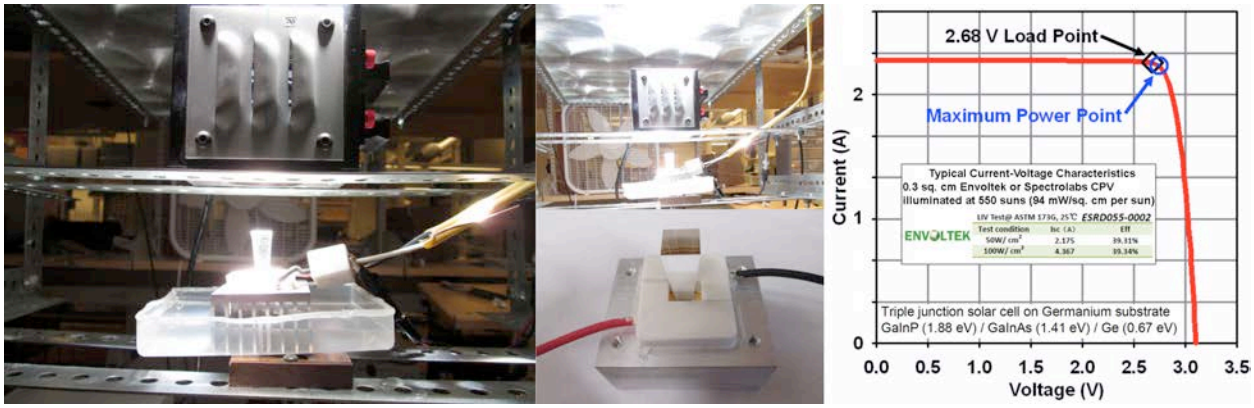

Fig. S3. Electrolyzer current by power supply (initial experiments) and now provided by an efficient concentrator photovoltaic in lab under 1 kW Xenon, daylight color (5600K) AM1(air mass) illumination. Left side is the 0.3074 cm^2 Envoltek ESRD055 CPV situated under the air-cooled AM1 filter. Middle top: The fresnel concentrator above the AM 1 filter. Middle bottom: the unattached CPC under the secondary optical concentrator. Right side: Typical (550 sun) photocurrent - voltage plot of the CPV.

Solar Thermal Constrained Volume Pressurization

A low energy route to solar energy conversion. In this study we also introduce a solar thermal water self-pressurizing, low electrolysis energy path system. The solar generated high pressure of the reactant gas phase equilibrates with gas or molten phase reactants to decrease the electrochemical potential required for endothermic electrolyses. Sunlight provides the energy to evaporate a reactant in a constrained volume, driving the reactant to high pressure as shown (for H_2O) in Scheme S1 (alternatively, the higher pressure H_2O can be used to compress a piston to pressurize a reactant such as N_2 in air). The sunlight also provides higher temperature, which further decreases the electrolysis splitting energy. Solar thermal energy is readily absorbed at conversion efficiency in excess of 65%, and here provides an efficient energy source and mechanism to maintain a high reactant pressure. Hence the energy needed to split water or electrochemically synthesize molecules can be substantially decreased by sunlight. Specifically here, pure water or an NaOH:KOH electrolyte, was enclosed with air and heated in a confined volume.

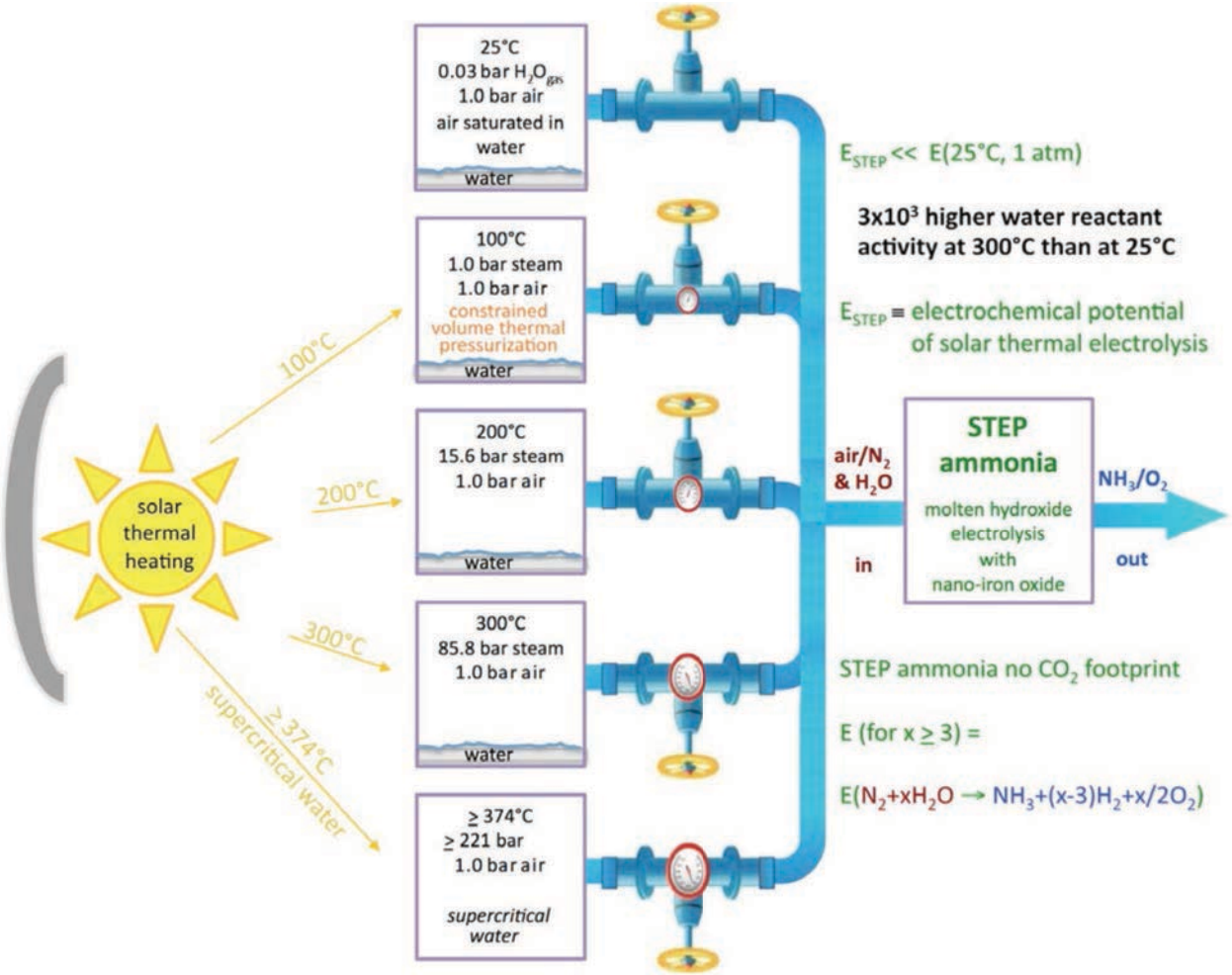

Scheme S1. The pressure of water saturating 1 bar of air, without or with solar heating in a constrained volume, as a feedstock for STEP ammonia production. Note, that dry air's composition is 78.08% N_2, 20.95% O_2, 0.93% Ar, and other lower concentration gases; alternatively a pure N_2 feedstock can be considered instead of air.

As expected, heating volume constrained water yielded a demonstrated increase in water pressure from 0.03 bar at room temperature to 60 bar at 275°C measured in the 200 ml constrained volume experimental cell (a modified hydrothermal reaction chamber) shown in Fig. S4. The generated high water pressure is in accord with improved high Q /low energy ammonia synthesis conditions theoretically predicted by Eq 7 & 8, seen in the lower voltage curve of Fig. 1 of the main text.

Fig. S4. High-pressure cell used to measure saturated water pressure as a function of temperature. The Tech-zoom stainless steel reactor has an inner 200ml Teflon chamber (top shown as used to measure saturated water pressure), and (bottom) is shown as in-house modified for electrolysis by replacement of the right-hand flow valve with throughput electrical contacts using an OMEGA MFT-116-3 Feedthrough for up to three 1/16" diameter probes with a ¼" NPTM fitting.

In addition to water as shown in Scheme S1, we directly heated water/hydroxide mixtures in the Fig. S4 modified hydrothermal reaction chamber shown in the Methods section. Pure water in a constrained environment will achieve a pressure of 85.8 bar at 300°C (*31*). As seen in in Fig. S5, a KOH mix containing 50% water (an 18m KOH aqueous solution) will achieve 30 bar in a constrained environment (a substantial portion of the water is bound by the KOH). The 1:1 molar NaOH:KOH used in the main portion of this study is a low melting point eutectic but at 1 bar retains relatively low concentrations of water (<8%) at 200°C. In order to achieve water-saturation pressures that can decrease the electrolysis energy, higher concentrations of water are required. As seen in the figure we measure that a 1:1 molar ratio of NaOH to KOH when containing 67 % water (an aqueous solution that is 4 molal in both NaOH and KOH) does rise to a water pressure of over 50 bar when heated to 300°C. In comparison, as seen in the figure, the variation with temperature of this saturated water pressure is similar, but slightly less, than that previously observed above pure 8 m NaOH or pure 8m KOH solutions.

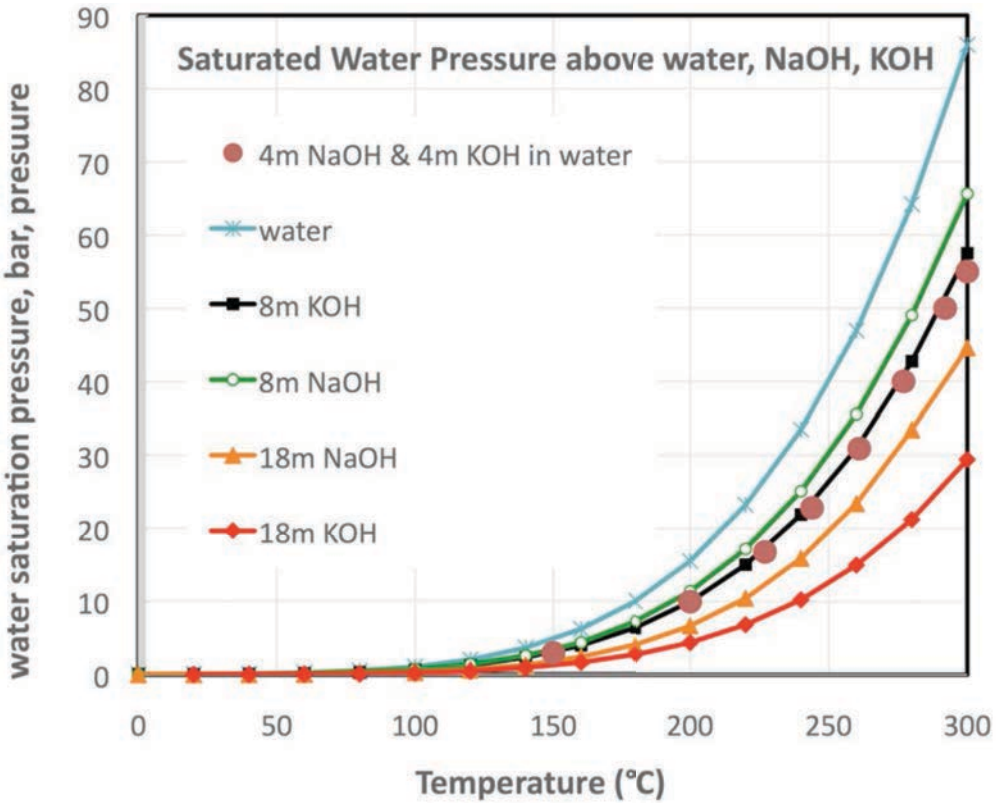

Fig. S5. The measured water pressure above a 4 molal NaOH + 4 molal KOH aqueous solution (a mix containing a 1:1 molar ratio of NaOH to KOH and 72.2 mass percent water) compared to the known (*31*) experimental saturated water pressures above water, 8 or 18 m NaOH, and 8 or 18 m KOH.

In principle, the heat required to raise the aqueous hydroxide mix is low (the heat capacity for water, NaOH and KOH varies from C_p = 1 to 4 J g^{-1} K^{-1} with temperature). To safely constrain the pressure, the Teflon lined stainless steel 200 ml reaction chamber used in this study is massive (5 kg) compared to the 70g mass of the heated hydroxide

solution, which provides a challenge to heating the chamber solely with solar energy. However demonstrating that solar thermal is sufficient, is that outdoors 60 to 70 g of an alkali eutectic salt consistently reaches and sustains temperatures of 500°-700°C, and 30 g reaches over 700°C, with (Edmund Optics) Fresnel lens concentrator under Washington DC sunlight.

We kept the temperature of Fig. S4 high-pressure cell at or below 300°C, as the decomposition temperature of Teflon is 325°C. We observe that the Teflon lining began to soften or deform at temperatures over 300°C. In accord with Scheme S1, high water content, closed contained electrolyses provide an opportunity to increase the saturated water pressure above the mNolten phase reaction by three orders of magnitude by increasing the temperature from 25°C to 300°C. These conditions provide the opportunity to explore the capability of solar thermal energy to decrease the electrolysis potential needed to drive water reactant electrolyses such in the ammonia synthesis reactions Eqs. 4-8.

In experiments in the volume constrained cell with externally connected electrodes shown on the right side of Fig. S4, the potential between Ni electrodes in an 8 m hydroxide ammonia synthesis electrolyte (4m NaOH, 4 m KOH, nano-Fe_2O_3) decreased with increasing temperature providing initial supporting evidence of the predicted high Q, low potential ammonia synthesis potential calculated in Fig. 1 of the main text. Specifically at 250°C and 25 bar under volume constrained conditions using the Fig. S4 cell, measured electrolysis potentials are lower than those measured at atmospheric pressure and lower temperature, and the ammonia generation rate and current efficiency is higher. Measured potentials over the 10 cm^2 electrodes at higher temperature and pressure were 0.78V at 1 mA, 1.01V at 20 mA (compared to 1.23V at ambient pressure and 200°C), and 1.31V at 250 mA (compared to 1.44V at ambient pressure and 200°C). The cell was then maintained at 20 mA (2 mA cm^{-2}) for 10 hours, and regularly (every ~2 hours) vented through a sparger/water trap to analyze for ammonia and the gas analyzed for hydrogen. Compared to the 200°C, 1 atm experimental results, the 250°C, 25 bar results require significantly lower electrolysis voltage, while coulombic efficiency and peak ammonia rate are the same 35% and 2.4 x 10^{-9} mol NH_3 cm^{-2} s^{-1}. Interestingly however, no hydrogen co-product was detected during the course of the experiment. At 250°C and 25 bar the ammonia production rate varied with time as 2.1 x 10^{-9} (hours 0 to 2.5), 2.2 x 10^{-9} (hours 2.5 to 5), 2.4 x 10^{-9} (hours 5 to 8), and then dropped to 1.6 x 10^{-9} (hours 8 to 10). In each case the pressure increased from 25 bar prior to venting. The cell was allowed to increase in pressure to 39 bar subsequent to the first vent/ammonia analysis, and then vented at 35 to 36 bar subsequently through 8 hours of electrolysis time. During hours 8 to 10, the rate of pressure build-up in the cell slowed and only increased from 25 to 28 bar during this two hour interval. Concurrent with the measured decrease in ammonia rate during this time interval was an increase in voltage (from 1.01 V to 1.11V).

As expected, we observe that using water evaporation in a closed container increases the electrolysis cell pressure, and in addition we observe that this induces a significant decrease in the energy (electrolysis voltage) measured to drive ammonia production. It should be noted that the lack of an observed hydrogen co-product at high pressure during ammonia synthesis at 2 mA cm^{-2} represents a loss of this fuel as a co-product.

References

1. V. Smil, *Enriching the Earth: Fritz Haber, Carl Bosch, and the Transformation of World Food Production* (MIT Press, Cambridge, MA, 2004).

2. J. Rockström, W. Steffen, K. Noone, A. Persson, F. S. Chapin 3rd, E. F. Lambin, T. M. Lenton, M. Scheffer, C. Folke, H. J. Schellnhuber, B. Nykvist, C. A. de Wit, T. Hughes, S. van der Leeuw, H. Rodhe, S. Sörlin, P. K. Snyder, R. Costanza, U. Svedin, M. Falkenmark, L. Karlberg, R. W. Corell, V. J. Fabry, J. Hansen, B. Walker, D. Liverman, K. Richardson, P. Crutzen, J. A. Foley, A safe operating space for humanity. *Nature* **461**, 472–475 (2009). Medline doi:10.1038/461472a

3. R. Strait, M. Nagvekar, Carbon dioxide capture and storage in the nitrogen and syngas industries. *Nitrogen+Syngas* **303** (Jan.-Feb.), 1–3 (2010); www.kbr.com/Newsroom/Publications/Articles/Carbon-Dioxide-Capture-and-Storage-in-the-Nitrogen-Syngas-Industries.pdf.

4. A. Bonomi, M. Hadat, C. Gentaz, Galvanic cell studies on ionic carbide and nitride solutions in molten salts. *J. Electrochem. Soc.* **124**, 982–986 (1977). doi:10.1149/1.2133513

5. A. Bonomi, M. Hadat, F. Breda, Electrochemical studies on ionic nitride solutions in molten salts. *J. Electrochem. Soc.* **126**, 248–251 (1979). doi:10.1149/1.2129013

6. T. Murakami, T. Nishikiori, T. Nohira, Y. Ito, Electrolytic synthesis of ammonia in molten salts under atmospheric pressure. *J. Am. Chem. Soc.* **125**, 334–335 (2003). Medline doi:10.1021/ja028891t

7. Y. Ito, T. Goto, Electrochemistry of nitrogen and nitrides in molten salts. *J. Nucl. Energy* **344**, 128–135 (2005).

8. T. Murakami, T. Nohira, Y. H. Ogata, Y. Ito, Electrolytic ammonia synthesis in molten salts under atmospheric pressure using methane as a hydrogen source. *Electrochem. Solid-State Lett.* **8**, D12–D14 (2005). doi:10.1149/1.1870633

9. T. Murakami, T. Nohira, Y. Araki, T. Goto, R. Hagiwara, Y. H. Ogata, Electrolytic synthesis of ammonia from water and nitrogen under atmospheric pressure using a boron-doped diamond electrode. *Electrochem. Solid-State Lett.* **10**, E4–E6 (2007). doi:10.1149/1.2437674

10. N. Serizawa, H. Miyashiro, K. Takei, T. Ikezumi, T. Nishikiori, Y. Ito, Dissolution behavior of ammonia electrosynthesized in molten LiCl–KCl–CsCl system. *J. Electrochem. Soc.* **159**, E87–E91 (2012). doi:10.1149/2.099204jes

11. C. J. Pickett, J. Talarmin, Electrosynthesis of ammonia. *Nature* **317**, 652–653 (1985). doi:10.1038/317652a0

12. N. Furuya, H. Yoshiba, Electroreduction of nitrogen to ammonia on gas diffusion electrodes loaded with inorganic catalysts. *J. Electroanal. Chem.* **291**, 269–272 (1990). doi:10.1016/0022-0728(90)87195-P

13. E. Skúlason, T. Bligaard, S. Gudmundsdóttir, F. Studt, J. Rossmeisl, F. Abild-Pedersen, T. Vegge, H. Jónsson, J. K. Nørskov, A theoretical evaluation of

possible transition metal electro-catalysts for N_2 reduction. *Phys. Chem. Chem. Phys.* **14**, 1235–1245 (2012). Medline doi:10.1039/c1cp22271f

14. I. Amar, R. Lan, C. Petit, S. Tao, Solid-state electrochemical synthesis of ammonia: A review. *J. Solid State Electrochem.* **15**, 1845–1860 (2011). doi:10.1007/s10008-011-1376-x

15. A. Skodra, M. Stoukides, Electrocatalytic synthesis of ammonia from steam and nitrogen at atmospheric pressure. *Solid State Ion.* **180**, 1332–1336 (2009). doi:10.1016/j.ssi.2009.08.001

16. V. Kordali, G. Kyriacou, C. Lambrou, Electrochemical synthesis of ammonia at atmospheric pressure and low temperature in a solid polymer electrolyte cell. *Chem. Commun. (Camb.)* **2000**, 1673–1674 (2000). doi:10.1039/b004885m

17. R. Lan, J. T. S. Irvine, S. Tao, Synthesis of ammonia directly from air and water at ambient temperature and pressure. *Sci. Rep.* **3**, 1145 (2013). Medline doi:10.1038/srep01145

18. R. Lan, S. Tao, Electrochemical synthesis of ammonia directly from air and water using a Li+/H+/NH4+ mixed conducting electrolyte. *RSC Adv.* **3**, 18016–18021 (2013). doi:10.1039/c3ra43432j

19. J. R. McKone, S. C. Marinescu, B. S. Bruneschwig, J. R. Winkler, H. B. Gray, Earth-abundant hydrogen evolution electrocatalysts. *Chem. Sci.* **5**, 865–878 (2014). doi:10.1039/c3sc51711j

20. D. Santos, C. A. C. Sequeira, J. L. Figueiredo, Hydrogen production by alkaline water electrolysis. *Quím. Nova* **8**, 1176–1193 (2013). doi:10.1590/S0100-40422013000800017

21. K. Zeng, D. Zhang, Recent progress in alkaline water electrolysis for hydrogen production and applications. *Progr. Energy Combust. Sci.* **36**, 307–326 (2010). doi:10.1016/j.pecs.2009.11.002

22. J. Ganley, An intermediate-temperature direct ammonia fuel cell with a molten alkaline hydroxide electrolyte. *J. Power Sources* **178**, 44–47 (2008). doi:10.1016/j.jpowsour.2007.11.093

23. J. Ganley, High temperature and pressure alkaline electrolysis. *Int. J. Hydrogen Energy* **34**, 3604–3611 (2009). doi:10.1016/j.ijhydene.2009.02.083

24. S. Licht, L. Halperin, M. Kalina, M. Zidman, N. Halperin, Electrochemical potential tuned solar water splitting. *Chem. Commun. (Camb.)* **2003**, 3006–3007 (2003). Medline doi:10.1039/b309397b

25. M. W. Chase, *J. Phys. Chem. Ref. Data* **9**, 1 (1998).

26. Thermochemical data from (*25*) are available online at U.S. National Institute of Standards and Technology ChemWeb: http://webbook.nist.gov/chemistry/form-ser.html.

27. Glenn Research Center, National Aeronautics and Space Administration (NASA), ThermoBuild access to NASA Glenn thermodynamic CEA database (2006); data available at www.grc.nasa.gov/WWW/CEAWeb/ceaThermoBuild.htm.

28. S. Licht, STEP (solar thermal electrochemical photo) generation of energetic molecules: A solar chemical process to end anthropogenic global warming. *J. Phys. Chem. C* **113**, 16283–16292 (2009). doi:10.1021/jp9044644

29. A. Pelton, K. Hack (and codevelopers), *283 binary salt phase diagram*, [Facility for the Analysis of Chemical Thermodynamics (FACT), Centre for Research in Computational Thermochemistry (CRCT), University of Montreal, rev. ed., 2012]; www.crct.polymtl.ca/FACT/documentation/FTsalt/FTsalt_Figs.htm.

30. Materials and methods are detailed in the supplementary materials on *Science* Online.

31. A. Hellman, E. J. Baerends, M. Biczysko, T. Bligaard, C. H. Christensen, D. C. Clary, S. Dahl, R. van Harrevelt, K. Honkala, H. Jonsson, G. J. Kroes, M. Luppi, U. Manthe, J. K. Nørskov, R. A. Olsen, J. Rossmeisl, E. Skúlason, C. S. Tautermann, A. J. Varandas, J. K. Vincent, Predicting catalysis: Understanding ammonia synthesis from first-principles calculations. *J. Phys. Chem. B* **110**, 17719–17735 (2006). Medline doi:10.1021/jp056982h

32. M. Appl, Ammonia 2 production processes, *Ullman's Encyclopedia of Industrial Chemistry* (Wiley-Verlag, Weinheim, Germany, ed. 7, 2012), pp. 139–210; doi: 10.1002/14356007.

33. S. Licht, Efficient solar-driven synthesis, carbon capture, and desalinization, STEP: Solar thermal electrochemical production of fuels, metals, bleach. *Adv. Mater.* **47**, 5592–5612 (2011). Medline doi:10.1002/adma.201103198

34. R. Pitz-Paal, in *Solar Energy Conversion and Photoenergy Systems*, J. B. Galvez, S. M. Rodriguez, Eds. (EOLSS Publishers, Oxford, 2007).

35. T. Hahm, H. Schmidt-Traub, B. Leßmann, A cone concentrator for high-temperature solar cavity-receivers. *Sol. Energy* **65**, 33–41 (1999). doi:10.1016/S0038-092X(98)00119-4

36. W. Ziqing, Z. Kiuming, L. Jianxin, W. Rong, W. Kemei, Preparation and application of nanometer materials supported ruthenium catalysts. *J. Catal.* **33**, 377–378 (2013).

Vol. 5 • No. 7 • April 8 • 2015

www.advenergymat.de

ADVANCED ENERGY MATERIALS

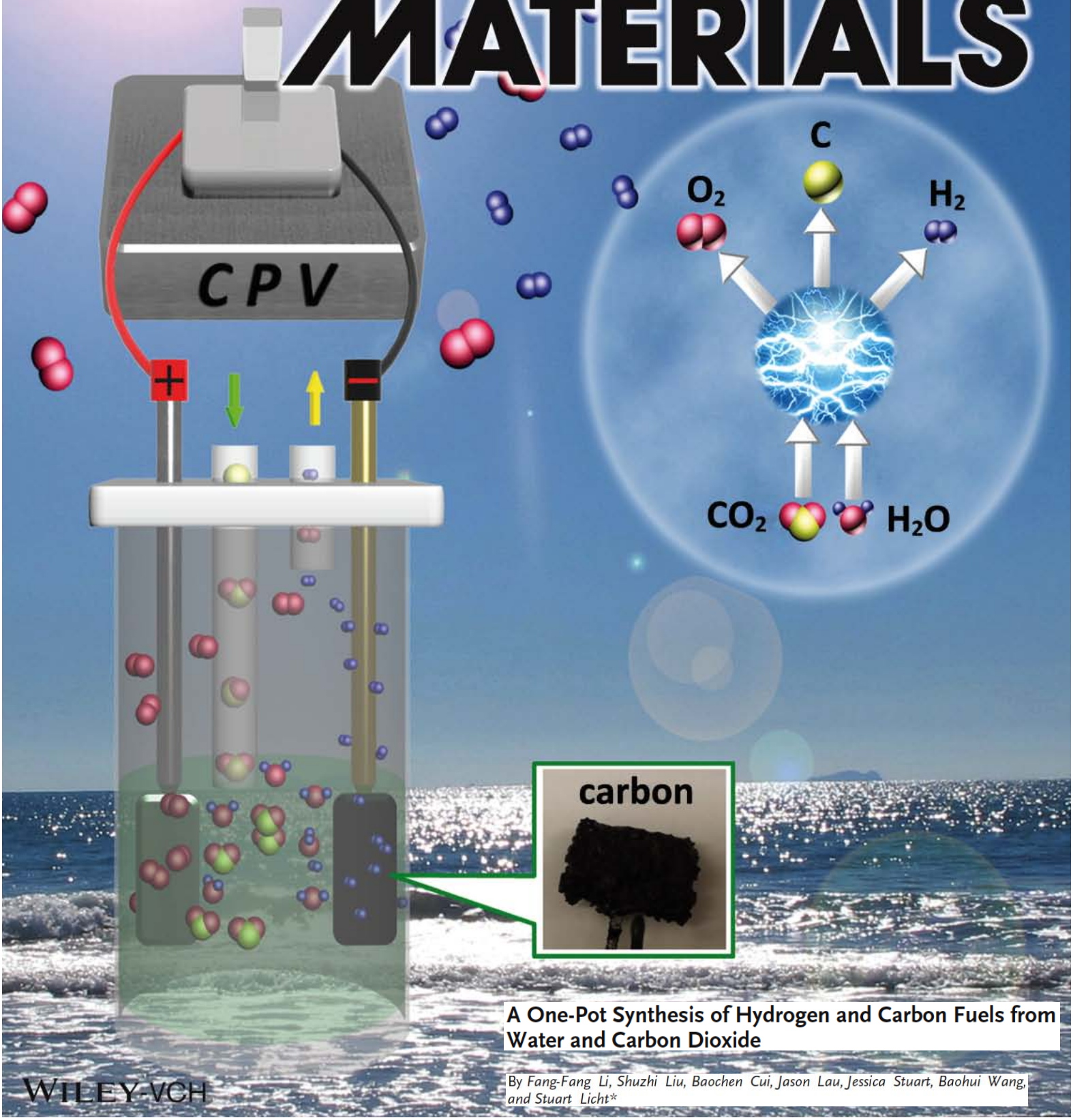

A One-Pot Synthesis of Hydrogen and Carbon Fuels from Water and Carbon Dioxide

By *Fang-Fang Li, Shuzhi Liu, Baochen Cui, Jason Lau, Jessica Stuart, Baohui Wang, and Stuart Licht**

WILEY-VCH

A One-Pot Synthesis of Hydrogen and Carbon Fuels from Water and Carbon Dioxide

*Fang-Fang Li, Shuzhi Liu, Baochen Cui, Jason Lau, Jessica Stuart, Baohui Wang, and Stuart Licht**

Nonfossil fuel-based, low carbon footprint fuels are needed to ameliorate the effects of anthropogenic climate change. In 2002, we presented a solar electrochemical theory that the full spectrum of sunlight was sufficient to split water to hydrogen fuel at over 50% solar conversion efficiency.[1,2] The water splitting electrolysis is endothermic, requiring a smaller potential at higher temperature. The rest potential of common electrolyses, such as $E(H_2O \rightarrow H_2 + 1/2O_2) = 1.23$ V, is often considerably greater than the photopotential of visible light semiconductors. Thermal sunlight can provide an efficient heat source to lower the electrolysis potential, opening a pathway to these otherwise potential-forbidden pathways of charge transfer. We demonstrated this theory in 2003 showing that even a small bandgap semiconductor, such as silicon, was energetically sufficient to split water when sub-bandgap sunlight, not used by the semiconductor, was directed to heating the water.[3] In 2009, this theory was renamed STEP (the solar thermal electrochemical process) and generalized to all endothermic reactions.[4] From 2010 this has been demonstrated for the direct removal of atmospheric carbon dioxide (STEP carbon),[5–7] water treatment[8,9] and organics,[10] and the CO_2-free production of iron (STEP iron),[6,11,12] magnesium and bleach,[6] calcium oxide (STEP cement),[13] and ammonia (STEP fertilizer).[14]

The general use of solar thermal energy to lower the potential of useful electrolyses can be applied to liquid, gas, or solid phase electrolyte cells. In general, we have found an energy advantage in applying STEP to liquid, molten electrolyte cells. Such cells can be driven by thermal sunlight to high temperature accommodating both facile kinetics at high current density and a lower endothermic electrolysis potential. Importantly, molten salt cells can often accommodate high reactant concentrations, which lead to a further decrease in the electrolysis potential (as driven by the Nernst equation). For example, a molten carbonate containing dissolved oxide readily absorbs atmospheric CO_2, and has the advantage that the reducible tetravalent carbon concentration (as carbonate) is 10^6-fold higher than that in air (as CO_2).[4,5] We have previously demonstrated molten hydroxide electrolytes for solar water splitting to hydrogen fuel,[3,6,15] and molten carbonate electrolytes for solar carbon dioxide splitting to carbon and carbon monoxide fuels.[5–7] Lubomirsky and co-workers[16] have also probed the electrolysis of lithium molten carbonates to produce carbon monoxide, and Chen and co-workers[17] have also probed electrolysis of mixed lithium, potassium molten carbonates to carbon.

We have previously delineated the solar, optical, and electronic components of STEP.[6,13] In this study, we focus on the electrolysis component for STEP fuel. Specifically, we present the first molten electrolyte sustaining electrolytic co-production of both hydrogen and carbon products in a single cell. Solid carbon (as coal) is used as the starting point to generate CO and hydrogen for the Fischer–Tropsch generation of a variety of fuels, such as synthetic diesel.[18] However, that process is carbon dioxide emitting intensive. Here, hydrogen and graphitic carbon are produced without carbon dioxide emissions and instead produced from water and carbon dioxide.

This communication recounts our successful attempt to simultaneously co-generate hydrogen and solid carbon fuels from a mixed hydroxide/carbonate electrolyte in a "single-pot" electrolytic synthesis at temperatures below 650 °C. The alternative co-generated hydrogen and gaseous carbon monoxide fuel synthesis will be pursued in a later study as the high temperature (over 900 °C) currently required to form CO in molten carbonates is a challenge to make compatible with the lower temperature range we have succeeded for hydrogen in the hydroxide electrolyses. We demonstrate here the functionality of new lithium–barium–calcium hydroxide carbonate electrolytes to co-generate hydrogen and carbon fuel in a single electrolysis chamber at high current densities of several hundreds of mA/cm^2, at low electrolysis potentials, and from water and CO_2 starting points, which provides a significant step towards the development of renewable fuels.

Molten hydroxides are important as conductive, high-current, low-electrolysis-potential electrolytes for water splitting to generate hydrogen that have not been widely explored.[3,6,19,20] The pure anhydrous akali hydroxides melt only at temperatures >300 °C: LiOH (T_{mp} = 462 °C), NaOH (T_{mp} = 318 °C), KOH (T_{mp} = 406 °C), CsOH (T_{mp} = 339 °C). The mixed hydroxides have lower melting point. With molar ratios of 0.3:0.7 LiOH/NaOH, 0.3:0.7 LiOH/KOH, 0.5:0.5 NaOH/KOH, 0.44:0.56 KOH/CsOH, respectively, these melt at 215 °C, 225 °C, 170 °C, and 195°C, and the melting point is even lower when hydrated hydroxide salts are used. A eutectic 0.45:0.55 mix of LiOH/$Ba(OH)_2$ melts at 320 °C, compared to 407 °C for anhydrous $Ba(OH)_2$, and 300 °C for the monohydrate $Ba(OH)_2 \cdot H_2O$.[21]

Low temperature enhances electrolytic H_2 formation in molten hydroxides. The coulombic efficiency of electrolytic water splitting, η_{H2} (moles H_2 generated per 2 Faraday of applied charge),

Dr. F.-F. Li, Prof. S. Liu, Prof. B. Cui, J. Lau, J. Stuart, Prof. B. Wang, Prof. S. Licht
Department of Chemistry
George Washington University
Washington, DC 20052, USA
E-mail: slicht@gwu.edu

DOI: 10.1002/aenm.201401791

approaches 100% in low melting point, mixed alkali molten hydroxides at temperatures up to 300 °C.

$$H_2O \rightarrow H_2 + 1/2O_2 \quad (1)$$

$$\text{cathode}: 2H_2O + 2e^- \rightarrow H_2 + 2OH^- \quad (2)$$

$$\text{anode}: 2OH^- \rightarrow 1/2O_2 + H_2O + 2e^- \quad (3)$$

Hydroxide hydrates, $MOH{\cdot}nH_2O$ (M = alkali), bind fewer waters, n, at higher temperature, equilibria, and saturated aqueous alkali hydroxide solutions contain less water. For example, saturated NaOH solution equilibrate with 23%, 16%, or 3% water respectively at 100 °C, 200 °C, or 300 °C (saturated aqueous NaOH solution does not boil at 1 atmosphere of pressure[3], As temperature increases, molten alkali hydroxides provide a decreasing source of water for hydrogen generation as they lose water favoring the formation of the oxide:

$$2MOH \rightarrow M_2O + H_2O(\text{gas}) \quad (4)$$

For example, as temperature increases by 100 °C increments from 500 °C to 900 °C, the equilibria constant for the LiOH reaction of Equation 5 (M = Li) increases from 0.006, 0.02, 0.1, 0.3, to 0.8.[22] At higher temperature, the coulombic efficiency of hydrogen generation in molten hydroxide falls as superoxide, O_2^- reduction, increasingly competes with hydrogen formation in the (parasitic) side reactions:[19]

$$\text{anode}: 4OH^- \rightarrow O_2^- + 2H_2O + 3e^- \quad (5)$$

$$\text{cathode}: O_2^- + 2H_2O + 3e^- \rightarrow 4OH^- \quad (6)$$

In **Table 1**, we demonstrate that the efficiency of electrolytic hydrogen formation in pure or mixed molten hydroxide electrolytes is enhanced at lower temperature. We measure the coulombic efficiency of hydrogen formation from water splitting in various molten, pure or mixed alkali or alkali earth hydroxide electrolytes at temperatures from 200 °C up to 800 °C. As seen in the table, the coulombic efficiency falls to η_{H2} = 0% with temperature at 800 °C. At high temperature, we observe higher coulombic efficiency in lithium and barium hydroxide electrolytes than in sodium or potassium hydroxide electrolytes.

High temperature enhances electrolytic carbon fuel formation in molten carbonates. High temperature is advantageous as it decreases the energy necessary to drive the STEP endothermic process. The carbonates, Li_2CO_3, Na_2CO_3, and K_2CO_3, have respective melting points of 723 °C, 851 °C, and 891 °C. Molten Li_2CO_3 not only requires lower thermodynamic electrolysis energy,[5] but in addition has higher conductivity (6 S cm^{-1}) than that of Na_2CO_3 (3 S cm^{-1}) or K_2CO_3 (2 S cm^{-1}) near the melting point.[23] Higher conductivity is desired as it leads to lower electrolysis ohmic losses. Mass transport is also more facile at higher temperature; the conductivity increases from 0.9 to 2.1 S cm^{-1} with temperature increase from 650 °C to 875 °C for a 1:1:1 by mass mixture of the three alkali carbonates.[24]

We observed experimental carbonate electrolysis with two distinct products in two distinct temperature domains. In both cases, current densities >1 A cm^{-2} are sustained with low polarization at nickel anodes and steel cathodes.[5–7,25,26] At temperatures below 800 °C, the only observed cathode product is solid carbon, formed by an efficient $4e^-$ reduction of carbonate (or CO_2 dissolved in carbonate). XRD analysis identifies the carbon product as graphite. From 800 °C to 900 °C, the product transitions from carbon to carbon monoxide. The $2e^-$ reduction of carbonate to carbon monoxide is the only product observed at temperature ≥975 °C in molten lithium carbonate. At 750 °C carbon formation occurs at electrolysis voltage ≥1.08 V, and at 950 °C carbon monoxide formation occurs at ≥0.73 V. At 750 °C carbon formation is sustained at 0.1 A cm^{-2} at electrolysis voltage of 1.5 V, and at 950 °C carbon monoxide sustained at 0.1 A cm^{-2} at 1.0 V. The CO product fraction increases as T approaches 950 °C.

$$Li_2CO_3(\text{molten}) \rightarrow C(\text{solid}) + Li_2O(\text{dissolved}) + O_2(\text{gas}) \quad (7)$$

Table 1. The measured coulombic efficiency of hydrogen generation, η_{H2}, in various molten hydroxide electrolytes at various temperatures. Water (as steam) is bubbled through the electrolyte. Electrolytic water splitting is measured at 267 mA cm^{-2} (1 A) between two planar 3.75 cm^2 nickel electrodes. Efficiency is determined by comparing the measured mole equivalents of hydrogen generated to each 2 mole equivalents (coulombs) of applied current in accord with $H_2O \rightarrow H_2 + 1/2O_2$.

Electrolyte	Melting point	η_{H2} (200 °C)	η_{H2} (300 °C)	η_{H2} (400 °C)	η_{H2} (500 °C)	η_{H2} (600 °C)	η_{H2} (700 °C)	η_{H2} (800 °C)
LiOH	462 °C				88%	21%	4%	0%
$Li_{0.3}Na_{0.7}OH$	215 °C		99%	87%	47%			
NaOH	318 °C			72%				
$Na_{0.5}K_{0.5}OH$	170 °C	96%	86%	47%	28%	13.4%		
KOH	406 °C			80%				
$Li_{0.3}K_{0.7}OH$	225 °C		94%	56%	32%	7.8%		
$Ba(OH)_2$	407 °C				55%	32%		
$Li_{0.33}Ba_{0.67}(OH)_2$			96%					
$(NaOH)_{0.865}(Na_2CO_3)_{0.125}$				77%				
$(LiOH)_{0.843}(Li_2CO_3)_{0.157}$					79%	17.2%	5.5%	

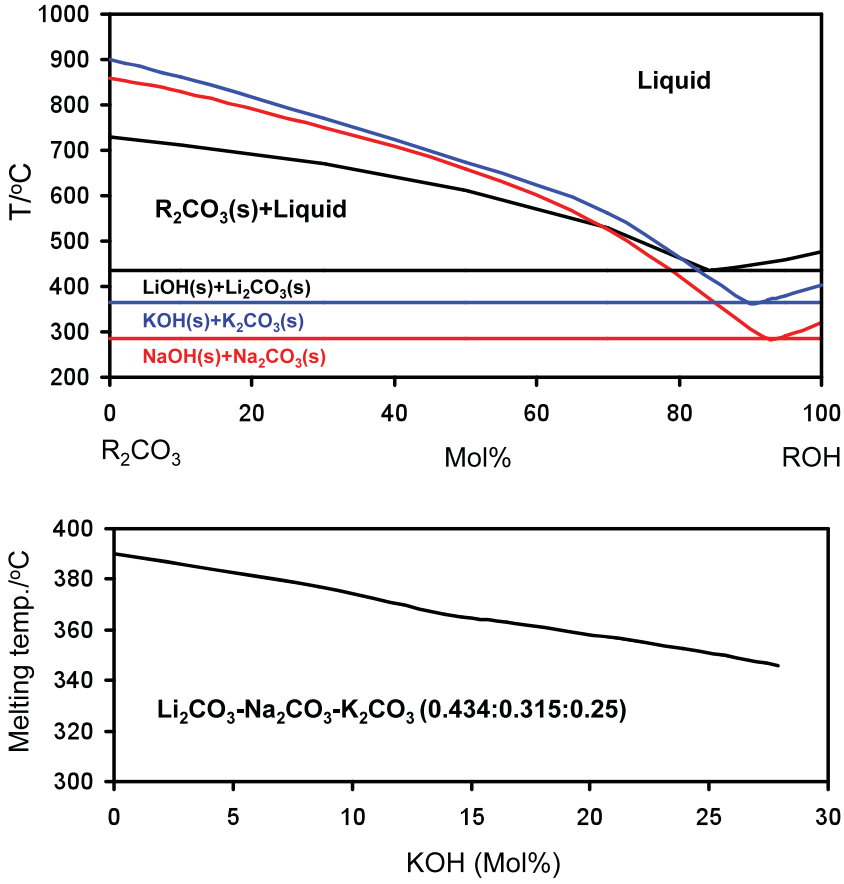

Figure 1. Carbonate–hydroxide binary phase diagrams in pure Li, Na, or K systems (top, using data from ref. [29]) or in a mixed Li, Na, K carbonate with KOH (bottom, using data from ref. [27]). The liquidus areas (above the curves) provide a low temperature molten domain for STEP water and carbon dioxide splitting. The low temperature ensures sufficient hydration within the molten hydroxide component for hydrogen generation, and the simultaneous presence of carbonate in the molten mix provides the opportunity of the co-generation of carbon fuels.

$$Li_2CO_3(\text{molten}) \rightarrow CO(\text{gas}) + Li_2O(\text{dissolved}) + 1/2O_2(\text{gas}) \quad (8)$$

When CO_2 is bubbled in, a rapid complete reaction back to the original lithium carbonate occurs:

$$Li_2O(\text{dissolved}) + CO_2(\text{gas}) \rightarrow Li_2CO_3(\text{molten}) \quad (9)$$

In the presence of carbon dioxide and dissolved Li_2O, reaction 9 is exothermic, and the rapid reaction back to the original lithium carbonate occurs while CO_2 is bubbled into the molten lithium carbonate electrolyte.

The carbon capture reaction in molten carbonate combines Equations (7)–(9):

$$CO_2(\text{gas}) \rightarrow C(\text{solid}) + O_2(\text{gas}); \quad T < 850\ ^\circ C \quad (10)$$

$$CO_2(\text{gas}) \rightarrow CO(\text{gas}) + 1/2O_2(\text{gas}); \quad T > 850\ ^\circ C \quad (11)$$

Low carbonate melting points are achieved by a eutectic mix of alkali carbonates (T_{mp} Li_2CO_3: 723 °C, Na_2CO_3: 851 °C, K_2CO_3: 891 °C; $Li_{1.07}Na_{0.93}CO_3$: 499 °C; $Li_{0.85}Na_{0.61}K_{0.54}CO_3$: 393 °C). We have investigated carbon dioxide and iron oxide splitting electrolyses in mixed Li–Na–K, Cs–Li–Na–K, and Ba–Li carbonate electrolytes, with and without added lithium oxide, Li_2O.[6,7,12,25,26] Lithium oxide (and iron oxide) is highly soluble in both pure lithium carbonate and the alkali carbonate eutectic, and we observe that dissolved Li_2O decreases the carbonate electrolysis potential.[6,12] The concentration of lithium oxide can be controlled to maintain the carbonate electrolyte in the CO_2 absorption mode and eliminate electrolyte carbonate decomposition (the backreaction of Equation (9).

Molten hydroxide/carbonate mix electrolytes to co-generate hydrogen and carbon fuels. The eutectic carbonates/hydroxides had not been considered for electrolyses, but are solar thermal storage molten salt candidates.[27] These electrolytes melt at 346 °C to 420 °C, and facilitate dissolution of both water and carbon dioxide. We are studying these as STEP electrolytes and their phase diagrams are presented in **Figure 1**. In accord with the figure, high molal fractions of the pure hydroxide salt are necessary to achieve low melting points. For example, the eutectic lithium mix studied had 84.3:15.7 mol% LiOH:Li_2CO_3 with a melting point of 434 °C, and the 87.5:12.5 mol% NaOH:Na_2CO_3 sodium mix studied had a melting point of 330 °C. Constant current electrolysis in these electrolytes was studied between 3.75 cm^2 nickel anodes and cathodes over a wide range of currents. Electrolysis was measured at 500, 600, and 700 °C in the lithium hydroxide/carbonate electrolyte and at 400 °C in the sodium hydroxide/carbonate electrolyte. H_2 and O_2 were efficiently generated at the respective nickel anode and cathodes (Table 1). However, consistent with the low carbonate compared to hydroxide concentration in these molten salts, no carbon product was observed to be generated during electrolysis in these single cation electrolytes as studied over a wide range of currents (from mA to A) in either the M = Na electrolyte at 400 °C or the M = Li electrolyte at 500 °C, 600 °C, or 700 °C. At relatively high current densities (0.5 A through 3.75 cm^2 planar electrodes), the electrolysis potential averaged respectively at 700 °C, 600 °C, and 500 °C 1.42, 1.52, and 1.66 V in the mixed lithium hydroxide/carbonate electrolyte, and 1.32, 1.49, and 1.63 V in the pure LiOH electrolyte. Finally, a comparison of three different single alkali cation electrolytes MOH:M_2CO_3, for M = either Li, Na, or K, was compared under similar electrolysis conditions. Each electrolysis was conducted at 500 °C and 1 A, and in electrolytes containing 15 mol% M_2CO_3 and 85 mol% MOH. The electrolyses occurred at average potentials of 2.13 (M = Li), 2.31 (M = Na), and 1.57 V (for M = K). In the Li and Na electrolyses, both cathode and anode were clean (after washing off solidified electrolyte) after the electrolysis (**Figure 2**, top left). However, during the M = K electrolysis, a grey deposit

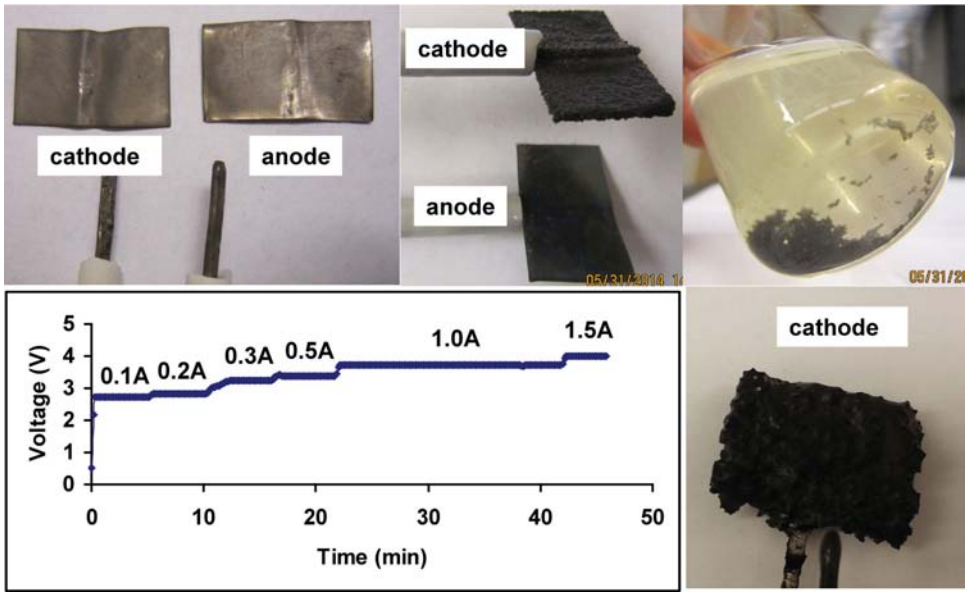

Figure 2. Top left: 3.75 cm^2 (1.5 cm × 2.5 cm) Ni anode and cathode are unaffected by a 1 A electrolysis for 4 h at 500 °C in 85 mol% LiOH with 15 mol% Li_2CO_3. Top middle: the cathode exhibits a deposit subsequent to the 4Ah electrolysis at 500 °C in 85 mol% KOH with 15 mol% K_2CO. Top right: the product removed by sonication of the cathode in water. Bottom: 3.75 cm^2 Ni cathode subsequent to a 470 °C electrolysis in $Li_{0.87}Na_{0.63}K_{0.5}CO_3$ with 9.7 mol% LiOH. Left: constant current electrolysis voltage. Right: graphite product on cathode.

formed on the cathode (Figure 2, top middle), which was analyzed by EDS electron dispersive spectroscopy as nickel and no carbon. This deposit is consistent with the higher corrosivity towards nickel we previously observed for potassium compared to lithium carbonate electrolytes, and the potential of this electrolysis. We previously observed that sodium carbonate corrosivity to anodically biased nickel metal was intermediate to that observed between the corrosive potassium carbonate and the stabilizing lithium carbonate electrolyte.[28]

From 400 °C to 700 °C, and over a wide range of current densities, electrolytes containing carbonate as a minor component and with hydroxide as the major component support facile water splitting forming H_2 as the only fuel product. Unexpectedly, an electrolyte containing carbonate as the major component, which is a eutectic carbonate mixed with hydroxide as the minor component, supports simultaneous splitting of both H_2O (to H_2) and CO_2 (to graphite), providing a one-pot simultaneous synthesis of H_2 and C. Low temperature and high carbonate relative to hydroxide composition were maintained by using the Li, Na, K mixed electrolyte ($Li_{0.87}Na_{0.63}K_{0.5}CO_3$), but with LiOH (rather than KOH used for the phase diagram on the right side of Figure 1) as the hydroxide component. LiOH compared to KOH provides higher conductivity and partially compensates for the K_2CO_3 in the electrolyte to stabilize the nickel anode. The cathode has no deposit subsequent to a electrolysis in a 51.1 mol% LiOH electrolyte, and the cathode exhibits little deposition evident on the cathode after a 31.7 mol% LiOH electrolyte electrolysis, while an 18.0 mol% LiOH electrolyte exhibits a significant, contiguous deposit over the surface of the cathode. Finally, electrolysis in a 9.7 mol% LiOH eutectic alkali carbonate electrolyte results in a 5-fold increase in the cathode product compared (by mass after wash and dry of the product) to the 18.0 mol% LiOH electrolyte. An electrolysis example is presented in Figure 2 at 470 °C; a mix of the eutectic Li, Na, K carbonate with 9.7 mol% LiOH forms products of graphite and hydrogen. The synthesis has high coulombic efficiency (≈25% of the current forms H_2 and ≈40% to carbon production). As seen in Figure 2, the voltage is in the 2.7–3.7 V domain, which is significantly higher than that observed for hydrogen production (water splitting) alone. However, EDS indicates that in addition to the carbon product there is a nickel product at the cathode, and evidence of anode corrosion persists. This anode corrosion is exacerbated in the $Li_{0.87}Na_{0.63}K_{0.5}CO_3$ electrolyte when the 9.7 mol% lithium hydroxide is replaced by 7.4 mol% Li_2O. In the latter case, the anode is at least 60% etched away during the electrolysis, as evident when the electrode is extracted subsequent to the electrolysis.

In order to understand and alleviate the persistent corrosion of the anode, which is not evident during electrolytic splitting to anodic O_2 and cathodic C in a pure lithium carbonate electrolyte, three changes were probed. First, the 3.75 cm^2 shim (thin planar) Ni anodes and cathodes were replaced by more robust 10 cm^2 wound wire planar disc electrodes consisting of pure nickel wire (McMaster 200) for the anode and stainless steel (McMaster 316) for the cathode (**Figure 3**). Replacement of the nickel cathode by steel had little (no) significant effect on the electrolysis, but allowed for greater discrimination of any nickel deposited on the cathode. The electrode pairs prior or subsequent to a corrosive electrolysis are presented in Figure 3. Second, to compensate for corrosion of the anode in the alkali eutectic carbonate/hydroxide mixes, we investigated replacing the LiOH component, with a more stabilizing $Ba(OH)_2$. Figure 3a presents 10 cm^2 coiled wire electrodes prior the electrolysis with both the (316 steel) cathode (situated under the anode) and the Ni anode, and as situated prior to immersion in the electrolysis cell. Figure 3b shows the cathode and anode subsequent

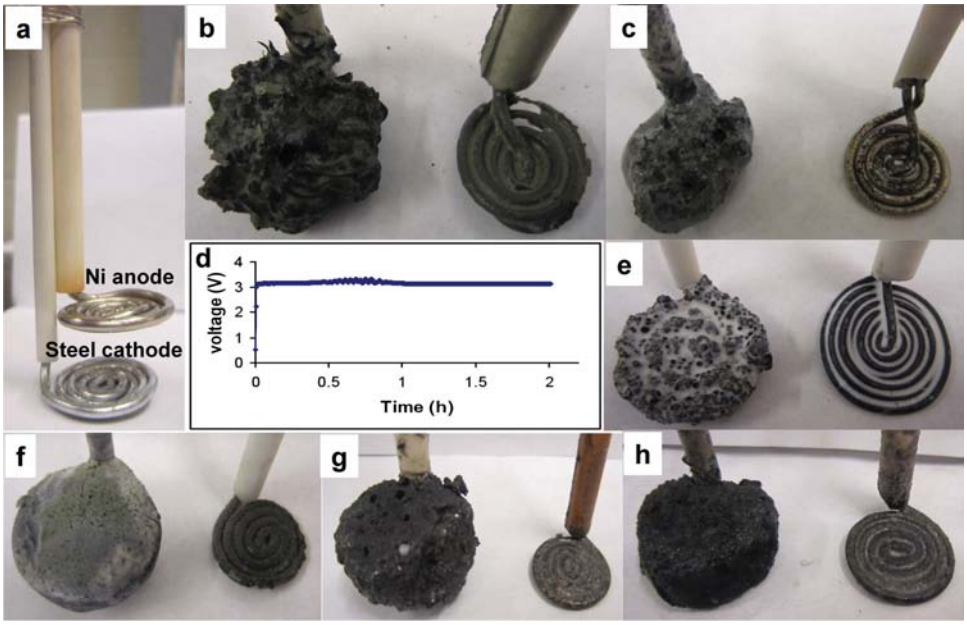

Figure 3. a) 10 cm^2 coiled wire electrodes prior the electrolysis. b,c and g,h) The cathode and anode subsequent to a 1A 2h electrolysis at 480 °C, such as (b) in $Li_{0.87}Na_{0.63}K_{0.5}CO_3$ with 9.7 mol% LiOH which occurred at an average 3.4 V electrolysis potential. While a significant carbon deposition is evident at the cathode, the anode (always shown on the right side of the photon) has been visibly corroded by the electrolysis. c) The anode improvement by replacing LiOH with $Ba(OH)_2$ in the electrolyte. The cathode and anode are shown subsequent to electrolysis in $Li_{0.87}Na_{0.63}K_{0.5}CO_3$ with 11.5 mol% $Ba(OH)_2$, which occurred at an average 3.6 V electrolysis potential. e) Subsequent to electrolysis in the same $Ba(OH)_2$ alkali eutectic carbonate electrolyte, but with two changes: the electrodes are larger (20 cm^2 coiled wire) and CO_2 was bubbled into the electrolyte to ensure rapid replacement of the CO_2 consumed during the electrolysis. At this lower current density, as shown in Figure 3d, the electrolysis occurred at an average potential of 3.14 V. The lowest images show the cathode and anode removed subsequent to 1A 2h electrolysis in the following carbonates LiNaBa (f) or LiNaCa (g), both at 550 °C to ensure melting, or LiCsCa (h), but at 520 °C to ensure melting. LiNaBa = $Li_{0.75}Na_{0.7}Ba_{0.27}CO_3$; LiNaCa = $Li_{0.75}Na_{0.7}Ca_{0.27}CO_3$; LiCsCa = $Li_{0.75}Cs_{0.7}Ca_{0.27}CO_3$.

to a 1A 2h electrolysis at 480 °C in $Li_{0.87}Na_{0.63}K_{0.5}CO_3$ with 9.7 mol% LiOH, which occurred at an average 3.4 V electrolysis potential. While a significant carbon deposition is evident at the cathode, the anode has been visibly corroded by the electrolysis. Figure 3c shows the anode improvement by replacing LiOH with $Ba(OH)_2$ in the electrolyte. The cathode and anode are shown subsequent to a 1A 2h electrolysis at 480 °C in $Li_{0.87}Na_{0.63}K_{0.5}CO_3$ with 11.5 mol% $Ba(OH)_2$, which occurred at an average 3.6 V electrolysis potential. Figure 3e shows the electrodes subsequent to electrolysis in the same $Ba(OH)_2$ alkali eutectic carbonate electrolyte, again at 1A 2h electrolysis at 480 °C, but with two changes: the electrodes are larger (20 cm^2 coiled wire) and CO_2 was bubbled into the electrolyte to ensure rapid replacement of the CO_2 consumed during the electrolysis. At this lower current density, as shown in Figure 3d, the electrolysis occurred at an average potential of 3.14 V.

Third, we investigate replacing the most corrosive potassium carbonate component of the alkali eutectic electrolyte by barium carbonate or calcium carbonate. Figure 3g shows the electrodes subsequent to electrolysis in LiNaBa and LiNaCa carbonates, respectively. A voluptuous carbon deposit is evident at the cathode, but the anode is corroded by the electrolysis according to the EDS analysis of the products. As can be seen in Figure 3,g, the electrolysis containing $BaCO_3$ shows more corrosion than that containing the $CaCO_3$ electrolyte. Therefore, we replaced the $BaCO_3$ with Cs_2CO_3 and use LiCsCa carbonate as the electrolyte. No visible anodic corrosion is evident (as shown in Figure 3h); however, cesium carbonate is an expensive replacement and while not visually evident, EDS continues to show the presence of nickel at the cathode due to corrosion. Finally, we replaced the sodium and potassium carbonates with barium and calcium carbonates, which presented a greater challenge in minimizing the (lithium/barium/calcium, rather than lithium, sodium, potassium) eutectic melting point (in order to maximize the hydrogen evolution current efficiency). After testing the melting point of a range of lithium, barium, and calcium carbonates, a minimum melting point of 620 °C was observed for a $Li_{1.6}Ba_{0.3}Ca_{0.1}CO_3$ electrolyte. Electrolyses were conducted in this electrolyte. Carbon deposition occurred at the cathode as displayed in **Figure 4**. At the lower current density (0.1A 20h) as shown in Figure 4b, the electrolysis occurred at an average potential of 2.0 V over the 10 cm^2 coiled wire disk electrodes. The improvement in the anode stability was marked. There is no evidence of anode corrosion, and the carbon product on the cathode contains no nickel (as measured by EDS). The black/gray overcoat on the anode is a nickel oxide stable overlayer, which we have previously observed to sustain the anode as an effective, stable electrocatalyst facilitating oxygen formation.[11] The one-pot co-synthesis of H_2 and C was carried out in this new $Li_{1.6}Ba_{0.3}Ca_{0.1}CO_3$ electrolyte with LiOH as hydroxide component. An electrolysis is presented in Figure 4c,d at 620 °C; a mix of the eutectic $Li_{1.6}Ba_{0.3}Ca_{0.1}$ carbonate with 18.0 mol% LiOH forms a product of graphite (Figure 4d) and hydrogen which was analyzed by both Micro IV

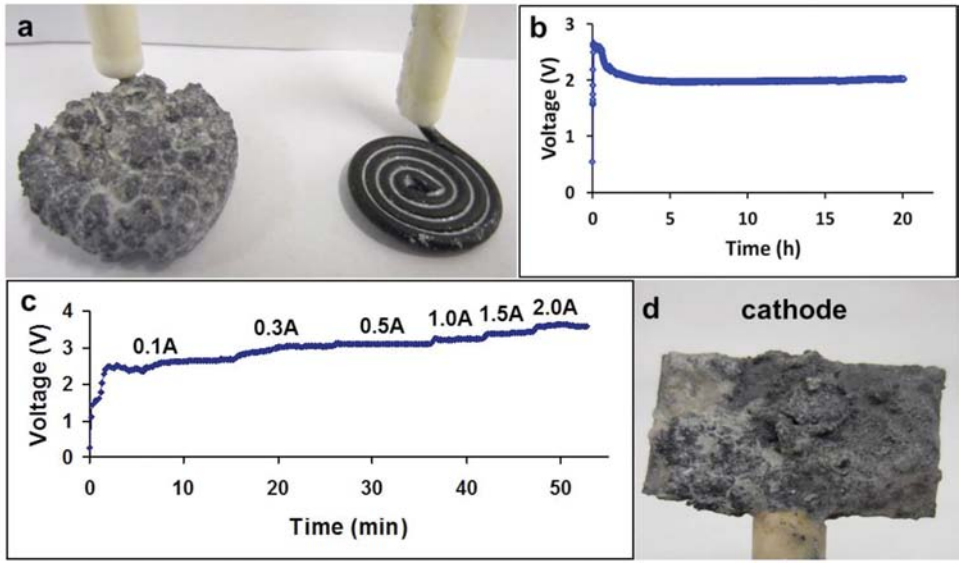

Figure 4. Electrolysis in $Li_{1.6}Ba_{0.3}Ca_{0.1}$ carbonates and 18.3 mol% LiOH electrolyte at 620 °C. a) 10 cm^2 coiled wire cathode and anode after electrolysis at 0.1 A for 20 h with an average potential of 2.0 V (b). c,d) The electrolysis with 3.75 cm^2 planar nickel anode and nickel cathodes. (c) displays the electrolysis voltage at various constant currents and (d) graphite product on the cathode subsequent to the electrolysis.

hydrogen analyzer (GfG Instrumentation) and Gas Chromatograph. The synthesis has high coulombic efficiency with ≈62% of the current generating H_2 and 20% generating carbon at an applied electrolysis current of 2 A through the 3.75 cm^2 planar nickel anode and nickel cathode. The electrolysis sustains the simultaneous, efficient co-generation of hydrogen and carbon in a single electrolysis chamber. It is interesting to note that the H_2 coulombic efficiency in the $LiOH/Li_{1.6}Ba_{0.3}Ca_{0.1}CO_3$ electrolyte is higher than that observed at 500 °C in a pure barium hydroxide electrolyte, and which had not permitted the co-generation of fuels However, the observed current efficiency of H_2 generation is observed to be lower at smaller applied currents: 30% at 1.5 A and 23% at 1 A. As seen in Figure 4c, the voltage is in the 2.5–3.5 V domain (through the flat 3.75 cm^2 electrodes), which is slightly lower than that observed in LiNaK carbonate and 9.7 mol% LiOH but still much higher than that observed for hydrogen production (water splitting) alone.

The demonstrated functionality of the lithium barium calcium carbonate and lithium hydroxide electrolytes to co-generate hydrogen and carbon fuel at high current densities of several hundreds of mA/cm^2, at low electrolysis potentials, and from water and CO_2 starting points, provides a significant step towards the development of renewable fuels. This one-pot molten electrolyte synthesis is compatible with the STEP process,[4–15] in which solar thermal energy increases the system temperature to decrease electrolysis potentials.

Supporting Information

Supporting Information is available from the Wiley Online Library and consists of experimental details and pure hydroxide (without carbonate) electrolysis results.

Acknowledgements

The authors are grateful to the ONR award N14–13–1006568 for support of this study.

Received: October 9, 2014
Revised: November 20, 2014
Published online: December 23, 2014

[1] S. Licht, *Electrochem. Comm.* **2002**, *4*, 789.
[2] S. Licht, *J. Phys. Chem. C* **2003**, *107*, 4253.
[3] S. Licht, L. Halperin, M. Kalina, M. Zidman, N. Halperin, *Chem. Comm.* **2003**, 3006.
[4] S. Licht, *J. Phys. Chem. C* **2009**, *113*, 16283.
[5] S. Licht. B. Wang, S. Ghosh, H. Ayub, D. Jiang, J. Ganley, *J. Phys. Chem. Lett.* **2010**, *1*, 2363.
[6] S. Licht, *Adv. Mater.* **2011**, *23*, 5592.
[7] S. Licht, B. Cui, B. Wang, *J. CO_2 Utilization* **2013**, *2*, 58.
[8] B. Wang, H. Wu, G. Zhang, S. Licht, *ChemSusChem* **2012**, *5*, 2000.
[9] B. Wang, Y. Hu, H. Wu, S. Licht, *Electrochem. Sci. Lett.* **2013**, *2*, H34.
[10] Y. Zhu, B. Wang, X. Liu, H. Wang, H. Wu, S. Licht, *Green Chem.* **2014**.*14*, 476.
[11] S. Licht, H. Wu, *J. Phys. Chem. C* **2011**, *115*, 25138.
[12] B. Cui, S. Licht, *Green Chem.* **2013**, *15*, 881.
[13] S. Licht, H. Wu, C. Hettige, B. Wang, J. Lau, J. Asercion, J. Stuart, *Chem. Comm.* **2012**, *48*, 6019.
[14] S. Licht, B. Cui, B. Wang, F.-F. Li, J. Lau, S. Liu, *Science* **2014**, *345*, 637.
[15] S. Licht, O. Chityat, H. Bergmann, A. Dick, S. Ghosh, H. Ayub, *Int. J. Hyd. Energy* **2010**, *35*, 10867.
[16] V. Kaplan, E. Wachtel, K. Gartsman, Y. Feldman, I. Lubomirsky, *J. Electrochem. Soc.* **2010**, *157*, B552.
[17] H. Ijije, C. Sun, G. Chen, *Carbon* **2014**, *73*, 163.

[18] A. Andrews, J. Logan, Fischer-Tropsch Fuels from Coal, Natural Gas, and Biomass: Background and Policy. *Congressional Research Service Report for Congress* **2008**, RL34133, (March 27, 2008); available at: http://assets.opencrs.com/rpts/RL34133_20080327.pdf; http://www.congressionalresearch.com/RL34133/document. php?study = Fischer-Tropsch+Fuels+from+Coal+Natural+ Gas+and+Biomass+Background+and+Policy.
[19] J. Divisek, J. Mergel, H. F. Nissen, *Int. J. Hyd. Energy* **1980**, *5*, 151.
[20] J. Ganley, *Int. J. Hyd. Energy* **2009**, *4*, 3604.
[21] M. Maurice, A. Erb, G. Ado, *C. R. Acad. Sci. Paris* **1971**, *272*, 842.
[22] L. V. Gurvich, G. A. Bergman, L. N. Gorokhov, *J. Phys. Chem. Ref. Data* **1996**, *25*, 1225.
[23] Z. Zhang, Z. Wang, Z., eds, *Principles and Applications of Molten Salt Electrochemistry*, **2006**, Chemical Industry Press, Beijing, p. 191.
[24] T. Kojima, Y. Miyazaki, K. Nomura, K. Tanimoto, *J. Electrochem. Soc.* **2008**, *155*, F150.
[25] S. Licht, B. Cui, J. Stuart, B. Wang, J. Lau, *Energy Env. Sci.* **2013**, *6*, 3646.
[26] B. Cui, S. Licht, *J. Mat. Chem. A* **2014**, *2*, 10577.
[27] R. I. Olivares, C. Chen, S. Wright, *J. Solar Energy Eng.* **2012**, *134*, 41002.
[28] S. Licht, Stabilization of STEP electrolytes **2012** (accessed: Dec 2014), http://arxiv.org/pdf/1209.3512.pdf.
[29] *FACT Salt Phase Diagrams* (accessed: De. 2104), http://www.crct.polymtl.ca/fact/documentation/FTsalt/FTsalt_Figs.htm

Green Chemistry

RSC Publishing

COMMUNICATION

Critical STEP advances for sustainable iron production†

Cite this: *Green Chem.*, 2013, **15**, 881

Received 14th October 2012,
Accepted 5th February 2013

DOI: 10.1039/c3gc00018d

www.rsc.org/greenchem

Baochen Cui and Stuart Licht*

A transformative, sustainable technology to replace the age-old CO_2-intensive production of iron is presented. Molten calcium inclusive carbonates are introduced for STEP Iron. Understanding the speciation constraints permits iron synthesis at nearly 100% coulombic efficiency, without exotic electrocatalysts, and at low electrolysis energy.

There is an urgent need for a material's synthesis to replace the millennia old CO_2-extensive (carbothermal) iron making process. The production of iron and its alloys are one of the top contributors to greenhouse gases (other major contributors are electrical and vehicular power production and cement), and 9 kg of carbon dioxide are emitted for each 10 kg of iron produced. We presented a STEP (Solar Thermal Electrochemical Process) theory of solar energy conversion, building on an alternative theory of solar water splitting, that solar thermal energy could drive endothermic electrochemical reactions (such as the reduction of carbon dioxide) at high solar energy conversion efficiency in molten electrolytes and without carbon dioxide emission.[1] We experimentally demonstrated that STEP can extract graphite from carbon dioxide at solar efficiencies exceeding that of solar cells. STEP has now been applied to a range of useful products including cement, and towards water desalinization and water treatment.[1–3]

In this communication a new, effective molten path for the electrolytic CO_2-free formation of iron is introduced. The electrochemical reduction of iron ore had been investigated in several electrolytes.[4–9] Each of those electrochemical reductions had physical chemical limitations, such as high energy or corrosivity that, to date, had prevented implementation of an electrochemical replacement to the carbothermal production of iron. Electrolysis of the emitted CO_2 subsequent to iron production has also been considered.[1,10] Recently, we presented a molten Li_2CO_3 electrolytic process (STEP) to generate iron without emitting CO_2 and requiring little energy, in mixed alkali and pure lithium molten carbonates.[1,11] However, a complex, spatially dispersed, electrodeposition occurs near the cathode that includes partially reduced (Fe^{2+}) species. This speciation is mapped for the first time in this study. An alternative, carbonate $Na_xK_yCO_3$ can confine iron to the cathode, but is not "green" corroding anode and cathode and decomposing the carbonate emitting CO_2.[12] Here, this corrosion is eliminated in a new, less alkaline iron splitting electrolyte, in which iron ore is effectively electrolyzed to iron at high efficiency and low energy.

In the prior STEP Iron formation process, an oxide, such as lithium oxide, Li_2O, dissolves the iron oxide, and is regenerated during the electrochemical reduction. Iron oxides were discovered to be unexpectedly, highly soluble in lithiated carbonates.[1] The electrolysis of the iron oxide enriched electrolyte occurs without carbon dioxide release, and without net consumption of the carbonate, such as through the intermediate soluble salt $MFeO_2$:

$$\text{dissolution}: \quad Fe_2O_3 + M_2O \rightarrow 2MFeO_2 \tag{1}$$

$$\text{electrolysis}: \quad 2MFeO_2 \rightarrow 2Fe + M_2O + 3/2O_2 \tag{2}$$

$$\text{net}: \quad Fe_2O_3 \rightarrow 2Fe + 3/2O_2 \tag{3}$$

Broadening the base of understanding of speciation in the STEP Iron process will be critical to replace a pervasive high carbon footprint industrial process with an effective, low energy CO_2-free alternative. In this communication, we provide (i) the first map of the speciation of the diffuse STEP Iron product, (ii) minimize the energy of the eqn (1)–(3) mechanism, and (iii) demonstrate an alternative synthetic route, which does not produce a spatially diffuse product based on dissolution. The alternative pathway maintains the low carbon footprint, but is based on insoluble iron oxides and produces an iron metal product confined to within the interfacial domain of the cathode, and without release of iron oxide to the bulk electrolyte.

Department of Chemistry, George Washington University, Washington, DC 20052, USA. E-mail: slicht@gwu.edu; Fax: +202-994-5873; Tel: +703-226-8225

†Electronic supplementary information (ESI) available: Expanded introduction, methodology details, and electrochemical parameter optimization for the STEP Iron process. See DOI: 10.1039/c3gc00018d

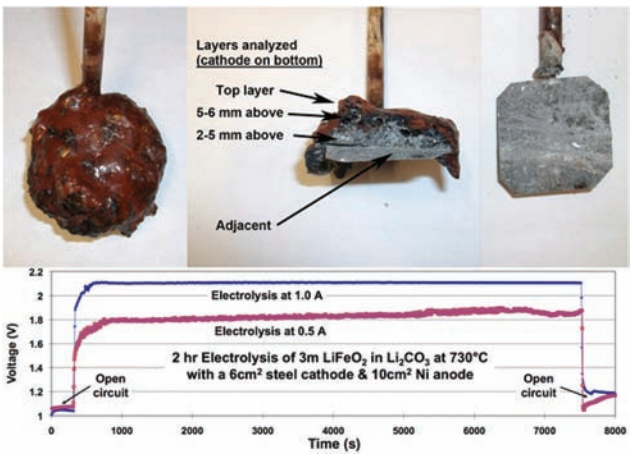

Fig. 1 Middle: Potential during the constant current electrolysis in 730 °C molten Li_2CO_3 containing 3 m $LiFeO_2$. Top: Photographs of cathode and product following STEP Iron electrolysis for 2 hours at a constant current of 1 A. Left: cathode subsequent to electrolysis, extraction and cooling. Middle: bare cathode after removal of the product (the product readily peels off the cooled cathode). This reusable cathode consists of 2.5 cm × 2.5 cm steel. Right: a cut, cross-section view of the product still on the cathode.

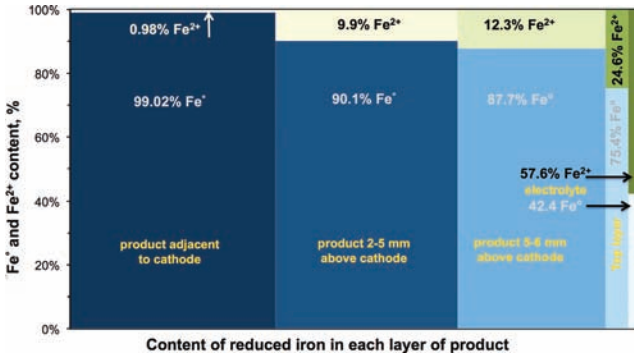

Fig. 2 Cross sectional profile of the reduced iron species analyzed from the layers photographed in Fig. 1, and the electrolyte (right side).

The series of photos in Fig. 1 present a STEP Iron electrolysis product, as deposited from molten lithium carbonate onto a planar steel cathode. A reductive bias protects cathodes during STEP Iron electrolysis, and a wide variety of materials (iron, steel, carbon) are effective as cathodes.[11] The left photo of Fig. 1 presents a cathode subsequent to electrolysis in molten Li_2CO_3 containing dissolved iron oxide, extraction and cooling. The middle photo shows a cut, cross-section view of the product as removed from the cathode. The product readily peels off the cooled cathode, and the right photo shows the reusable, bare cathode after removal of the product.

The ESI† details the iron analyses and electrolysis configuration used.[13–16] To address the issue of the ratio of the different oxidation states of iron in the electrolysis product several techniques were considered. Techniques such as XPS provide these different oxidation states, but apply to only a small portion of the sample. From a material's perspective this high degree of spatial localization was considered here to leave the interpretation subject to too small a sample (the "trees" rather than "forest" perspective). However, such studies will be valuable in the future. Powder X-ray diffraction was also considered, and was performed on several samples. For example the electrolysis product near lying to the cathode exhibited iron metal 2-theta peaks (at 44.6°) and Li_2CO_3 (at 21.3, 29.4, 30.6, 31.8, 34.2 36.1, 36.9, 43.6, 44.7, and 48.8°). However the technique was considered more time consuming, expensive and less direct than classic quantitative analysis methodologies. This latter method directly probes the oxidation state of the iron species, and had the added advantage that it was conducted in-lab. Hence the classic quantitative analysis technique of precipitation analysis was chosen for this study to provide a complete description of the ferrous, ferric and metallic iron oxidation states as detailed in the ESI.†

Fig. 2 profiles the measured concentrations of the reduced iron species subsequent to electrolysis. The width reflects the relative total fraction of iron metal found in each layer. The vertical subdivisions of each bar reflect the relative iron oxide concentration that has been reduced to Fe^{2+} or to iron metal. Product closer to the cathode is on the left side, and product further from the cathode is on the right side of the scheme.

The Fig. 2 compositional analysis provides an understanding of each of the layers evident in the photograph of the cathode product. Consistent with the grey-metal color, the dominant iron species in the layer adjacent to the cathode is zero-valent iron. The additional black evident in the next layers is consistent with the color of partially reduced iron oxides, such as ferrous oxide or Fe_3O_4. The thin, top layer on the product was still molten while the cathode was extracted. The red/brown color of this layer is similar to that of the remaining bulk electrolyte, but still contains a significant (zero valent) iron metal content. Finally furthest from the cathode, the post electrolysis bulk electrolyte also contains zero valent iron (although at a much lower level, less than 1% of that found at the cathode surface), as well as partially reduced (ferrous) iron, and also ferric ion remaining from the initial iron oxide dissolution.

The product speciation profile in Fig. 2 presents the substantial, but incomplete reduction of iron. One objective of this study is the systematic optimization of the STEP Iron to approach 100% coulombic efficiency of the conversion of ferric ion, Fe^{3+}, to iron metal, Fe°, and a second objective to accomplish that high coulombic efficiency at low energy (low applied electrolysis potential and high current density). The electrolysis of Fig. 1, is conducted with parallel, horizontal anode and cathode. The nickel oxygen evolving anode is situated near the surface of electrolyte, 1 cm above the cathode. The 10 cm^2 nickel electrode is oversized compared to the 6.2 cm^2 cathode.

The electrolyte composition and temperature, and the electrode configuration, duration and current density have a substantial impact on STEP Iron coulombic efficiency. For example, the electrolysis of Fig. 1 is conducted at 730 °C, near the electrolyte melting point, and a rise in temperature to 850 °C decreases the requisite electrolysis potential but

generates a lower fraction of iron metal. The ESI† begins with an electrolysis temperature of 800 °C, and systematically conducts modification of the physical chemical components of the system to understand conditions which increase coulombic efficiency and minimize the requisite electrolysis potential.

Following extensive modification and systematic optimization as delineated in the ESI,† optimized, high efficiency, low energy electrolyses are measured with an outer foil or wire cylinder pure nickel anode and a small or large diameter inner steel foil cathode. The *coulombic efficiency* compares the applied electrolysis current to the theoretical required for the three electron reduction of Fe^{3+} to iron metal. Efficiency is highest at minimum molten lithium carbonate temperature, intermediate dissolved ferric concentration (3 molal), intermediate cathode and anode current density, anode electron transfer facilitated by situating the anode near the electrolyte// air interface, and or a vertical cathode parallel to a vertical anode. Extended duration electrolyses can be sustained if levels of ferric are not depleted, such as would be achieved *via* continuous addition of ferric oxide during the electrolysis. The electrolysis configuration is simplified when the electrolysis is conducted in a nickel crucible, which comprises both the anode and the cell body in one piece.

The *overpotential* is constrained by the anode current density; energy minimization is achieved with a maximum anode surface area. Interelectrode separations must be small enough (<1 cm) to minimize potential loss at high (>0.1 A cm^{-2}) current density. Consistent with the expected Nernst decrease of redox potential with increasing ferric concentration, higher $LiFeO_2$ (and Li_2O) concentration decreases the electrolysis potential.

As delineated in the ESI,† optimized electrolyses occur in a low electrolysis potential of 1.35 V and at coulombic efficiency approaching 100%. The energy required to generate a mole of iron is 1.35 V × (3 Faraday/mole Fe) × (26.8 Ah per Faraday) = 109 Wh per mole of iron. This is only approximately 1/3 of the energy required to produce a mole of iron using coke carbon by the conventional carbothermal method (this assumes solar thermal energy is used to maintain the 730 °C STEP Iron electrolysis temperature).

Lithium containing carbonate electrolytes promote soluble iron oxide, as mediated by lithium oxide, eqn (1). The high solubility leads to low energy iron metal electrodeposition, but the iron product can be spatially diffuse. The carbon footprint of molten carbonate electrolytes with less soluble or insoluble is explored here as green, low cost alternatives to a pure lithium carbonate electrolyte. Iron oxide solubility in a molten carbonate electrolyte decreases when there is less lithium present; the solubility of Fe^{3+} in a $Li_{0.87}Na_{0.63}K_{0.5}CO_3$ eutectic is less than half of its value in Li_2CO_3.[1] Electrolysis of Fe^{3+} dissolved in this eutectic diminishes the secondary Fe^{2+} layer in the product, compared to that in Li_2CO_3, as seen in Fig. 7 of the ESI.†

We previously observed that a lithium-free carbonate $Na_{1.23}K_{0.77}CO_3$ eutectic is corrosive towards the nickel anode, the steel cathode, and the electrolyte, impeding CO_2 electrolysis, and in preliminary results (on CO_2 splitting) observed that $CaCO_3$ addition is highly stabilizing, sustaining an effective electrolysis of CO_2 to carbon and oxygen.[2] We attributed the $Na_{1.23}K_{0.77}CO_3$ corrosivity to the observed high solubility and alkalinity of Na_2O, and the effective electrolysis in $Ca_{0.27}Na_{0.7}K_{0.75}CO_3$ to the low solubility and alkalinity of CaO.

Fig. 3 Electrolytic production of iron using solid, rather than dissolved, iron oxide.

Here we observe that Fe^{3+} is insoluble (solubility ≪ 0.1 m Fe_2O_3) in both $Na_{1.23}K_{0.77}CO_3$ and $Ca_{0.27}Na_{0.7}K_{0.75}CO_3$. We investigate electrolysis of solid Fe_2O_3 pressed onto the cathode as shown on the bottom of Fig. 3. Electrolytic reduction of 2 g of solid Fe_2O_3 (pressed at 6000 psi on each side of a coiled 26.5 cm, 1.2 mm diameter, 10 cm^2 iron wire, Fig. 3 bottom), then dry annealed at 750 °C for 2 hours, was compared in three molten carbonate electrolytes: pure lithium, a sodium potassium eutectic and a calcium, sodium, potassium eutectic. The previous STEP Iron process using Fe_2O_3 dissolved as $LiFeO_2$ in Li_2CO_3 is a CO_2-free process.[11,12] However, the electrolytic reduction of Fe_2O_3 in $Na_{1.23}K_{0.77}CO_3$ is not "green". Unlike the Li_2O containing Li_2CO_3 electrolyte, this electrolyte reacts with iron oxide and releases CO_2 in accord with:

$$Fe_2O_3 + M_2CO_3 \rightarrow 2MFeO_2 + CO_2 \quad (4)$$

Eqn (4) is observable both as a mass loss from the electrolyte, rapid bubble evolution from the cathode, and darkening of the electrolyte during the electrolysis.

Electrolysis in the $Ca_{0.27}Na_{0.7}K_{0.75}CO_3$ electrolyte decreases the rate of CO_2 emission from the cathode, and results in a high quality iron metal deposit. The observed, qualitative rate of bubble evolution from the immersed cathode during 750 °C electrolysis decreased in the order Li_2CO_3 (vigorous in the absence of dissolved Li_2O) > $Na_{1.23}K_{0.77}CO_3$ (vigorous) > $Ca_{0.27}Na_{0.7}K_{0.75}CO_3$ (little, if any bubble

evolution). Similarly as shown on the top of Fig. 3, post electrolysis, the molten calcium-containing electrolyte had not changed color, whereas the Li_2CO_3 electrolyte has turned red due to ferric dissolution (as $LiFeO_2$), and the $Na_{1.23}K_{0.77}CO_3$ electrolyte has become black. The electrolyte, which solidifies on extraction of the $Ca_{0.27}Na_{0.7}K_{0.75}CO_3$ electrolysis product, is readily removed by a water wash. The washed metal product seen in Fig. 3, is formed at high coulombic efficiency (98% compared to only 49 or 50% coulombic conversion from Fe_2O_3 in either the Li_2CO_3, or $Na_{1.23}K_{0.77}CO_3$ during the 2 hour 0.5 amp electrolysis). The nickel oxygen anode, photographed on the top right of Fig. 3 is unaffected by this electrolysis in $Ca_{0.27}Na_{0.7}K_{0.75}CO_3$.

Finally, although Ca^{2+} added to the $Na_yK_zCO_3$ electrolyte as calcium carbonate, $CaCO_3$, suppresses corrosion and CO_2 emission from the cathode, it does not prevent CO_2 emission from another source; that is the decomposition of the carbonate electrolyte, which occurs in accord with the equilibrium:

$$M_2CO_3 \rightleftharpoons M_2O + CO_2 \quad (5)$$

This final electrolyte decomposition challenge is overcome by the addition of 0.5 m CaO (lime) rather than $CaCO_3$ (limestone) to the molten carbonate electrolyte, and we observe that both the iron oxide insoluble $CaO/Na_yK_zCO_3$ and CaO/Li_2CO_3 electrolytes, as well as the previous iron oxide soluble Li_2O/Li_2CO_3 electrolyte, provide a high quality iron metal electrolysis product from solid, pressed iron oxide. Added oxide eliminates the carbonate decomposition emission of CO_2 by driving equilibrium 5 to the left. Specifically, we had previously observed that at 750 °C Li_2CO_3 with 3 m Li_2O, absorbs atmospheric CO_2 and gains mass when exposed to air, while without added Li_2O, Li_2CO_3 or $CaCO_3/Li_2CO_3$ both emit CO_2 and lose mass (these effects are quantified and elaborated upon in ref. 2 ESI†).

In summary, the chemistry of a transformative process to decrease greenhouse gas emissions is developed here. High quality, low energy iron metal products are produced by the green electrolysis of iron oxide in molten carbonates and provide an important opportunity to replace the CO_2 intensive-carbothermal production of iron. A calcium-containing electrolyte, $CaO/Na_yK_zCO_3$, is more effective for iron production than $Na_yK_zCO_3$ from several perspectives, maximizing iron conversion efficiency, minimizing nickel anode corrosion, minimizing dissolution into the electrolyte, and spatially constraining the iron product to the cathode surface. The energy required to produce STEP Iron is only approximately 1/3 of the energy required to produce a mole of iron using coke carbon by the conventional carbothermal method (this assumes solar thermal energy is used to maintain the 730 °C STEP Iron electrolysis temperature). Future studies will probe replacing calcium with barium, which presumably will have similar, less alkaline, advantageous effects on the iron product, and electrolyte and anode stability.

Acknowledgements

We gratefully acknowledge partial support of this research by the US NSF.

Notes and references

1 S. Licht, *Adv. Mater.*, 2011, **47**, 5592.
2 S. Licht, H. Wu, C. Hettige, B. Wang, J. Lau, J. Asercion and J. Stuart, *Chem. Commun.*, 2012, **48**, 6019; S. Licht, H. Wu, C. Hettige, B. Wang, J. Lau, J. Asercion and J. Stuart, *Chem. Commun.*, 2011, **47**, 3081; S. Licht, H. Wu, C. Hettige, B. Wang, J. Lau, J. Asercion and J. Stuart, *Chem. Commun.*, 2010, **46**, 7004; S. Licht, H. Wu, C. Hettige, B. Wang, J. Lau, J. Asercion and J. Stuart, *Chem. Commun.*, 2005, 4623; S. Licht, H. Wu, C. Hettige, B. Wang, J. Lau, J. Asercion and J. Stuart, *Chem. Commun.*, 2003, 3006; and as related to batteries: S. Licht, H. Wu, C. Hettige, B. Wang, J. Lau, J. Asercion and J. Stuart, *Chem. Commun.*, 2008, 3257; S. Licht, H. Wu, C. Hettige, B. Wang, J. Lau, J. Asercion and J. Stuart, *Chem. Commun.*, 2007, 2753; S. Licht, H. Wu, C. Hettige, B. Wang, J. Lau, J. Asercion and J. Stuart, *Chem. Commun.*, 2006, 4341.
3 S. Licht, *J. Phys. Chem. C*, 2009, **35**, 16283; S. Licht, B. Wang and H. Wu, *J. Phys. Chem. C*, 2011, **115**, 11803; S. Licht, *et al.*, *J. Phys. Chem. Lett.*, 2010, **1**, 2363; S. Licht, *et al.*, *Int. J. Hydrogen Energy.*, 2010, **35**, 10867; B. Wang, H. Wu, G. Zhang and S. Licht, *ChemSusChem*, 2012, **5**, 2000. The studies date back to the original STEP-like theory on water splitting at: S. Licht, *J. Phys. Chem. B*, 2003, **107**, 4253; S. Licht, *Electrochem. Commun.*, 2002, **4**, 789.
4 B. He, R. V. Gudavarthy, J. A. Koza and J. A. Switzer, *J. Am. Chem. Soc.*, 2011, **133**, 12358.
5 C. Donath, E. Neacsu and N. Ene, *Rev. Roum. Chim.*, 2011, **56**, 763.
6 A. Pal, A. N. Samata and S. Ray, *Hydrometallurgy*, 2010, **105**, 30.
7 B. Y. Yuan, O. E. Kongstein, G. M. Haarberg, A. N. Samata and S. Ray, *J. Electrochem. Soc.*, 2009, **156**, D64.
8 A. Allanore, H. Lavelaine, J. P. Birat, G. Velentin and F. Lapicue, *J. Appl. Electrochem.*, 2010, **40**, 2010.
9 E. Mostad, S. Rolseth and J. Thonstad, *Hydrometallurgy*, 2008, **90**, 213.
10 A. L. Dipu, J. Ryu and Y. Kato, *ISIJ Int.*, 2012, **52**, 1427.
11 S. Licht and H. Wu, *J. Phys. Chem. C*, 2011, **115**, 25138.
12 S. Licht, *arXiv* [physics.chem-ph], 2012, *arXiv*: **1209.3512**, 1.
13 Z. Xu, H. Hwant, R. Greenlund, X. Huang, J. Luo and S. Anshuetz, *J. Miner. Mater. Character. Eng.*, 2003, **2**, 65.
14 X. Shi, J. Liao and S. Wang, *Rock Miner. Anal.*, 2009, **28**, 197.
15 ASTM designation: D3872-86. Standard Test Method for Ferrous Iron in Iron Oxides. *Annual Book of ASTM Standards*, 1999, 1.
16 Y. Gende and O. Lahav, *Appl. Geochem.*, 2008, **23**, 2123.

ChemComm

Dynamic Article Links

Cite this: *Chem. Commun.*, 2012, **48**, 6019–6021

www.rsc.org/chemcomm

COMMUNICATION

STEP cement: Solar Thermal Electrochemical Production of CaO without CO_2 emission†

Stuart Licht,* Hongjun Wu,‡ Chaminda Hettige, Baohui Wang,‡ Joseph Asercion, Jason Lau and Jessica Stuart

Received 22nd February 2012, Accepted 5th April 2012
DOI: 10.1039/c2cc31341c

New molten salt chemistry allows solar thermal energy to drive calcium oxide production without any carbon dioxide emission. This is accomplished in a one pot synthesis, and at lower projected cost than the existing cement industry process, which after power production, is the largest contributor to anthropogenic greenhouse gas emissions.

Cement production accounts for 5–6% of all anthropogenic CO_2 emissions. Society consumes over 3×10^{12} kg of cement annually, and the cement industry releases 9 kg of CO_2 for each 10 kg of cement produced. The majority of CO_2 emissions occurs during the decarbonation of limestone ($CaCO_3$) to lime (CaO) described in eqn (1), and the remainder (30 to 40%) from burning fossil fuels, such as coal, to heat the kiln reactors to ~900 °C, eqn (2):[1–3]

ClimateCentral.org recently wrote that no other sector has such a high potential for drastic emission reductions, and while other processes are being explored to sequester cement's CO_2, none eliminate it. In forming CaO, solar thermal reactors have been studied as replacements to the fossil fuel heat in eqn (2).[4] However, the majority of the CO_2 emissions still occurs (as decarbonation in eqn (1)) in the conventional decarbonation of limestone to lime:

$$CaCO_3 + Q_{heat} \rightarrow CaO + CO_2 \quad (1)$$

$$nC + nO_2 \rightarrow nCO_2 + Q_{heat} \quad (2)$$

Here we show a new thermal chemistry, based on anomalies in oxide solubilites, to generate CaO, without CO_2 emission, in a high throughput, cost effective, environment conducive to the formation of cement. The aqueous solubility of $CaCO_3$ (6×10^{-5} m, where molal ≡ moles per kg solvent) is 3 orders of magnitude less than the 2×10^{-2} m solubility of calcium oxide, dissolving as calcium hydroxide. Surprisingly, this situation is reversed at high temperatures in molten carbonates, which allows the endothermic, electrolytic one pot synthesis, and precipitation of CaO.

Conducive to our new solar process,[5,6] electrolysis of molten carbonates forms oxides, which precipitate as calcium oxide when mixed with calcium carbonate. Thus no CO_2 is formed, to eliminate cement's greenhouse gas contribution to anthropogenic climate change.

In STEP cement limestone undergoes low energy electrolysis to produce (i) lime, (ii) O_2 and (iii) reduced carbonate without carbon dioxide emission. Alternative configurations of the electrolysis component of this STEP (Solar Thermal Electrochemical Production) are represented in Scheme 1. Compared to the

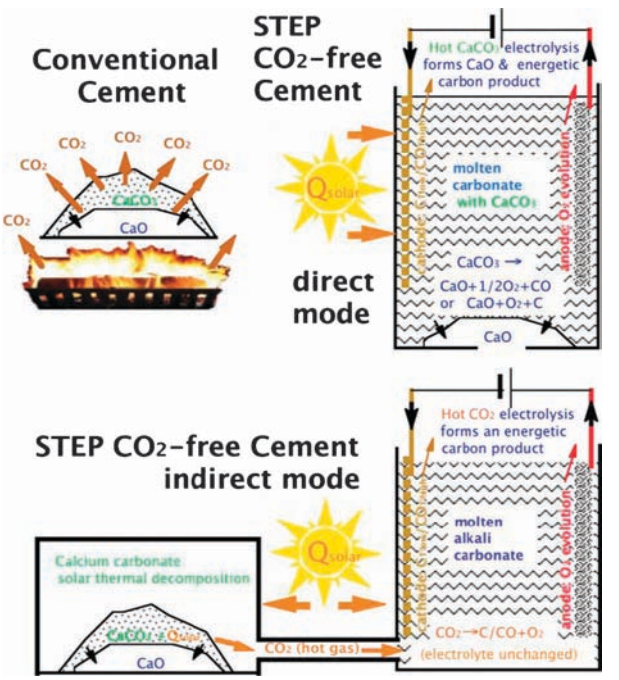

Scheme 1 Conventional thermal decomposition production of lime (top left) *versus* STEP direct solar conversion of calcium carbonate to calcium oxide (top right) eliminating CO_2. Carbonate electrolysis is endothermic requiring lower potential at higher temperature or carbonate concentration. Solar thermal energy provides the heat to lower this $E_{electrolysis}$. When this solar heated electrolysis energy is generated by a non-fossil fuel electricity source the process is fully carbon dioxide free. Bottom: the indirect mode of STEP cement as delineated in the ESI.†

Department of Chemistry, George Washington University, Ashburn, Virginia 20147, USA. E-mail: slicht@gwu.edu; Tel: 703 726 8215

† Electronic supplementary information (ESI) available: Expanded experimental details, stability, solubility and product analyses, economic assessment, STEP theory overview, STEP efficiencies and supplementary references. See DOI: 10.1039/c2cc31341c

‡ Present address: Northeast Petroleum Univ., Daqing, P. R. China.

conventional cement thermochemical process (top left), in the STEP cement direct electrolysis configuration (top right), solar thermal heated molten carbonates are electrolyzed forming oxides, which in the presence of calcium carbonate precipitate as lime:

$$\text{below 800 °C: } CaCO_3 + Q_{solar} + E_{electrolysis} \rightarrow CaO_{\downarrow} + C + O_2 \quad (3)$$

$$\text{above 800 °C: } CaCO_3 + Q_{solar} + E_{electrolysis} \rightarrow CaO_{\downarrow} + CO + 1/2O_2 \quad (4)$$

Heat significantly decreases the required electrolysis potentials needed to split calcium carbonate and to drive eqn (3) and (4), to below the electrolysis potential required at room temperature. Our calculated values are summarized on the top of Fig. 1. The unit activity thermodynamic electrolysis potential is lower for $CaCO_3$ than for lithium, sodium or potassium carbonate electrolyses. The high ratio of molten carbonate reactant to product is expected to further decrease the electrolysis potential.[5–7] Below 800 °C in the top figure, the energetically preferred (lower potential) carbon electrolysis product of $CaCO_3$ is solid carbon, while above that temperature CO is produced.

While calcium hydroxide is water soluble, calcium carbonate is highly insoluble in water, which leads to seashell stability. This situation is reversed at high temperatures in molten carbonates. Fig. 2, top, compares our measured solubility of oxides or calcium carbonate, in either molten lithium carbonate (squares) or a molten alkali carbonate mix (circles), to that of lithium oxide (triangles).

As measured in Fig. 2, at each temperature in either a eutectic mix of carbonates or in pure lithium carbonate, the solubility of calcium oxide is low, and ranges from 30 to 100 times less than the solubility of calcium carbonate, and 50 times less soluble than that of Li_2O. Beyond this low

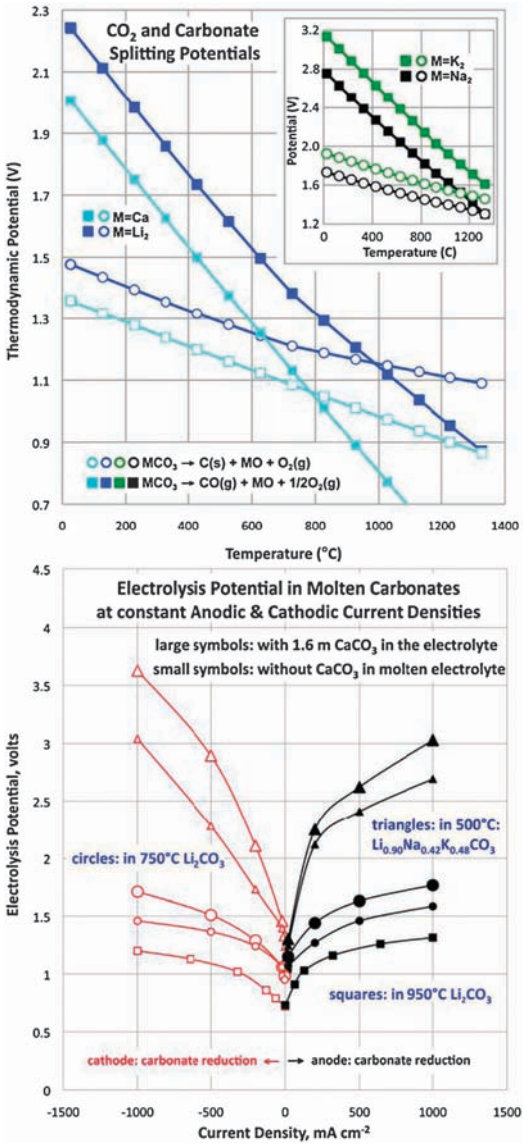

Fig. 1 CO_2 and carbonate splitting potentials. Top: The low thermodynamic potential to electrolyze calcium carbonate in the CO_2-free production of lime. Bottom: The measured full electrolysis potential as a function of current density in either Li_2CO_3 at 750 or 950 °C, or eutectic molten carbonates at 500 °C. At negative currents, the cathode is iron wire, and at positive current, the anode is either nickel or iridium wire (both yield similar electrolysis potentials).

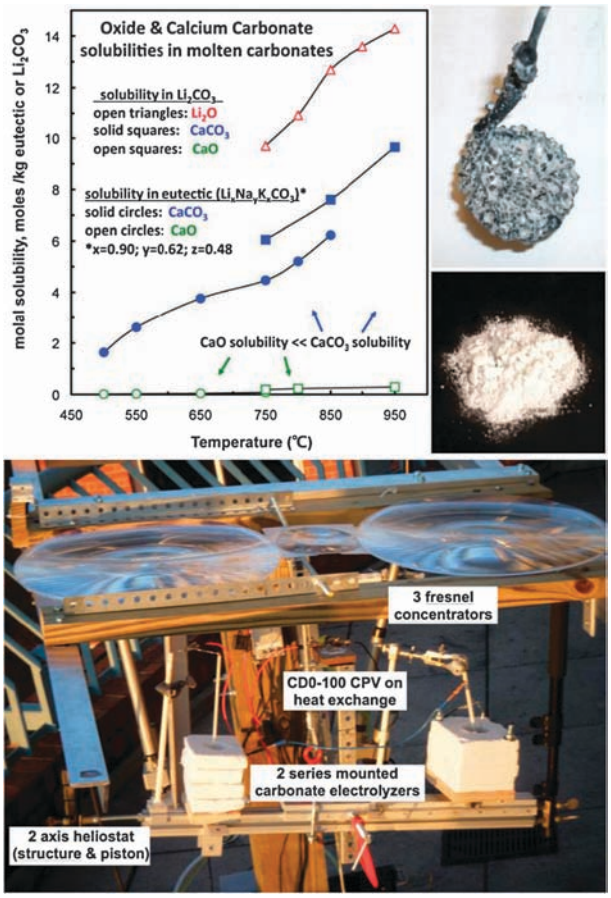

Fig. 2 The low solubility of calcium oxide, compared to calcium carbonate and lithium oxide solubility in molten carbonates (top) facilitates the electrolysis and precipitation of calcium oxide. STEP cement (bottom) with carbonate electrolyzers (detailed in the Electronic Supplementary Information (ESI†)), CPV and Fresnel concentrators mounted on a Suntura dual axis heliostat. Photographs of 5 h, 1 A 750 °C molten electrolysis products, upper: C and CaO from Li_2CO_3, lower: CaO from Li_2CO_3 containing 1 m Li_2O.

solubility of CaO, when molten carbonates undergo electrolysis to form oxides, added $CaCO_3$ will precipitate the desired CaO product for extraction, and the added carbonate replenishes the electrolyte for ongoing CaO production.

In 2009 we introduced the STEP theory of an efficient solar chemical process, based on a synergy of solar thermal and endothermic electrolyses.[5] Solar heat and high molten reactant concentration, substantially decreases the electrolysis energy.[6] As delineated in the ESI, experimentally, STEP can synthesize chemicals at solar efficiencies of 50%, as demonstrated with CO_2-free production of metals, fuels, and bleach.[6,7]

STEP cement, the direct CO_2-free synthesis of CaO from calcium carbonate is described and introduced in Scheme 1. In addition to the desired calcium oxide product, lower temperature electrolysis favors the dense storage of captured CO_2 as solid carbon (eqn (3)) at the cathode, while higher temperature electrolysis has the advantage of a lower electrolysis potential, and forms carbon monoxide at the cathode, a useful industrial reagent. The bottom of Fig. 1 summarizes the electrolysis potential measured in molten carbonates during the production of oxide. The indicated 1 A cm^{-2} is a high reaction rate, and higher rate, at even lower potential occurs with textured, or porous, rather than flat electrodes such as reticulated (spongy) Ni or iron. The oxide is formed at low energy (low electrolysis potential) and at high rate (high current densities), which is necessary to maintain production for commodities. For example aluminum is commercially produced at 0.8 A cm^{-2} in contemporary industrial plants.

Fig. 1 includes the measured full electrolysis potentials in a system constrained by either the anode or cathode surface area. Nickel and iridium are effective anode materials; CaO can improve nickel stability and decrease oxidative attack.[8,9] Steel is an effective cathode material in this system.

The electrolysis of carbonates is endothermic, which provides the opportunity to add a significant portion of the required energy to drive the process as solar thermal heat. A two axis Suntura heliostat provides orthonormal orientation to sun. Details of the 20 cm^2 steel cathode and 40 cm^2 nickel anode cathode electrolysis cell are included in the Electronic Supplementary Information (ESI†). As seen in the bottom of Fig. 2, concentrators direct sunlight to the CPV and electrolysis cells, and within minutes melt the electrolyte.

Electrolysis electrode surface areas were chosen to match the solar cell generated power, and the 2.7 V, 3.5 W drives two electrolysis cells in series at 750 °C and three in series at 950°. A Spectrolab CDO-100-C1MJ concentrator solar photovoltaic cell is used to generate 2.7 V at maximum power point, with solar to electrical energy efficiencies of 37% under 500 suns illumination. At maximum power, the 0.99 cm^2 cell generates 1.3 A at 100 suns, and when masked to 0.2 cm^2 area generates 1.4 A at 500 suns. Molten salt heat storage, as currently used in concentrator solar power CSP electricity plants, can be adapted to the STEP process. This will facilitate continuous operation independent of the sunlight variation, but has not yet been incorporated into this outdoor STEP calcium oxide generator. Intermittent and variable sunlight incident on this STEP configuration limits temperature and electric control, and long duration (5 h) electrolyses are conducted indoor at constant temperature and current. Indoors, the measured electrolysis potential is steady throughout the electrolysis. In pure, molten Li_2CO_3 the 0.1 A electrolysis occurs at 1.2 V, and at 1 A occurs at 1.6 V, or 0.9 V, respectively at 750 °C, or 950 °C. At 750 °C and 1 A, the addition of 1 m Li_2O lowers the observed potential to 1.5 V, and the addition of 1 to 6 m $CaCO_3$ increases the electrolysis potential to 1.8 V.

Constant current Li_2CO_3 electrolysis reduces carbonate, and produces Li_2O, which with the addition of $CaCO_3$ precipitates CaO (Fig. 2 photo), while oxygen evolves from the anode as oxygen solubility is low.[10,11] The precipitate is separately identified as CaO by FTIR, XRD, and AA analysis.† The products are CaO, C and oxygen without carbon dioxide evolution. The photo in Fig. 2 shows the carbon and CaO deposited after a 5 h electrolysis at 1 A, resulting in 0.56 g of carbon, 1.5 g of $O_{2(gas)}$ and 2.6 g of lime in quantitative accord with the 5 Ah, 4 electron splitting of carbonate.

This study presents a new chemistry of energy efficient, CO_2-free lime production, and the challenge of system scale-up awaits. It should be noted that the carbonate product is readily removed (dropping cleanly from the extracted steel wire cathode when it is uncoiled, or at higher temperature as a simple evolved gas CO), oxygen evolution is confined to the vicinity of the anode, and the high density calcium oxide product does not decompose in the molten carbonate and forms a slurry at the bottom of the vessel where it may be removed by tap in the same manner in which molten iron is removed from conventional iron production kilns.

In the present study new molten salt chemistry is found which allows solar thermal energy to drive CO_2-free lime production, in a one-pot synthesis, at lower projected cost than the existing cement industry process (details in ESI). After power production, the cement industry is largest single contributor to anthropogenic greenhouse gas emissions.

This work has been partially supported by NSF award 1006568.

References

1 Y. Liu, Y. Kuang, N. Huang, Z. Wu and C. Wang, *Int. J. Environ. Pollut.*, 2009, **37**, 369.
2 J. Allwood, J. Cullen and R. Milford, *Environ. Sci. Technol.*, 2010, **44**, 1888.
3 S. Haselbach, *J. Environ. Eng.*, 2009, **135**, 465.
4 A. Meier, E. Bonald, G. Cella, W. Lipinski and D. Wuillemin, *Sol. Energy*, 2006, **80**, 1355.
5 S. Licht, *J. Phys. Chem. C*, 2009, **113**, 16283.
6 S. Licht, *Adv. Mater.*, 2011, **23**, 5592.
7 S. Licht and H. Wu, *J. Phys. Chem. C*, 2011, **115**, 25138.
8 H. Yin, *et al.*, *Electrochim. Acta*, 2011, **56**, 3296.
9 Y. Yang, I. Sommerville and A. McLean, *Trans. Ind. Met.*, 2006, **59**, 655.
10 S. Scaccia and S. Frangini, *J. Mol. Liq.*, 2006, **129**, 133.
11 S. Scaccia and S. Frangini, *J. Mol. Liq.*, 2009, **146**, 39.

ADVANCED MATERIALS
www.advmat.de

Efficient Solar-Driven Synthesis, Carbon Capture, and Desalinization, STEP: Solar Thermal Electrochemical Production of Fuels, Metals, Bleach

*S. Licht**

STEP (solar thermal electrochemical production) theory is derived and experimentally verified for the electrosynthesis of energetic molecules at solar energy efficiency greater than any photovoltaic conversion efficiency. In STEP the efficient formation of metals, fuels, chlorine, and carbon capture is driven by solar thermal heated endothermic electrolyses of concentrated reactants occuring at a voltage below that of the room temperature energy stored in the products. One example is CO_2, which is reduced to either fuels or storable carbon at a solar efficiency of over 50% due to a synergy of efficient solar thermal absorption and electrochemical conversion at high temperature and reactant concentration. CO_2-free production of iron by STEP, from iron ore, occurs via Fe(III) in molten carbonate. Water is efficiently split to hydrogen by molten hydroxide electrolysis, and chlorine, sodium, and magnesium from molten chlorides. A pathway is provided for the STEP decrease of atmospheric carbon dioxide levels to pre-industial age levels in 10 years.

1. Introduction

The anthropogenic release of carbon dioxide and atmospheric carbon dioxide have reached record levels. One path towards CO_2 reduction is to utilize renewable energy to produce electricity. Another, less explored path is to utilize renewable energy to produce societal staples such as metals, bleach, and fuels (including carbonaceous fuels) directly. Whereas solar-driven water splitting to generate hydrogen fuels has been extensively studied,[1,2] there have been few studies of solar-driven carbon dioxide splitting, although recently we introduced a global process for solar thermal electrochemical production (STEP) of energetic molecules, including CO_2 splitting.[3–8] "CO_2 is a highly stable, noncombustible molecule, and its thermodynamic stability makes its activation energy demanding and challenging."[9] In search of a solution for climate change associated with increasing levels of atmospheric CO_2, the field of carbon dioxide splitting (solar or otherwise), while young, is growing rapidly, and as with water splitting, includes the study of photoelectrochemical, biomimetic, electrolytic, and thermal pathways of carbon dioxide splitting.[10,11]

The direct thermal splitting of CO_2 requires excessive temperatures to drive any significant dissociation. As a result, lower temperature thermochemical processes using coupled reactions have recently been studied.[12–16] The coupling of multiple reactions steps decreases the system efficiency. To date, such challenges, and the associated efficiency losses, have been an impediment to the implementation of the related, extensively studied field of thermochemical splitting of water.[2] Photo-electrochemistry probes the energetics of illuminated semiconductors in an electrolyte, and provides an alternative path to solar fuel formation. Photoelectrochemical solar cells (PECs) can convert solar energy to electricity,[17–21] and with inclusion of an electrochemical storage couple, have the capability for internal energy storage to provide a level output despite variations in sunlight.[22,23] Solar to photo-electrochemical energy can also be stored externally in chemical form, when it is used to drive the formation of energetically rich chemicals. With photochemical and photo-electrochemical splitting of carbon dioxide[24–29] the selective production of specific fuel products has been demonstrated. Such systems function at low current density and efficiencies of ~1 percent, and as with photoelectrochemical water splitting face stability and bandgap challenges related to effective operation with visible light.[21,30,31]

The electrically driven (nonsolar) electrolysis of dissolved carbon dioxide is under investigation at or near room temperature in aqueous, non-aqueous, and PEM media.[32–41] These are constrained by the thermodynamic and kinetic challenges associated with ambient temperature, endothermic processes, of a high electrolysis potential, large overpotential, low rate and low electrolysis efficiency. High-temperature, solid-oxide electrolysis of carbon dioxide dates back to suggestions from the 1960s to use such cells to renew air for a space habitat,[42–44] and the sustainable rate of the solid oxide reduction of carbon dioxide is improving rapidly.[45–51] Molten-carbonate rather than solid-oxide fuel cells running in the reverse mode had also been studied to renew air in 2002.[52] In a manner analogous to our 2002 high-temperature solar water-splitting studies (described below),[53–55] we showed in 2009 that molten-carbonate cells

Prof. S. Licht
Department of Chemistry
George Washington University
Washington, DC 20052, USA
E-mail: slicht@gwu.edu

DOI: 10.1002/adma.201103198

are particularly effective for solar-driven electrolysis of carbon dioxide,[3,4,8] and also for CO_2-free iron metal production.[5,6]

Light-driven water splitting was originally demonstrated with TiO_2 (a semiconductor with a bandgap, $E_g > 3.0$ eV).[56] However, only a small fraction of sunlight has sufficient energy to drive TiO_2 photoexcitation. Studies had sought to tune (lower) the semiconductor bandgap to provide a better match to the electrolysis potential.[57] In 2000 we used external multiple bandgap PVs (photovoltaics) to generate H_2 by splitting water at 18% solar energy conversion efficiency.[58] However, that room temperature process does not take advantage of additional, available thermal energy.

An alternative to tuning a semiconductor bandgap to provide a better match to the solar spectrum, is an approach to tune (lower) the electrolysis potential.[55] In 2002 we introduced a photo electrochemical thermal water splitting theory,[53] which was verified by experiment in 2003, for H_2 generation at over 30% solar energy conversion efficiency, and providing the first experimental demonstration that a semiconductor, such as Si (E_g = 1.1 eV), with bandgap lower than the standard water splitting potential ($E°_{H2O}$(25 °C) = 1.23 V), can directly drive hydrogen formation.[55] With increasing temperature, the quantitative decrease in the electrochemical potential to split water to hydrogen and oxygen had been well known by the 1950s.[59a,59b] In 1976 Wentworth and Chen wrote on "simple thermal decomposition reactions for storage of solar energy," with the limitation that the products of the reaction must be separated to prevent back reaction, and were without any electrochemical component.[60] As early as 1980 it was noted that thermal energy could decrease the necessary energy for the generation of H_2 by electrolysis.[61] However, that process would combine elements of solid state physics, insolation and electrochemical theory, complicating rigorous theoretical support of the process. Our photo-electrochemical thermal water splitting model for solar/H_2 by this process, was the first derivation of bandgap-restricted, thermal-enhanced, high solar water splitting efficiencies. The model, predicting solar energy conversion efficiencies that exceed those of conventional photovoltaics was initially derived for AM(Air Mass)1.5, terrestrial insolation, and later expanded to include sunlight above the atmosphere (AM0 insolation).[53,54] The experimental accomplishment followed, and established that the water splitting potential can be specifically tuned to match efficient photo-absorbers,[55] eliminating the challenge of tuning (varying) the semiconductor bandgap, and which can lead to over 30% solar to chemical energy conversion efficiencies. Our early process was specific to H_2 and did not incorporate the additional temperature enhancement of excess super-band gap energy and concentration enhancement of excess reactant to further decrease the electrolysis potential, in our contemporary STEP process.

Stuart Licht is a Professor of Chemistry at George Washington University, and was formerly a Program Director at the United States National Science Foundation. He completed his Ph.D. at the Weizmann Institute and was a postdoc at MIT. His current research interests include solar energy, multiple electron redox for highest capacity batteries an fuel cells, photoelectrochemistry, and a pathway to a renewable chemical economy.

2. Solar Thermal Electrochemical Production of Energetic Molecules: An Overview

2.1. STEP Theoretical Background

A single, small band gap junction, such as in a silicon PV, cannot generate the minimum photopotential required to drive many room temperature electrolysis reactions, as shown in the left of **Scheme 1**. The advancement of such studies had focused

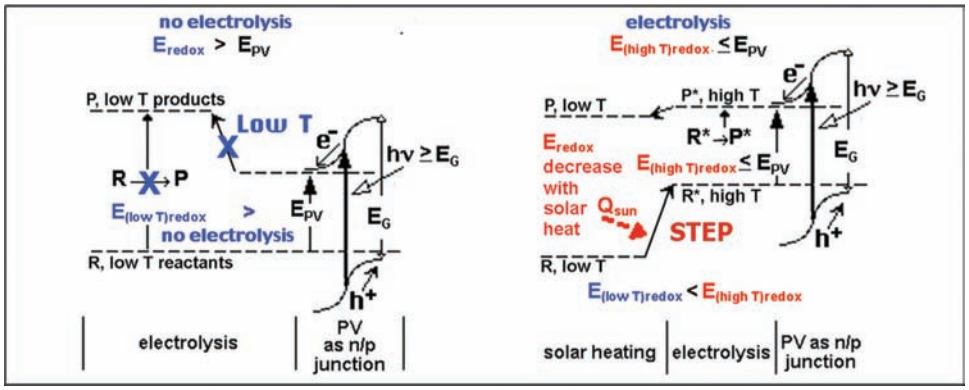

Scheme 1. Top: Comparison of PV and STEP solar driven electrolysis energy diagrams. STEP uses sunlight to drive otherwise energetically forbidden pathways of charge transfer. The energy of photodriven charge transfer is insufficient (left) to drive (unheated) electrolysis, but is sufficient (right) to drive endothermic electrolysis in the solar heated synergestic process. The process uses both visible & thermal solar energy for higher efficiency; thermal energy decreases the electrolysis potential forming an energetically allowed pathway to drive electrochemical charge transfer.

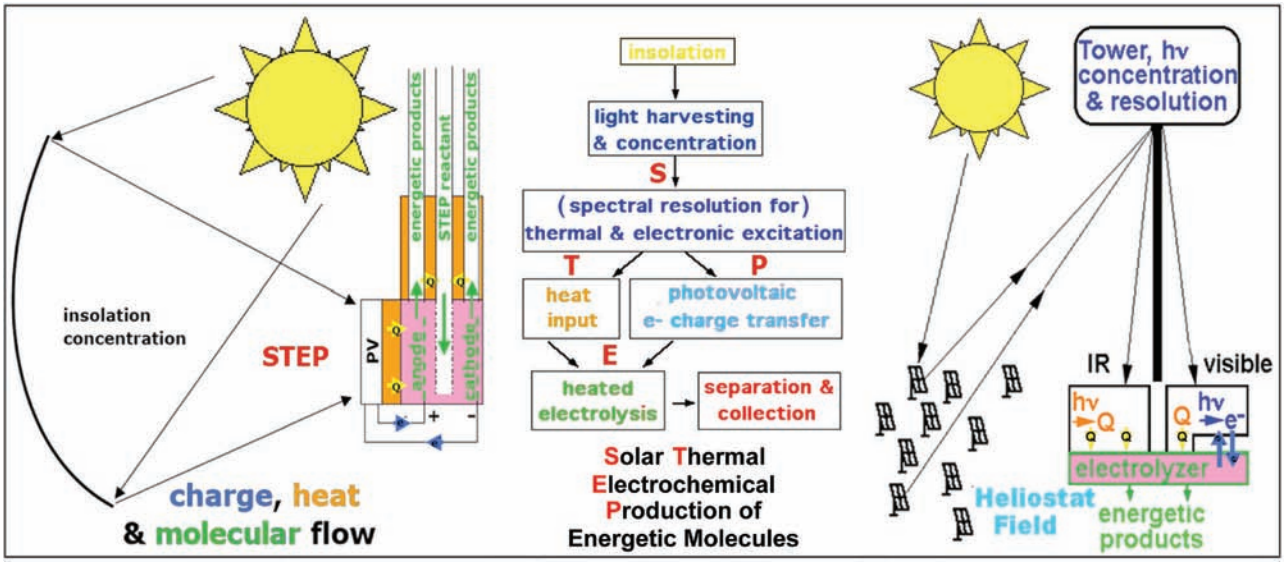

Scheme 2. Global use of sunlight to drive the formation of energy rich molecules. Left: Charge and heat flow in STEP: heat flow (yellow arrows), electron flow (blue), & reagent flow (green). Right: Beam splitters redirect sub-bandgap sunlight away from the PV onto the electrolyzer. Modified with permission.[3]

on tuning semiconductor bandgaps[57] to provide a better match to the electrochemical potential (specifically, the water splitting potential), or by utilizing more complex, multiple bandgap structures using multiple photon excitation.[58] Either of these structures are not capable of excitation beyond the bandedge and can not make use of longer wavelength sunlight. Photovoltaics are limited to super-bandgap sunlight, $h\nu > E_g$, precluding use of long wavelength radiation, $h\nu < E_g$. STEP instead directs this IR sunlight to heat electrochemical reactions, and uses visible sunlight to generate electronic charge to drive these electrolyses.

Rather than tuning the bandgap to provide a better energetic match to the electrolysis potential, the **STEP** process instead tunes the redox potential to match the bandgap. The right side of Scheme 1 presents the energy diagram of a STEP process. The high temperature pathway decreases the free energy requirements for processes whose electrolysis potential decreases with increasing temperature. STEP uses solar energy to drive, otherwise energetically forbidden, pathways of charge transfer. The process combines elements of solid state physics, insolation (solar illumination) and high temperature electrochemical energy conversion. Kinetics improve, and endothermic thermodynamic potentials, decrease with increasing temperature. The result is a synergy, making use of the full spectrum of sunlight, and capturing more solar energy. STEP is intrinsically more efficient than other solar energy conversion processes, as it utilizes not only the visible sunlight used to drive PVs, but also utilizes the previously detrimental (due to PV thermal degradation) thermal component of sunlight, for the electrolytic formation of chemicals.

The two bases for improved efficiencies using the STEP process are (i) excess heat, such as unused heat in solar cells, can be used to increase the temperature of an electrolysis cell, such as for electrolytic CO_2 splitting, while (ii) the product to reactant ratio can be increased to favor the kintetic and energetic formation of reactants. With increasing temperature, the quantitative decrease in the electrochemical potential to drive a variety of electrochemical syntheses is well known, substantially decreasing the electronic energy (the electrolysis potential) required to form energetic products. The extent of the decrease in the electrolysis potential, $E_{redox,}$ may be tuned by choosing the constituents and temperature of the electrolysis. The process distinguishes radiation that is intrinsically energy sufficient to drive PV charge transfer, and applies all excess solar thermal energy to heat the electrolysis reaction chamber.

Scheme 2 summarizes the charge, heat and molecular flow for the STEP process; the high temperature pathway decreases the potential required to drive endothermic electrolyses, and also facilitates the kinetics of charge transfer (i.e., decreases overpotential losses), which arise during electrolysis. This process consists of (i) sunlight harvesting and concentration, (ii) photovoltaic charge transfer driven by super-bandgap energy, (iii) transfer of sub-bandgap and excess super-bandgap radiation to heat the electrolysis chamber, (iv) high temperature, low energy electrolysis forming energy rich products, and (v) cycle completion by pre-heating of the electrolysis reactant through heat exchange with the energetic electrolysis products. As indicated on the right side of Scheme 2, the light harvesting can use various optical configurations; e.g. in lieu of parabolic, or Fresnel, concentrators, a heliostat/solar tower with secondary optics can achieve higher process temperatures (>1000 °C) with concentrations of ~2000 suns. Beam splitters can redirect sub-bandgap radiation away from the PV (minimzing PV heating) for a direct heat exchange with the electrolyzer.

Solar heating can decrease the energy to drive a range of electrolyses. Such processes can be determined using available entropy, S, and enthalpy, H, and free-energy, G, data,[59b] and are identified by their negative isothermal temperature coefficient

of the cell potential.[59a] This coefficient $(dE/dT)_{isoth}$ is the derivative of the electromotive force of the isothermal cell:

$$(dE/dT)_{isoth} = \Delta S/nF = (\Delta H - \Delta G)/nFT \quad (1)$$

The starting process of modeling any STEP process is the conventional expression of a generalized electrochemical process, in a cell which drives an n electron charge transfer electrolysis reaction, comprising "x" reactants, R_i, with stoichiometric coefficients r_i, and yielding "y" products, C_i, with stoichiometric coefficients c_i.

Electrode 1 | Electrolyte | Electrode 2

Using the convention of $E = E_{cathode} - E_{anode}$ to describe the positive potential necessary to drive a non-spontaneous process, by transfer of n electrons in the electrolysis reaction of reactants to products:

$$\sum_{i=1\ to\ x} r_i R_i \rightarrow \sum_{i=1\ to\ y} c_i C_i \quad (2)$$

At any electrolysis temperature, T_{STEP}, and at unit activity, the reaction has electrochemical potential, E°_T. This may be calculated from consistent, compiled unit activity thermochemical data sets, such as the NIST condensed phase and fluid properties data sets,[59b] as:

$$E^\circ_T = -\Delta G^\circ(T = T_{STEP})/nF;\ E^\circ_{ambient} \equiv E^\circ_T(T_{ambient});\ \text{here}$$
$$T_{ambient} = 298.15\ K = 25\ ^\circ C,\ \text{and:}$$
$$\Delta G^\circ(T = T_{STEP}) = \sum_{i=1\ to\ y} c_i(H^\circ(C_i, T) - TS^\circ(C_i, T))$$
$$-\sum_{i=1\ to\ x} r_i(H^\circ(R_i, T) - TS^\circ(Ri, T)) \quad (3)$$

Compiled thermochemical data are often based on different reference states, while a consistent reference state is needed to understand electrolysis limiting processes, including water.[62,63] This challenge is overcome by modification of the unit activity (a = 1) consistent calculated electrolysis potential to determine the potential at other reagent and product relative activities via the Nernst equation.[64,65] Electrolysis provides control of the relative amounts of reactant and generated product in a system. A substantial activity differential can also drive STEP improvement at elevated temperature, and will be derived. The potential variation with activity, a, of the Equation 2 reaction is given by: $\sum_{i=1\ to\ x} r_i R_i \rightarrow \sum_{i=1\ to\ y} c_i C_i$, is given by:

$$E_{T,a} = E^\circ_T - (RT/nF)\cdot \ln(\Pi_{i=1\ to\ x}\, a(R_i)^{r_i}/\Pi_{i=1\ to\ y}\, a(C_i)^{c_i}) \quad (4)$$

Electrolysis systems with a negative isothermal temperature coefficient tend to cool as the electrolysis products are generated. Specifically in endothermic electrolytic processes, the Equation 4 free-energy electrolysis potential, E_T, is less than the enthalpy based potential. This latter value is the potential at which the system temperature would remain constant during electrolysis. This thermoneutral potential, E_{tn}, is given by:

$$E_{tn}(T_{STEP}) = -\Delta H(T)/nF; \Delta H(T_{STEP})$$
$$= \sum_{i=1\ to\ b} c_i H(C_i, T_{STEP}) - \sum_{i=1\ to\ a} r_i H(R_i, T_{STEP}) \quad (5)$$

Two general STEP implementations are being explored. Both can provide the thermoneutral energy to sustain a variety of electrolyses. The thermoneutral potential, determined from the enthalpy of a reaction, describes the energy required to sustain an electrochemical process without cooling. For example, the thermoneutral potential we have calculated and reported for CO_2 splitting to CO and O_2 at unit activities, from Equation 5, is 1.46(±0.01) V over the temperature range of 25–1400 °C. As represented in **Scheme 3** on the left, the standard electrolysis

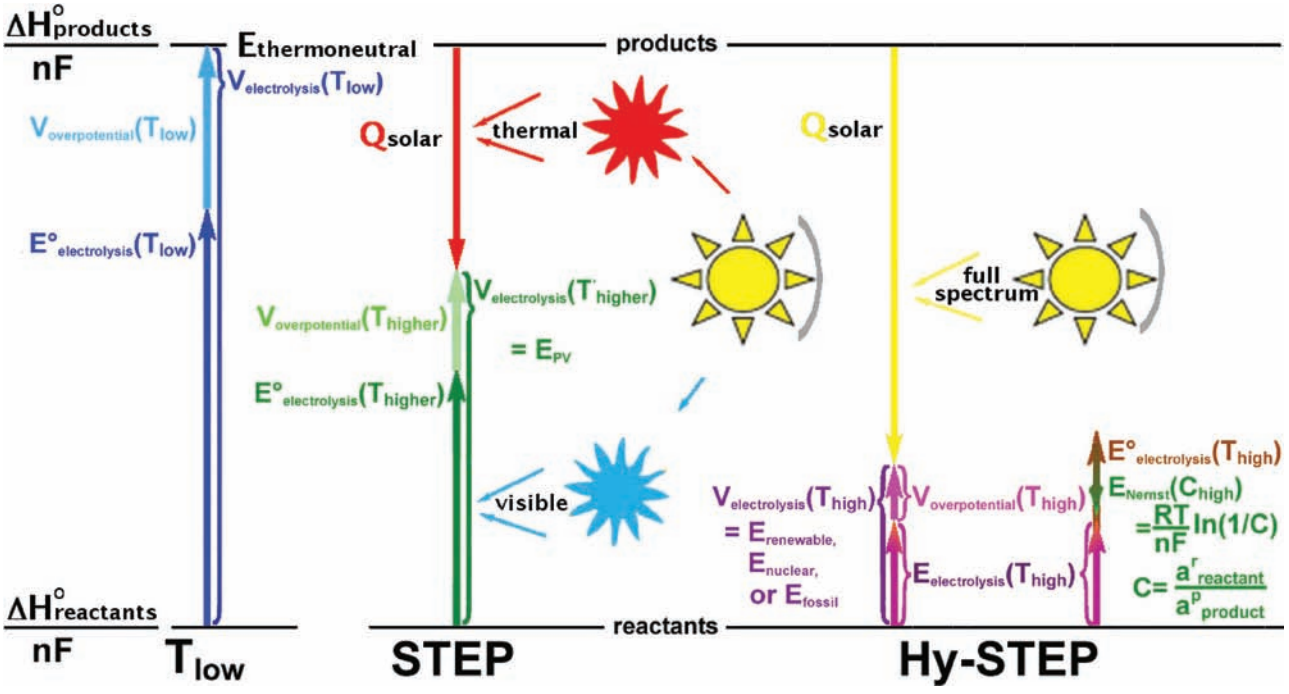

Scheme 3. Comparison of solar energy utilization in STEP and Hy-STEP implementations of the solar thermal electrochemical production of energetic molecules.

potential at room temperature, $E°$, can comprise a significant fraction of the thermoneutral potential. The first STEP mode, energetically represented next to the room temperature process in the scheme, separates sunlight into thermal and visible radiation. The solar visible generates electronic charge which drives electrolysis charge transfer. The solar thermal component heats the electrolysis and decreases both the $E°$ at this higher T, and the overpotential. The second mode, termed Hy-STEP (on the right) from "hybrid-STEP", does not separate sunlight, and instead directs all sunlight to heating the electrolysis, generating the highest T and smallest E, while the electrical energy for electrolysis is generated by a separate source (such as by photovoltaic, solar thermal electric, wind turbine, hydro, nuclear or fossil fuel generated electronic charge). As shown on the right side, high relative concentrations of the electrolysis reactant (such as CO_2 or iron oxide will further decrease the electrolysis potential).

2.2. STEP Solar to Chemical Energy Conversion Efficiency

The Hy-STEP mode is being studied outdoors with either wind or solar CPV (concentrator photovoltaic) generated electricity to drive $E_{electrolysis}$. The STEP mode is experimentally more complex and is presently studied indoors under solar simulator illumination. Determination of the efficiency of Hy-STEP with solar electric is straightforward in the domain in which $E_{electrolysis} < E_{thermoneutral}$ and the coulombic efficiency is high. Solar thermal energy is collected at an efficiency of $\eta_{thermal}$ to decrease the energy from $E_{thermoneutral}$ to $E_{electrolysis}$, and then electrolysis is driven at a solar electric energy efficiency of $\eta_{solar\text{-}electric}$:

$$\eta_{Hy-STEPsolar} = (\eta_{thermal}(E_{thermoneutral} - E_{electrolysis}) + \eta_{solar-electric} E_{electrolysis})/E_{thermoneutral} \quad (6)$$

$\eta_{thermal}$ is higher than $\eta_{solar\text{-}electric}$, and gains in efficiency occur in Equation 6 in the limit as $E_{electrolysis}$ approaches 0. $E_{electrolysis} = 0$ is equivalent to thermochemical, rather than electrolytic, production. As seen in **Figure 1**, at unit activity $E°_{CO2/CO}$ does not approach 0 until 3000 °C. Material constraints inhibit approach to this higher temperature, while electrolysis not only permits lower temperature, but also provides the advantage of spontaneous product seperation. At lower temperature, small values of $E_{electrolysis}$ can occur at higher reactant and lower product activities, as described in Equation 4. In the present configuration sunlight is concentrated at 75% solar to thermal efficiency, heating the electrolysis to 950 °C, which decreases the high current density CO_2 splitting potential to 0.9V, and the electrolysis charge is provided by CPV at 37% solar to electric efficiency. The solar to chemical energy conversion efficiency is in accordance with Equation 6:

$$\eta_{Hy-STEPsolar} = (75\%(1.46V - 0.90V) + 37\%0.90V)/1.46V = 52\% \quad (7)$$

A relatively high concentration of reactants lowers the voltage of electrolysis via the Nernst term in Equation 4. With appropriate choice of high temperature electrolyte, this effect can be dramatic, for example both in STEP iron and in comparing the benefits of the molten carbonate to solid oxide (gas phase) reactants for STEP CO_2 electrolytic reduction, sequestration and fuel formation. Fe(III) (as found in the common iron ore, hematite) is nearly insoluble in sodium carbonate, while it is soluble to over 10 m (molal) in lithium carbonate,[6] and as discussed in Section 2.3, molten carbonate electrolyzer provides 10^3 to 10^6 times higher concentration of reactant at the cathode surface than a solid oxide electrolyzer.

In practice, for STEP iron or carbon capture, we simultaneously drive lithium carbonate electrolysis cells together in series, at the CPV maximum power point (**Figure 2**). Specifically, a Spectrolab CDO-100-C1MJ concentrator solar cell is used to generate 2.7 V at maximum power point, with solar to electrical energy efficiencies of 37% under 500 suns illumination. As seen in Figure 2, at maximum power, the 0.99 cm^2 cell generates 1.3 A at 100 suns, and when masked to 0.2 cm^2 area generates 1.4 A at 500 suns. Electrolysis electrode surface areas were chosen to match the solar cell generated power. At 950 °C at 0.9V, the electrolysis cells generate carbon monoxide at 1.3 to 1.5 A (the electrolysis current stability is shown at the bottom of Figure 2).

In accord with Equation 6 and Scheme 3, Hy-STEP efficiency improves with temperature increase to decrease overpotential and $E_{electrolysis}$, and with increase in the relative reactant activity. Higher solar efficiencies will be expected, both with more effective carbonate electrocatalysts (as morphologies with higher effective surface area and lower overpotential) are developed, and as also as PV efficiencies increase. Increases in solar to electric (both PV, CPV and solar thermal-electric) efficiencies continue to be reported, and will improve Equation 7 efficiency. For example, multijunction CPV have been reported improved to $\eta_{PV} = 40.7\%$.[69]

Engineering refinements will improve some aspects, and decrease other aspects, of the system efficiency. Preheating the CO_2, by circulating it as a coolant under the CPV (as we currently do in the indoor STEP experiment, but not outdoor, Hy-STEP experiments) will improve the system efficiency. In the present configuration outgoing CO and O_2 gases at the cathode and anode heat the incoming CO_2. Isolation of the electrolysis products will require heat exchangers with accompanying radiative heat losses, and for electrolyses in which there are side reactions or product recombination losses, $\eta_{Hy\text{-}STEP\ solar}$ will decrease proportional to the decrease in coulombic efficiency. At present, wind turbine generated electricity is more cost effective than solar-electric, and we have demonstrated a Hy-STEP process with wind-electric, for CO_2 free production of iron (delineated in Section 3.3). Addition of long-term (overnight) molten salt insulated storage will permit continuous operation of the STEP process. Both STEP implementations provide a basis for practical, high solar efficiencies.

Components for STEP CO_2 capture and conversion to solid carbon are represented on the left side of Figure 2, and are detailed in references [4–7]. A 2.7 V CPV phootopotential drives three in series electrolyses at 950°C. Fundamental details of the heat balance are provided in reference 4. The CPV has an experimental solar efficiency of 37%, and the 63% of insolation not converted to electricity comprises a significant heat source. The challenge is to direct a substantial fraction of this heat to the electrolysis. An example of this challenge is in the first stage of

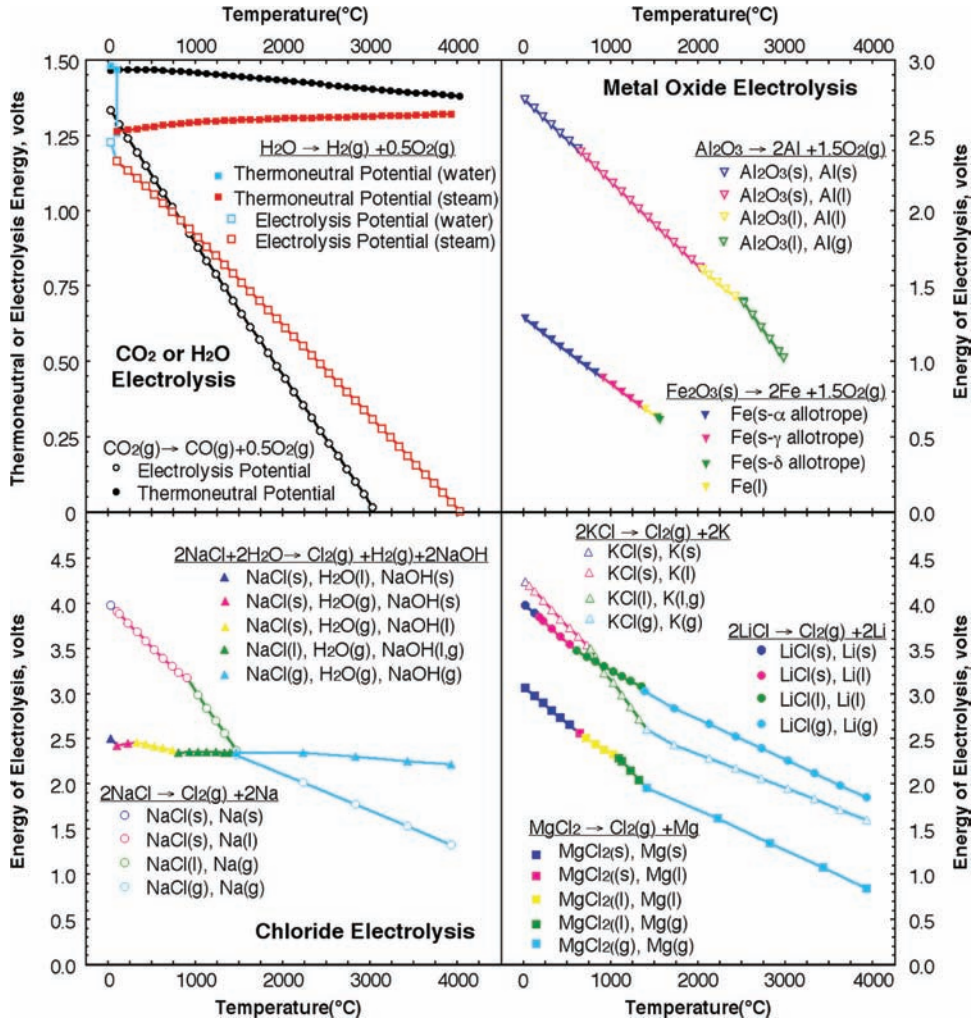

Figure 1. The calculated potential to electrolyze selected oxides (top) and chlorides (bottom). The indicated decrease in electrolysis energy, with increase in temperature, provides energy savings in the STEP process in which high temperature is provided by excess solar heat. Energies of electrolysis are calculated from Equation 3, with consistent thermochemical values at unit activity using NIST gas and condensed phase Shomate equations.[59b] Note with water excluded, the chloride electrolysis decreases (in the lower left of the figure). All other indicated electrolysis potentials, including that of water or carbon dioxide, decrease with increasing temperature. Thermoneutral potentials are calculated with Equation 5. Modified with permission from [3].

heating, in which higher temperatures increases CO_2 preheat, but diminishes the CPV power. Heating of the reactant CO_2 is a three tier process in the current configuration: the preheating of room temperature CO_2 consists of either (1a) flow-through a heat exchange fixed to the back of the concentrator solar cell and/or (1b) preheating to simulate CO_2 extracted from an available heat source such as a hot smoke (flue) stack, (2) secondary heating consists of passing this CO_2 through a heat exchange with the outgoing products, (3) tertiary heat is applied through concentrated, split solar thermal energy (Figure 2).

An upper limit to the energy required to maintain a constant system temperature is given in the case in which neither solar IR, excess solar visible, nor heat exchange from the environment or products would be applied to the system. When an 0.90 V electrolysis occurs, an additional 0.56 V, over E_{tn} = 1.46 V, is required to maintain a constant system temperature. Hence, in the case of three electrolyses in series, as in Figure 2, an additional 3 × 0.56 V = 1.68 V will maintain constant temperature. This is less than the 63% of the solar energy (equivalent to 4.6 V) not used in generating the 2.7 V of maximum power point voltage of electronic charge from the CPV in this experiment. Heating requirements are even less, when the reactant activity is maintained at a level that is higher than the product activity. For example, this is accomplished when products are continuously removed to ensure that the partial pressure of the products is lower than that of the CO_2. This lowers the total heat required for temperature neutrality to below that of the unit activity thermoneutral potential 1.46 V.

The STEP effective solar energy conversion efficiency, η_{STEP}, is constrained by both photovoltaic and thermal boost conversion efficiencies, η_{PV} and $\eta_{thermal\text{-}boost}$.[8] Here, the CPV sustains a conversion efficiency of η_{PV} = 37.0%. In the system, passage of electrolysis current requires an additional, combined (ohmic, anodic, and cathodic over-) potential above the thermodynamic potential. However, mobility and kinetics improve at higher temperature to decrease this overpotential. The generated CO

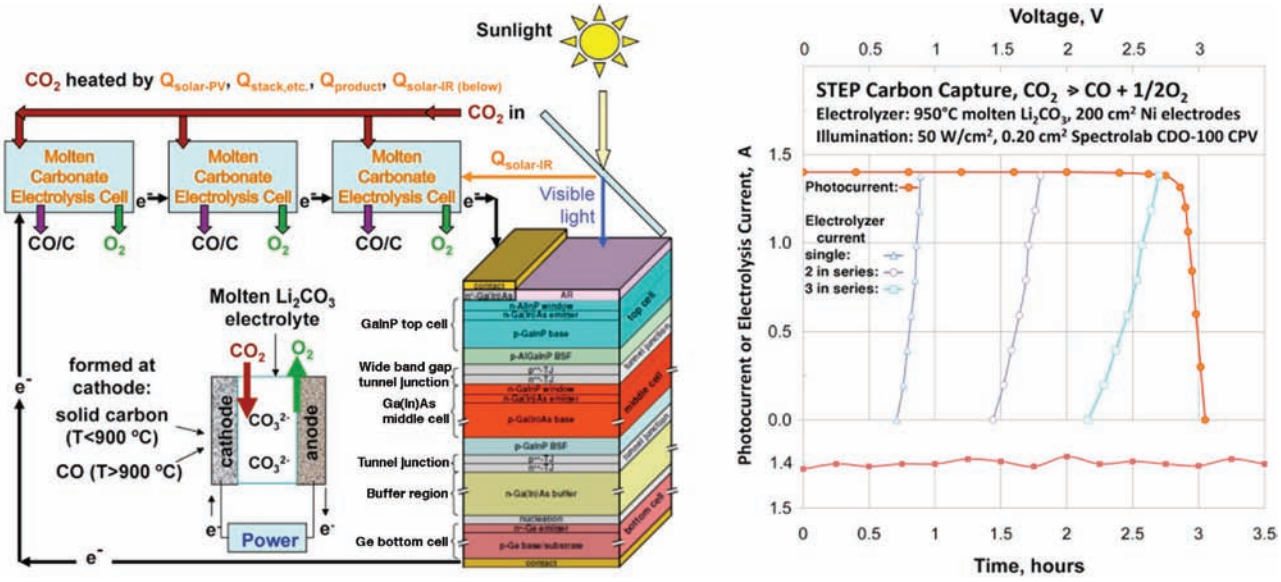

Figure 2. Left: STEP carbon capture in which three molten carbonate electrolysis in series are driven by a concentrator photovoltaic. Sunlight is split into two spectral regions; visible drives the CPV and thermal heats the electrolysis cell. In Hy-STEP (not shown) sunlight is not split and the full spectrum heats the electrolysis cell, and electronic charge is generated separately by solar, wind, or other source. Right: The maximum power point photovoltage of one Spectrolab CPV is sufficient to drive three in series carbon dioxide splitting 950 °C molten Li_2CO_3 electrolysis cells. Top: Photocurrent at 500 suns (masked (0.20 cm^2) Spectrolab CDO-100 CPV, or electrolysis current, versus voltage; electrolysis current is shown of one, two or three series 950 °C Li_2CO_3 electrolysis cells with 200 cm^2 Ni electrodes. Three in series electrolysis cells provide a power match at the 2.7 V maximum power point of the CPV at 950 °C; similarly (not shown), two 750 °C Li_2CO_3 electrolysis cells in series provide a power match at 2.7V to the CPV. Bottom: Stable carbon capture (with 200 cm^2 "aged" Ni electrodes at 750 °C; fresh electrodes (not shown) exhibit an initial fluctuation as carbon forms at the cathode and Ni oxide layer forms on the anode. The rate of solid carbon deposition gradually increases as the cathode surface area slowly increases in time. Modified with permission from [4].

contains an increase in oxidation potential compared to carbon dioxide at room temperature ($E_{CO2/CO}(25\ °C) = 1.33$ V for $CO_2 \rightarrow CO + 1/2\ O_2$ in Figure 1), an increase of 0.43 V compared to the 0.90 V used to generate the CO. The electrolysis efficiency compares the stored potential to the applied potential, $\eta_{\text{thermal-boost}} = E°_{\text{electrolysis}}(25\ °C)/V_{\text{electrolysis}}(T)$.[4] Given a stable temperature electrolysis environment, the experimental STEP solar to CO carbon capture and conversion efficiency is the product of this relative gain in energy and the electronic solar efficiency:

$$\eta_{\text{STEP}} = \eta_{\text{PV}} \cdot \eta_{\text{thermal-boost}} = 37.0\% \cdot (1.33\ \text{V}/0.90\ \text{V}) = 54.7\% \quad (8)$$

Ohmic and overpotential losses are already included in the measured electrolysis potential. This 54.7% STEP solar conversion efficiency is an upper limit of the present experiment, and as with the Hy-STEP mode, improvements are expected in electrocatalysis and CPV efficiency. Additional losses will occur when beam splitter and secondary concentrator optics losses, and thermal systems matching are incorporated, but serves to demonstrate the synergy of this solar/photo/electrochemical/thermal process, leads to energy efficiency higher than that for solar generated electricity,[69] or for photochemical,[70] photoelectrochemical,[21,27] solar thermal,[71] or other CO_2 reduction processes.[72]

The CPV does not need, nor function with, sunlight of energy less than that of the 0.67 eV bandgap of the multijunction Ge bottom layer. From our previous calculations, this thermal energy comprises 10% of AM1.5 insolation, which will be further diminished by the solar thermal absorption efficiency and heat exchange to the electrolysis efficiency,[54] and under 0.5 MW m^{-2} of incident sunlight (500 suns illumination), yields ~50 kW m^{-2}, which may be split off as thermal energy towards heating the electrolysis cell without decreasing the CPV electronic power. The CPV, while efficient, utilizes less than half of the super-bandgap (hν > 0.67 eV) sunlight. A portion of this > ~250 kW m^{-2} available energy, is extracted through heat exchange at the backside of the CPV. Another useful source for consideration as supplemental heat is industrial exhaust. The temperature of industrial flue stacks varies widely, with fossil fuel source and application, and ranges up to 650 °C for an open circuit gas turbine. The efficiency of thermal energy transfer will limit use of this available heat.

A lower limit to the STEP efficiency is determined when no heat is recovered, either from the CPV or remaining solar IR, and when heat is not recovered via heat exchange from the electrolysis products, and when an external heat source is used to maintain a constant electrolysis temperature. In this case, the difference between the electrolysis potential and the thermoneutral potential represents the enthalpy required to keep the system from cooling. In this case, our 0.9 V electrolysis occurs at an efficiency of (0.90V/1.46V) · 54.7% = 34%. While the STEP energy analysis, detailed in Section 4.2 for example for CO_2 to CO splitting, is more complex than that of the Hy-STEP mode, more solar thermal energy is available including a PV's unused or waste heat to drive the process and to improve the solar to chemical energy conversion efficiency. We determine the STEP solar efficiency over the range from inclusion of no solar

thermal heat (based on the enthalpy, rather than free energy, of reaction) to the case where the solar thermal heat is sufficient to sustain the reaction (based on the free energy of reaction). This determines the efficiency range, as chemical flow out to the solar flow in (as measured by the increase in chemical energy of the products compared to the reactants), from 34% to over 50%.

2.3. Identification of STEP Consistent Endothermic Processes

The electrochemical driving force for a variety of chemicals of widespread use by society will be shown to significantly decrease with increasing temperature. As calculated and summarized in the top left of Figure 1, the electrochemical driving force for electrolysis of either carbon dioxide or water, significantly decreases with increasing temperature. The ability to remove CO_2 from exhaust stacks or atmospheric sources, provides a response to linked environmental impacts, including global warming due to anthropogenic CO_2 emission. From the known thermochemical data for CO_2, CO and O_2, and in accord with Equation 1, CO_2 splitting can be described by:

$$CO_2(g) \rightarrow CO(g) + 1/2O_2(g);$$

$$E^\circ CO_2 split = (G^\circ CO + 0.5G^\circ O_2 - G^\circ CO_2)/2F; E^\circ(25\,^\circ C) = 1.333\ V \quad (9)$$

As an example of the solar energy efficiency gains, this progress report focuses on CO_2 splitting potentials, and provides examples of other useful STEP processes. As seen in Figure 1, CO_2 splitting potentials decrease more rapidly with temperature than those for water splitting, signifying that the STEP process may be readily applied to CO_2 electrolysis. Efficient, renewable, non-fossil fuel energy rich carbon sources are needed, and the product of Equation 9, carbon monoxide is a significant industrial gas with a myriad of uses, including the bulk manufacturing of hydrocarbon fuels, acetic acid and aldehydes (and detergent precursors), and for use in industrial nickel purification.[66] To alleviate challenges of fossil-fuel resource depletion, CO is an important syngas component and methanol is formed through the reaction with H_2. The ability to remove CO_2 from exhaust stacks or atmospheric sources, also limits CO_2 emission. Based on our original analogous experimental photo-thermal electrochemical water electrolysis design,[55] the first CO_2 STEP process consists of solar driven and solar thermal assisted CO_2 electrolysis. In particular, in a molten carbonate bath electrolysis cell, fed by CO_2.

$$\text{cathode}: \quad 2CO_2(g) + 2e^- \rightarrow CO_3\ (\text{molten}) + CO(g)$$

$$\text{anode}: \quad CO_3\ (\text{molten}) \rightarrow CO_2(g) + 1/2O_2(g) + 2e^-$$

$$\text{cell}: \quad CO_2(g) \rightarrow CO(g) + 1/2O_2(g) \quad (10)$$

Molten alkali carbonate electrolyte fuel cells typically operate at 650 °C. Li, Na or K cation variation can affect charge mobility and operational temperatures. Sintered nickel often serves as the anode, porous lithium doped nickel oxide often as the cathode, while the electrolyte is suspended in a porous, insulating, chemically inert $LiAlO_2$ ceramic matrix.[67]

Solar thermal energy can be used to favor the formation of products for electrolyses characterized by a negative isothermal temperature coefficient, but will not improve the efficiency of heat neutral or exothermic reactions. An example of this restriction occurs for the electrolysis reaction currently used by industry to generate chlorine. During 2008, the generation of chlorine gas (principally for use as bleach and in the chlor-alkali industry) consumed approximately 1% of the world's electricity,[68] prepared in accord with the industrial electrolytic process:

$$2NaCl + 2H_2O \rightarrow Cl_2 + H_2 + 2NaOH; E^\circ(25\,^\circ C) = 2.502\ V \quad (11)$$

In the lower left portion of Figure 1, the calculated electrolysis potential for this industrial chlor-alkali reaction exhibits little variation with temperature, and hence the conventional generation of chlorine by electrolysis would not benefit from the inclusion of solar heating. This potential is relatively invariant, despite a number of phase changes of the components (indicated on the figure and which include the melting of NaOH or NaCl). However, as seen in the figure, the calculated potential for the anhydrous electrolysis of chloride salts is endothermic, including the electrolyses to generate not only chlorine, but also metallic lithium, sodium and magnesium, and can be greatly improved through the STEP process:

$$MCl_n \rightarrow n/2Cl_2 + M;$$

$$E^\circ MCl_n\ split(25\,^\circ C) = 3.98\ V - M \text{ for M = Li or Na; } 4.24\ V \text{ for M = K; } 3.07\ V \text{ for M = Mg} \quad (12)$$

The calculated decrease for the anhydrous chloride electrolysis potentials are on the order of volts per 1000 °C temperature change. For example, from 25 °C up to the $MgCl_2$ boiling point of 1412 °C, the $MgCl_2$ electrolysis potential decreases from 3.07 V to 1.86 V. This decrease provides a theoretical basis for significant, non CO_2 emitting, non-fossil fuel consuming processes for the generation of chlorine and magnesium, to be delineated in Section 3.4, and occurring at high solar efficiency analogous to the similar CO_2 STEP process.

In Section 3.2 the STEP process will be derived for the efficient solar removal/ recycling of CO_2. In addition, thermodynamic calculation of metal and chloride electrolysis rest potentials identifies electrolytic processes which are consistent with endothermic processes for the formation of iron, chlorine, aluminum, lithium, sodium and magnesium, via CO_2-free pathways. As shown, the conversion and replacement of the conventional, aqueous, industrial alkali-chlor process, with an anhydrous electrosynthesis, results in a redox potential with a calculated decrease of 1.1 V from 25 to 1000 °C.

As seen in the top right of Figure 1, the calculated electrochemical reduction of metal oxides can exhibit a sharp, smooth decrease in redox potential over a wide range of phase changes. These endothermic process provide an opportunity for the replacement of conventional industrial processes by the STEP formation of these metals. In 2008, industrial electrolytic processes consumed ~5% of the world's electricity, including for aluminum (3%), chlorine (1%), and lithium, magnesium and sodium production. This 5% of the global 19×10^{12} kWh of electrical production, is equivalent to the emission

of 6×10^8 metric tons of CO_2.[68] The iron and steel industry accounts for a quarter of industrial direct CO_2 emissions. Currently, iron is predominantly formed through the reduction of hematite with carbon, emitting CO_2:

$$Fe_2O_3 + 3C + 3/2O_2 \rightarrow 2Fe + 3CO_2 \quad (13)$$

A non-CO_2 emitting alternative is provided by the STEP driven electrolysis of Fe_2O_3:

$$Fe_2O_3 \rightarrow 2Fe + 3/2O_2 \quad E^\circ = 1.28\ V \quad (14)$$

As seen in the top right of Figure 1, the calculated iron generating electrolysis potentials drops 0.5 V (a 38% drop) from 25 °C to 1000 °C, and as with the CO_2 analogue, will be expected to decrease more rapidly with high iron oxide activity conditions. Conventional industrial processes for these metals and chlorine, along with CO_2 emitted from power and transportation, are responsible for the majority of anthropogenic CO_2 release. The STEP process, to efficiently recover carbon dioxide and in lieu of these industrial processes, can provide a transition beyond the fossil fuel-electric grid economy.

The top left of Figure 1 includes calculated thermoneutral potentials for CO_2 and water splitting reactions. At ambient temperature, the difference between E_{th} and E_T does not indicate an additional heat requirement for electrolysis, as this heat is available via heat exchange with the ambient environment. At ambient temperature, $E_{tn} - E_T$ for CO_2 or water is respectively 0.13 and 0.25 V, is calculated (not shown) as 0.15 ± 0.1 V for Al_2O_3 and Fe_2O_3, and 0.28 ± 0.3 V for each of the chlorides.

We find that molten electrolytes present several fundamental advantages compared to solid oxides for CO_2 electrolysis. (i) Molten carbonate electrolyzer provides 10^3 to 10^6 times higher concentration of reactant at the cathode surface than a solid oxide electrolyzer. Solid oxides utilize gas phase reactants, whereas carbonates utilize molten phase reactants. Molten carbonate contains 2×10^{-2} mol reducible tetravalent carbon/ cm^3. The density of reducible tetravalent carbon sites in the gas phase is considerably lower. Air contains 0.03% CO_2, equivalent to only 1×10^{-8} mol of tetravalent carbon/ cm^3, and flue gas (typically) contains 10-15% CO_2, equivalent to 2×10^{-5} mol reducible C(IV)/ cm^3. Carbonate's higher concentration of active, reducible tetravalent carbon sites, logarithmically decreases the electrolysis potential, and can facilitate charge transfer at low electrolysis potentials. (ii) Molten carbonates can directly absorb atmospheric CO_2, whereas solid oxides require an energy consuming pre-concentration process. (iii) Molten carbonates electrolyses are compatible with both solid and gas phase products. (iv) Molten processes have an intrinsic thermal buffer not found in gas phase systems. Sunlight intensity varies over a 24-hour cycle, and more frequently with variations in cloud cover. This disruption to other solar energy conversion processes is not necessary in molten salt processes. For example as discussed in Section 4.3, the thermal buffer capacity of molten salts has been effective for solar to electric power towers to operate 24/7. These towers concentrate solar thermal energy to heat molten salts, which circulate and via heat exchange boil water to drive conventional mechanical turbines.

3. Demonstrated STEP Processes

3.1. STEP Hydrogen

STEP occurs at both higher electrolysis and higher solar conversion efficiencies than conventional room temperature photovoltaic (PV) generation of hydrogen. Experimentally, we demonstrated a sharp decrease in the water splitting potential in an unusual molten sodium hydroxide medium, **Figure 3**, and as shown in **Figure 4**, three series connected Si CPVs efficiently driving two series molten hydroxide water splitting cells at 500 °C to generate hydrogen.[55]

Recently we have considered the economic viability of solar hydrogen fuel production. That study provided evidence that the STEP system is an economically viable solution for the production of hydrogen.[55]

3.2. STEP Carbon Capture

In this process carbon dioxide is captured directly, without the need to pre-concentrate dilute CO_2, using a high temperature electrolysis cell powered by sunlight in a single step. Solar thermal energy decreases the energy required for the endothermic

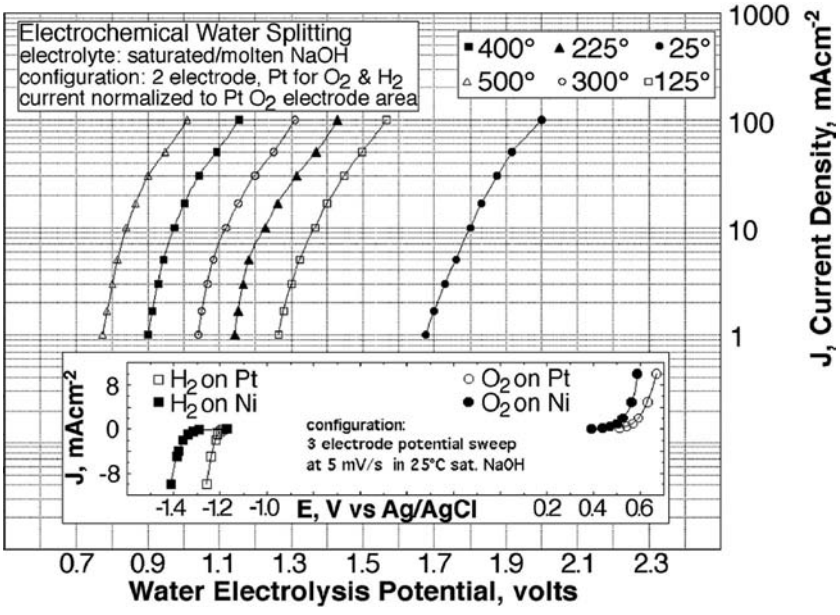

Figure 3. Water electrolysis potential, measured in aqueous saturated or molten NaOH, at 1 atm. Steam is injected in the molten electrolyte. The O_2 anode is 0.6 cm^2 Pt foil. IR and polarization losses are minimized by sandwiching 5 mm from each side of the anode, oversized Pt gauze cathode. Inset: At 25 °C, 3 electrode values comparing Ni and Pt working electrodes and with a Pt gauze counterelectrode at 5 mV/s.

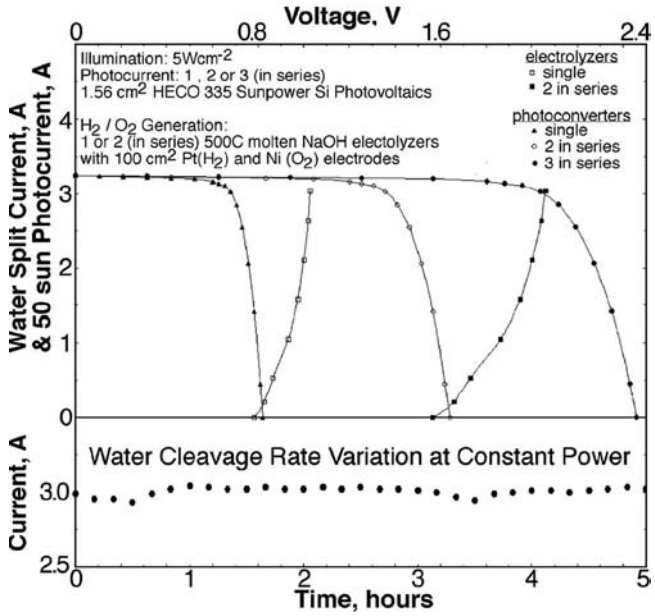

Figure 4. Photovoltaic and electrolysis charge transfer of STEP hydrogen using Si CPV's driving molten NaOH water electrolysis. The photocurrent is shown for 1, 2, or 3 1.561 cm^2 HECO 335 Sunpower Si photovoltaics in series at 50 suns. The CPVs drive 500 °C molten NaOH steam electrolysis using Pt gauze electrodes. Left inset: electrolysis current stability.

conversion of carbon dioxide and kinetically facilitates electrochemical reduction, while solar visible generates electronic charge to drive the electrolysis. CO_2 can be captured as solid carbon and stored, or used as carbon monoxide to feed chemical or synthetic fuel production. Thermodynamic calculations are used to determine, and then demonstrate, a specific low energy, molten carbonate salt pathway for carbon capture.

Prior investigations of the electrochemistry of carbonates in molten salts tended to focus on reactions of interest to fuel cells,[67] rather than the (reverse) electrolysis reactions of relevance to the STEP reduction of carbon dioxide, typically in alkali carbonate mixtures. Such mixtures substantially lower the melting point compared to the pure salts, and would provide the thermodynamic maximum voltage for fuel cells. However, the electrolysis process is maximized in the opposite temperature domain of fuel cells, that is at elevated temperatures which decrease the energy of electrolysis, as schematically delineated in Scheme 1. These conditions provide a new opportunity for effective CO_2 capture.

CO_2 electrolysis splitting potentials are calculated from the thermodynamic free energy components of the reactants and products[3,4,59b] as $E = -\Delta G(\text{reaction})/nF$, where $n = 4$ or 2 for the respective conversion of CO_2 to the solid carbon or carbon monoxide products. As calculated using the available thermochemical enthalpy and entropy of the starting components, and as summarized in the left side of **Figure 5**, molten Li_2CO_3, via a Li_2O intermediate, provides a preferred, low energy route compared to Na_2CO_3 or K_2CO_3 (via Na_2O or K_2O), for the conversion of CO_2. High temperature is advantageous as it decreases the free energy energy necessary to drive the STEP endothermic process. The carbonates, Li_2CO_3, Na_2CO_3 and K_2CO_3, have respective melting points of 723, 851, and 891 °C. Molten Li_2CO_3 not only requires lower thermodynamic electrolysis energy, but in addition has higher conductivity

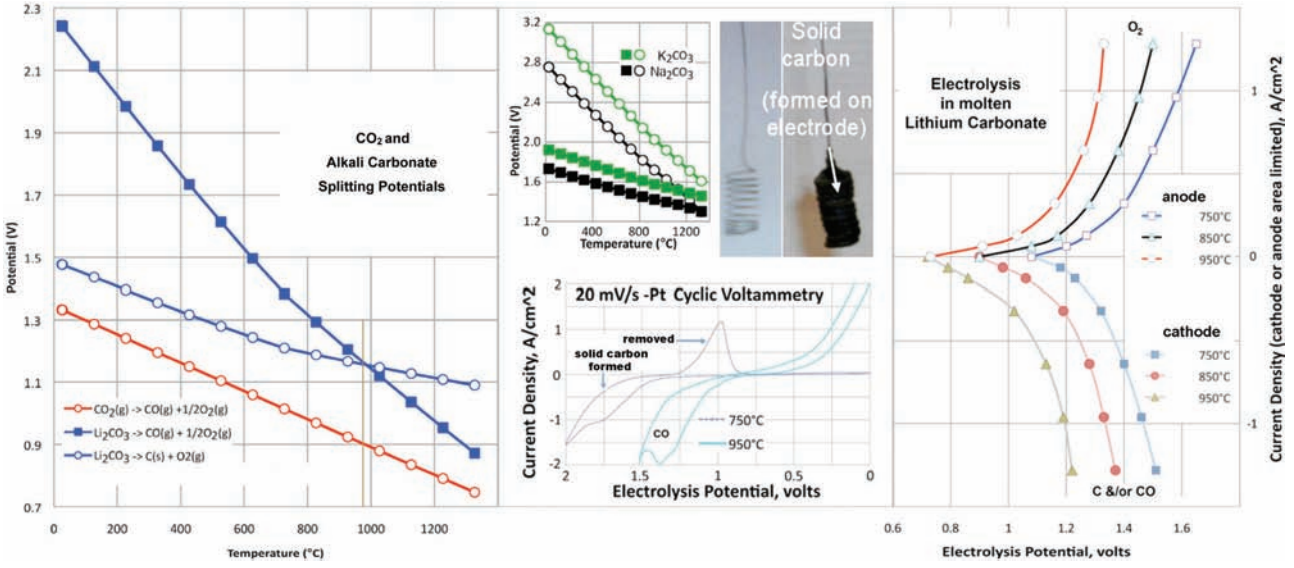

Figure 5. The calculated (left) and measured (right) electrolysis of CO_2 in molten carbonate. Left: The calculated thermodynamic electrolysis potential for carbon capture and conversion in Li_2CO_3 (main figure), or Na_2CO_3 or K_2CO_3 (left middle); squares refer to $M_2CO_3 \rightarrow C + M_2O + O_2$ and circles to a $M_2CO_3 \rightarrow CO + M_2O + 1/2\ O_2$. To the left of the vertical brown line, solid carbon is the thermodynamically preferred (lower energy) product. To the right of the vertical line, CO is preferred. Carbon dioxide fed into the electrolysis chamber is converted to solid carbon in a single step. Photographs: coiled platinum cathode before (left), and after (right), CO_2 splitting to solid carbon at 750 °C in molten carbonate with a Ni anode. Right: The electrolysis full cell potential is measured, under anode or cathode limiting conditions, at a platinum electrode for a range of stable anodic and cathodic current densities in molten Li_2CO_3. Lower midde: cathode size restricted full cell cyclic voltammetry, CV, of Pt electrodes in molten Li_2CO_3. Modified with permission from [4].

(6 S cm^{-1}) than that of Na_2CO_3 (3 S cm^{-1}) or K_2CO_3 (2 S cm^{-1}) near the melting point.[73] Higher conductivity is desired as it leads to lower electrolysis ohmic losses. Low carbonate melting points are achieved by a eutectic mix of alkali carbonates (T_{mp} $Li_{1.07}Na_{0.93}CO_3$: 499 °C; $Li_{0.85}Na_{0.61}K_{0.54}CO_3$: 393°C). Mass transport is also improved at higher temperature; the conductivity increases from 0.9 to 2.1 S cm^{-1} with temperature increase from 650 to 875 °C for a 1:1:1 by mass mixture of the three alkali carbonates.[74]

In 2009 we showed that molten carbonate electrolyzers can provide an effective media for solar splitting of CO_2 at high conversion efficiency. In 2010 Lubormirsky, et al, and our group separately reported that molten lithiated carbonates provide a particularly effective medium for the electrolysis reduction of carbon dioxide.[4,75] As we show in the photograph in Figure 5, at 750 °C, carbon dioxide is captured in molten lithium carbonate electrolyte as solid carbon by reduction at the cathode at low electrolysis potential. It is seen in the cyclic voltammetry, CV, that a solid carbon peak that is observed at 750 °C is not evident at 950 °C. At temperatures less than ~900 °C in the molten electrolyte, solid carbon is the preferred CO_2 splitting product, while carbon monoxide is the preferred product at higher temperature. As seen in the main portion of the figure, the electrolysis potential is <1.2V at either 0.1 or 0.5 A/cm^2, respectively at 750 or 850 °C. Hence, the electrolysis energy required at these elevated, molten temperatures is less than the minimum energy required to split CO_2 to CO at 25 °C:

$$CO_2 \rightarrow CO + 1/2O_2 \quad E^{\circ}(T = 25\,^{\circ}C) = 1.33\ V \tag{15}$$

The observed experimental carbon capture correlates with:

$$Li_2CO_3(molten) \rightarrow C(solid) + Li_2O(dissolved) + O_2(gas) \tag{16A}$$

$$Li_2CO_3(molten) \rightarrow CO(gas) + Li_2O(dissolved) + 1/2O_2(gas) \tag{16B}$$

When CO_2 is bubbled in, a rapid reaction back to the original lithium carbonate is strongly favored:

$$Li_2O(dissolved) + CO_2(gas) \rightarrow Li_2CO_3(molten) \tag{17A}$$

$$Li_2CO_3 \rightarrow Li_2O + CO_2 \tag{17B}$$

In the presence of carbon dioxide, reaction 17A is strongly favored (exothermic), and the rapid reaction back to the original lithium carbonate occurs while CO_2 is bubbled into molten lithium carbonate containing the lithium oxide.

The carbon capture reaction in molten carbonate, combines Equations 16 and 17:

$$CO_2(gas) \rightarrow C(solid) + O_2(gas) T \leq 900\,^{\circ}C \tag{18A}$$

$$CO_2(gas) \rightarrow CO(gas) + 1/2O_2(gas) T \geq 950\,^{\circ}C \tag{18B}$$

The electrolysis of carbon capture in molten carbonates can occur at lower experimental electrolysis potentials than the unit activity potentials calculated in Figure 5. A constant influx of carbon dioxide to the cell maintains a low concentration of Li_2O, in accord with reaction 23. The activity ratio, Θ, of the carbonate reactant to the oxide product in the electrolysis chamber, when high, decreases the cell potentials with the Nernst concentration variation of the potential in accord with Equation 16, as:

$$E_{CO2/X}(T) = E^{\circ}_{CO2/X}(T) - 0.0592\ V \cdot T(K)/(n \cdot 298\ K) \cdot \log(\Theta);$$
$$n = 4 \text{ or } 2, \text{ for } X = C_{solid} \text{ or } CO_{product} \tag{19}$$

For example from Equation 19, the expected cell potential at 950 °C for the reduction to the CO product is $E_{CO2/CO}$ = 1.17 V (0.243/2)·4 = 0.68 V, with a high Θ = 10 000 carbonate/oxide ratio in the electrolysis chamber. As seen in the Figure 5 photo, CO_2 is captured in 750 °C Li_2CO_3 as solid carbon by reduction at the cathode at low electrolysis potential. The carbon formed in the electrolysis in molten Li_2CO_3 at 750 °C is in quantitative accord with the 4 e- reduction of Equation 16A, as determined by (i) mass, at constant 1.25 A for both 0.05 and 0.5 A/cm^2 (large and small electrode) electrolyses (the carbon is washed in a sonicator, and dried at 90 °C), by (ii) ignition (furnace combustion at 950 °C) and by (iii) volumetric analysis in which KIO_3 is added to the carbon, converted to CO_2 and I_2 in hot phosphoric acid ($5C + 4KIO_3 + 4H_3PO_4 \rightarrow 5CO_2 + 2I_2 + 2H_2O + 4KH_2PO_4$), the liberated I_2 is dissolved in 0.05 M KI and titrated with thiosulfate using a starch indicator. We also observe the transition to the carbon monoxide product with increasing temperature. Specifically, while at 750 °C the molar ratio of solid carbon to CO-gas formed is 20:1, at 850° in molten Li_2CO_3, the product ratio is a 2:1, at 900 °C, the ratio is 0.5:1, and at 950 °C the gas is the sole product. Hence, in accord with Figure 2, switching between the C or CO product is temperature programmable.

We have replaced Pt, with Ni, nickel alloys (inconel and monel), Ti and carbon, and each are effective carbon capture cathode materials. Solid carbon deposits on each of these cathodes at similar overpotential in 750 °C molten Li_2CO_3. For the anode, both platinum and nickel are effective, while titanium corrodes under anodic bias in molten Li_2CO_3. As seen in the right side of Figure 5, electrolysis anodic overpotentials in Li_2CO_3 electrolysis are comparable, but larger than cathodic overpotentials, and current densities of over 1A cm^{-2} can be sustained. Unlike other fuel cells, carbonate fuel cells are resistant to poisoning effects,[67] and are effective with a wide range of fuels, and this appears to be the same for the case in the reverse mode (to capture carbon, rather than to generate electricity). Molten Li_2CO_3 remains transparent and sustains stable electrolysis currents after extended (hours/days) carbon capture over a wide range of electrolysis current densities and temperatures.

As delineated in Section 2.3, in practice, either STEP or Hy-STEP modes are useful for efficient solar carbon capture. CO_2 added to the cell is split at 50% solar to chemical energy conversion efficiency by series coupled lithium carbonate electrolysis cells driven at maximum power point by an efficient CPC. Experimentally, we observe the facile reaction of CO_2 and Li_2O in molten Li_2CO_3. We can also calculate the thermodynamic equilibrium conditions between the species in the system, Equation 3B. Using the known thermochemistry of Li_2O, CO_2 and Li_2CO_3,[59b] we calculate the reaction free-energy of Equation 1, and from this calculate the thermodynamic equilibrium constant as a function of temperature. From this equilibrium constant, the area above the curve on the left side of

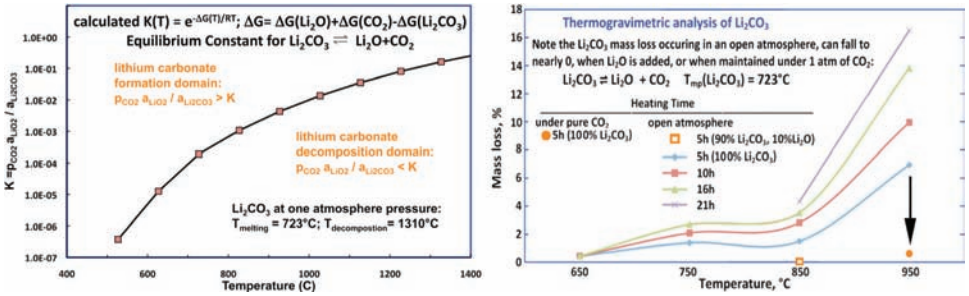

Figure 6. Left: Species stability in the lithium carbonate, lithium oxide, carbon dioxide system, as calculated from Li_2CO_3, Li_2O, and CO_2 thermochemical data. Right: Thermogravimetric analysis of lithium carbonate. The measured mass loss in time of Li_2CO_3. Not shown: The Li_2CO_3 mass loss rate also decreases with an increasing ratio of Li_2CO_3 mass to the surface area of the molten salt exposed to the atmosphere. This increased ratio, may increase the released partial pressure of CO_2 above the surface, increase the rate of the back reaction ($Li_2O + CO_2 \rightarrow Li_2CO_3$), and therefore result in the observed decreased mass loss. Hence, under an open atmosphere at 950 °C, the mass loss after 5 hours falls from 7% to 4.7%, when the starting mass of pure Li_2CO_3 in the crucible is increased from 20 to 50 g. Under these latter conditions (open atmosphere, 950 °C, 50 g total electrolyte), but using a 95% Li_2CO_3, 5% Li_2O mix, the rate of mass loss is only 2.3%. Modified with permission from [8].

Figure 6 presents the wide domain (above the curve) in which Li_2CO_3 dominates, that is where excess CO_2 reacts with Li_2O such that $p_{CO2} \cdot a_{Li2O} < a_{Li2CO3}$. This is experimentally verified when we dissolve Li_2O in molten Li_2CO_3, and inject CO_2(gas). Through the measured mass gain, we observe the rapid reaction to Li_2CO_3. Hence, CO_2 is flowed into a solution of 5% by weight Li_2O in molten Li_2CO_3 at 750 °C, the rate of mass gain is only limited by the flow rate of CO_2 into the cell (using an Omega FMA 5508 mass flow controller) to react one equivalent of CO_2 per dissolved Li_2O. As seen in the measured thermogravimetric analysis on the right side of Figure 6, the mass loss in time is low in lithium carbonate heated in an open atmosphere (~0.03% CO_2) up to 850 °C, but accelerates when heated to 950 °C. However the 950 °C mass loss falls to nearly zero, when heated under pure (1 atm) CO_2. Also in accord with Equation 1 added Li_2O shifts the equilibrium to the left. As seen in the figure in an open atmosphere, there is no mass loss in a 10% Li_2O, 90% Li_2CO_3 at 850 °C, and the Li_2O containing electrolyte absorbs CO_2 (gains mass) at 750 °C to provide for the direct carbon capture of atmospheric CO_2, without a CO_2 pre-concentration stage. This consists of the absorption of atmospheric CO_2 (in molten Li_2CO_3 containing Li_2O, to form Li_2CO_3), combined with a facile rate of CO_2 splitting due to the high carbonate concentration, compared to the atmospheric concentration of CO_2, and the continuity of the steady-state of concentration Li_2O, as Li_2CO_3 is electrolyzed in Equation 16.

3.3. STEP of Iron

A fundamental change in the understanding of iron oxide thermochemistry, can open a facile, new CO_2-free route to iron production. Along with the control of fire, iron production is one of the founding technological pillars of civilization, but is a major source of CO_2 emission. In industry, iron is still produced by the carbothermal greenhouse gas intensive reduction of iron oxide by carbon-coke, and a carbon dioxide free process to form this staple is needed.

The earliest attempt at electrowinning iron (the formation of iron by electrolysis) from carbonate appears to have been in 1944 in the unsuccessful attempt to electrodeposit iron from a sodium carbonate, peroxide, metaborate mix at 450–500 °C, which deposited sodium and magnetite (iron oxide), rather than iron.[76,77] Other attempts[77] have focused on iron electrodepostion from molten mixed halide electrolytes, which has not provided a successful route to form iron,[78,79], or aqueous iron electrowinning[80–83] that is hindered by the high thermodynamic potential (E° = 1.28 V) and diminished kinetics at low temperature.

We present a novel route to generate iron metal by the electrolysis of dissolved iron oxide salts in molten carbonate electrolytes, unexpected due to the reported insolubility of iron oxide in carbonates. We report high solubility of lithiated iron oxides, and facile charge transfer that produces the staple iron at high rate and low electrolysis energy, and can be driven by conventional electrical sources, but is also demonstrated with STEP procesess that decreases or eliminates a major global source of greenhouse gas emission.[3,4]

As recently as 1999, the solubility of ferric oxide, Fe_2O_3, in 650 °C molten carbonate was reported as very low, a $10^{-4.4}$ mole fraction in lithium/potassium carbonate mixtures, and was reported as invariant of the fraction of Li_2CO_3 and K_2CO_3.[84] Low solubility, of interest to the optimization of molten carbonate fuel cells, had likely discouraged research into the electrowinning of iron metal from ferric oxide in molten lithium carbonate. Rather than the prior part per million reported solubility, we find higher Fe(III) solubilities, on the order of 50% in carbonates at 950 °C. The CV of a molten Fe_2O_3 Li_2CO_3 mixture presented in **Figure 7**, and exhibits a reduction peak at –0.8 V, on Pt (gold curve); which is more pronounced at an iron electrode (light gold curve). At constant current, iron is clearly deposited. The cooled deposited product contains pure iron metal and trapped salt, and changes to rust color with exposure to water (figure photo). The net electrolysis is the redox reaction of ferric oxide to iron metal and O_2, Equation 14. The deposit is washed, dried, and is observed to be reflective, grey metallic, responds to an external magnetic field, and consists of dendritic iron crystals.

The two principle natural ores of iron are hematite (Fe_2O_3) and the mixed valence $Fe^{2+/3+}$ magnetite (Fe_3O_4). We observe that, Fe_3O_4 is also highly soluble in molten Li_2CO_3, and may also be reduced to iron with the net electrolysis reaction:

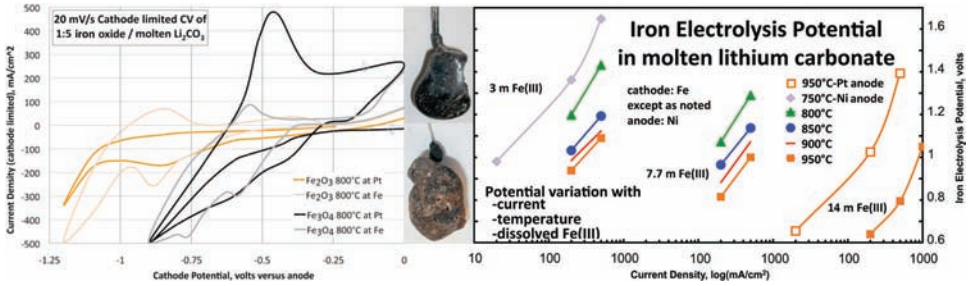

Figure 7. Middle: Photographs of electrolysis products from 20% Fe_2O_3 or Fe_3O_4 by mass in 800°C Li_2CO_3: following extended 0.5A electrolysis at a coiled wire (Pt or Fe) cathode with a Ni anode. Left: cathode restricted CV in Li_2CO_3, containing 1:5 by weight of either Fe_2O_3 or Fe_3O_4. Right: The measured iron electrolysis potentials in molten Li_2CO_3, as a function of the temperature, current density, and the concentration of dissolved Fe(III). Modified with permission from [5].

$$Fe_3O_4 \rightarrow 3Fe + 2O_2 \quad E^{\circ} = 1.32\ V,\ E_{thermoneutral} = 1.45\ V \tag{20}$$

Fe_3O_4 electrolysis potentials run parallel, but ~0.06 V higher, than those of Fe_2O_3 in Figure 1. The processes are each endothermic; the required electrolysis potential decreases with increasing temperature. For Fe_3O_4 in Figure 7, unlike the single peak evident for Fe_2O_3, two reduction peaks appear in the CV at 800 °C. Following the initial cathodic sweep (indicated by the left arrow), the CV exhibits two reduction peaks, again more pronounced at an iron electrode (grey curve), which appear to be consistent with the respective reductions of Fe^{2+} and Fe^{3+}. In either Fe_2O_3, or Fe_3O_4, the reduction occurs at a potential before we observe any reduction of the molten Li_2CO_3 electrolyte, and at constant current, iron is deposited. Following 1 hour of electrolysis at either 200 or 20 mA/cm^2 of iron deposition, as seen in the Figure 7 photographs, and as with the Fe_2O_3 case, the extracted cooled electrode, following extended electrolysis and iron formation, contains trapped electrolyte. Following washing, the product weight is consistent with the eight electron per Fe_3O_4 coulombic reduction to iron.

The solid products of the solid reaction of Fe_2O_3 and Li_2CO_3 had been characterized.[85,86] We prepare and probe the solubility of lithiated iron oxide salts in molten carbonates, and report high Fe(III) solubilities, on the order of 50% in molten carbonates, are achieved via the reaction of Li_2O with Fe_2O_3, yielding an effective method for CO_2 free iron production.

Lithium oxide, as well as Fe_2O_3 or Fe_3O_4, each have melting points above 1460 °C. Li_2O dissolves in 400–1000 °C molten carbonates. We find the solubility of Li_2O in molten Li_2CO_3 increases from 9 to 14 m from 750 to 950 °C. Following preparation of specific iron oxide salts, we add them to molten alkali carbonate. The resultant Fe(III) solubility is similar when either $LiFeO_2$, or $LiFeO_2$ as Fe_2O_3 + Li_2O, is added to the Li_2CO_3. As seen in the left side of **Figure 8**, the solubility of $LiFeO_2$ is over 12 m above 900 °C in Li_2CO_3.

The solid reaction of Fe_2O_3 and Na_2CO_3 produces both $NaFeO_2$ and $NaFe_5O_8$ products.[87] As seen in Figure 8, unlike the high solubility of iron oxide in molten Li_2CO_3, Na_2CO_3 or K_2CO_3, exhibit <<1 wt% iron oxide solubility, even at 950 °C. However, the solubility of (Li_2O + Fe_2O_3) is high in the alkali carbonate eutectic, $Li_{0.87}Na_{0.63}K_{0.50}CO_3$, and is approximately proportional to the Li fraction in the pure Li_2CO_3 electrolyte. The solubility of this lithiated ferric oxide in the $Li_xNa_yK_zCO_3$ mixes provides an alternative molten media for iron production, which compared to pure lithium carbonate, has the disadvantage of lower conductivity,[5] but the advantage of even greater availability, and a wider operating temperature domain range (extending several hundred degrees lower than the pure lithium system).

Fe_2O_3 or $LiFe_5O_8$ dissolves rapidly in molten Li_2CO_3, but reacts with the molten carbonate as evident in a mass loss, which evolves one equivalent of CO_2 per Fe_2O_3, to form a

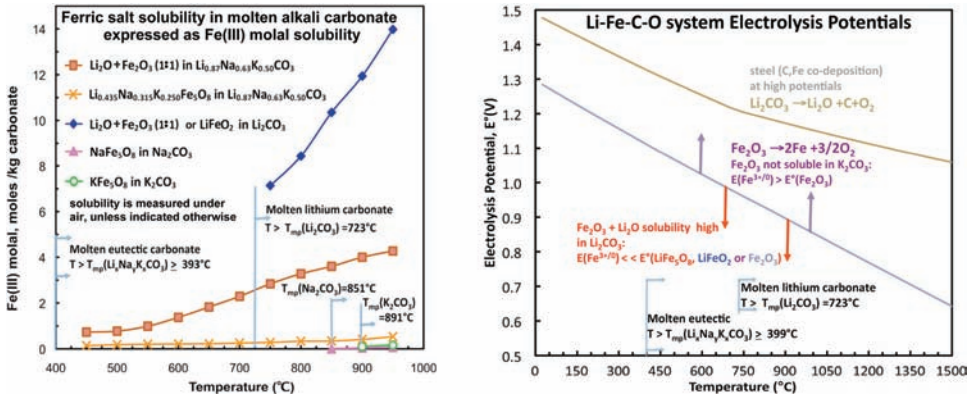

Figure 8. Left: Measured ferric oxides solubilities in alkali molten carbonates. Right: Calculated unit activity electrolysis potentials of $LiFe_5O_8$, Fe_2O_3 or Li_2CO_3. Vertical arrows indicate Nernstian shifts at high or low Fe(III). Modified with permission from [5].

steady state concentration of $LiFeO_2$ in accord with the reaction of Equation 21 (but occurring in molten carbonate).[6] However, 1 equivalent of Li_2O and 1 equivalent of Fe_2O_3, or $LiFeO_2$, dissolves without the reactive formation of CO_2. This is significant for the electrolysis of Fe_2O_3 in molten carbonate. As $LiFeO_2$ is reduced Li_2O is released, Equation 22, facilitating the continued dissolution of Fe_2O_3 without CO_2 release or change in the electrolyte, More concisely, iron production via hematite in Li_2CO_3 is given by I and II:

I dissolution in molten carbonate $Fe_2O_3 + Li_2O \rightarrow 2LiFeO_2$ (21)

II electrolysis, Li_2O regeneration: $2LiFeO_2 \rightarrow 2Fe + Li_2O + 3/2O_2$ (22)

Iron Production, Li_2O unchanged (I + II): $Fe_2O_3 \rightarrow 2Fe + 3/2O_2$ (23)

As indicated in Figure 6, a molar excess, of greater than 1:1 of Li_2O to Fe_2O_3 in molten Li_2CO_3, will further inhibit the Equation 1 disproportionation of lithium carbonate. The right side of Figure 8 summarizes the thermochemical calculated potentials constraining iron production in molten carbonate. Thermodynamically it is seen that at higher potential, steel (iron containing carbon) may be directly formed via the concurrent reduction of CO_2, which we observe in the Li_2CO_3 at higher electrolysis potential, as $Li_2CO_3 \rightarrow C + Li_2O + O_2$, followed by carbonate regeneration via Equation 3, to yield by electrolysis in molten carbonate:

Steel Production: $Fe_2O_3 + 2xCO_2 \rightarrow 2FeC_x + (3/2 + 2x)O_2$ (24)

From the kinetic perspective, a higher concentration of dissolved iron oxide improves mass transport, decreases the cathode overpotential and permits higher steady-state current densities of iron production, and will also substantially decrease the thermodynamic energy needed for the reduction to iron metal. In the electrolyte Fe(III) originates from dissolved ferric oxides, such as $LiFeO_2$ or $LiFe_5O_8$. The potential for the $3e^-$ reduction to iron varies in accord with the general Nerstian expression, for a concentration [Fe(III)], at activity coefficient, α:

$$E_{Fe(III/0)} = E^{\circ}_{Fe(III/0)} + (RT/nF)\log(\alpha_{Fe(III)}[Fe(III)])^{1/3} \quad (25)$$

This decrease in electrolysis potential is accentuated by high temperature and is a ~0.1 V per decade increase in Fe(III) concentration at 950 °C. Higher activity coefficient, $\alpha_{Fe(III)} > 1$, would further decrease the thermodynamic potential to produce iron. The measured electrolysis potential is presented on the right of Figure 7 for dissolved Fe(III) in molten Li_2CO_3, and is low. For example 0.8V sustains a current density of 500 mA cm^{-2} in 14 m Fe(III) in Li_2CO_3 at 950 °C. Higher temperature, and higher concentration, lowers the electrolysis voltage, which can be considerably less than the room potential required to convert Fe_2O_3 to iron and oxygen. When an external source of heat, such as solar thermal, is available then the energy savings over room temperature iron electrolysis are considerable.

Electrolyte stability is regulated through control of the CO_2 pressure and/or by dissolution of excess Li_2O. Electrolyte mass change was measured in 7 m $LiFeO_2$ and 3.5 m Li_2O in molten Li_2CO_3 after 5 hours. Under argon there is a 1, 5, or 7 wt% loss at 750, 850, or 950 °C, respectively), through CO_2 evolution. Little loss occurs under air (0.03% CO_2), while under pure CO_2 the electrolyte gains 2-3 wt% (external CO_2 reacts with dissolved Li_2O to form Li_2CO_3).

The endothermic nature of the new synthesis route, that is the decrease in iron electrolysis potential with increasing temperature, provides a low free energy opportunity for the STEP process. In this process, solar thermal provides heat to decrease the iron electrolysis potential, Figure 7, and solar visible generates electronic charge to drive the electrolysis. A low energy route for the carbon dioxide free formation of iron metal from iron ores is accomplished by the synergistic use of both visible and infrared sunlight. This provides high solar energy conversion efficiencies, Figure 2, when applied to Equations 14 and 20 in a molten carbonate electrolytes. We again use a 37% solar energy conversion efficient concentrator photovoltaic (CPV) as a convenient power source to drive the low electrolysis energy iron deposition without CO_2 formation in Li_2CO_3,[3] as schematically represented in **Figure 9**.

A solar/wind hybrid solar thermal electrochemical production (Hy-STEP) iron electrolysis process is also demonstrated.[6] In lieu of solar electric, electronic energy can be provided by alternative renewables, such as wind. As shown on the right side of Figure 9, in this Hy-STEP example, the electronic energy is driven by a wind turbine and concentrated sunlight is only used to provide heat to decrease the energy required for iron splitting. In this process, sunlight is concentrated to provide effective heating, but is not split into separate spectral regions as in our alternative implementation. Hy-STEP iron production is measured with a 31.5" x 44.5" Fresnel lens (Edmund Optics) which concentrates sunlight to provide temperatures of over 950 °C, and a Sunforce-44444 400 W wind turbine provides electronic charge, charging series nickel metal hydride, MH, cells at 1.5V). Each MH cell, provides a constant discharge potential of 1.0–1.3 V, which are each used to drive one or two series connected iron electrolysis cells as indicated in the right side of Figure 9, containing 14 m Fe(III) molten Li_2CO_3 electrolysis cells. Electrolysis current is included in the lower right of Figure 9. Iron metal is produced. Steel (iron containing carbon) may be directly formed via the concurrent reduction of CO_2, as will be delineated in an expanded study.

3.4. STEP Chlorine and Magnesium Production (Chloride Electrolysis)

The predominant salts in seawater (global average 3.5 ± 0.4% dissolved salt by mass) are NaCl (0.5 M) and $MgCl_2$ (0.05 M). The electrolysis potential for the industrial chlor-alkali reaction exhibits little variation with temperature, and hence the conventional generation of chlorine by electrolysis, Equation 11, would not benefit from the inclusion of solar heating.[3] However, when confined to anhydrous chloride splitting, as exemplified in the lower portion of Figure 1, the calculated potential for the anhydrous electrolysis of chloride salts is endothermic for the electrolyses, which generate a chlorine and metal product. The application of excess heat, as through the STEP process, decreases the energy of electrolysis and can improve the

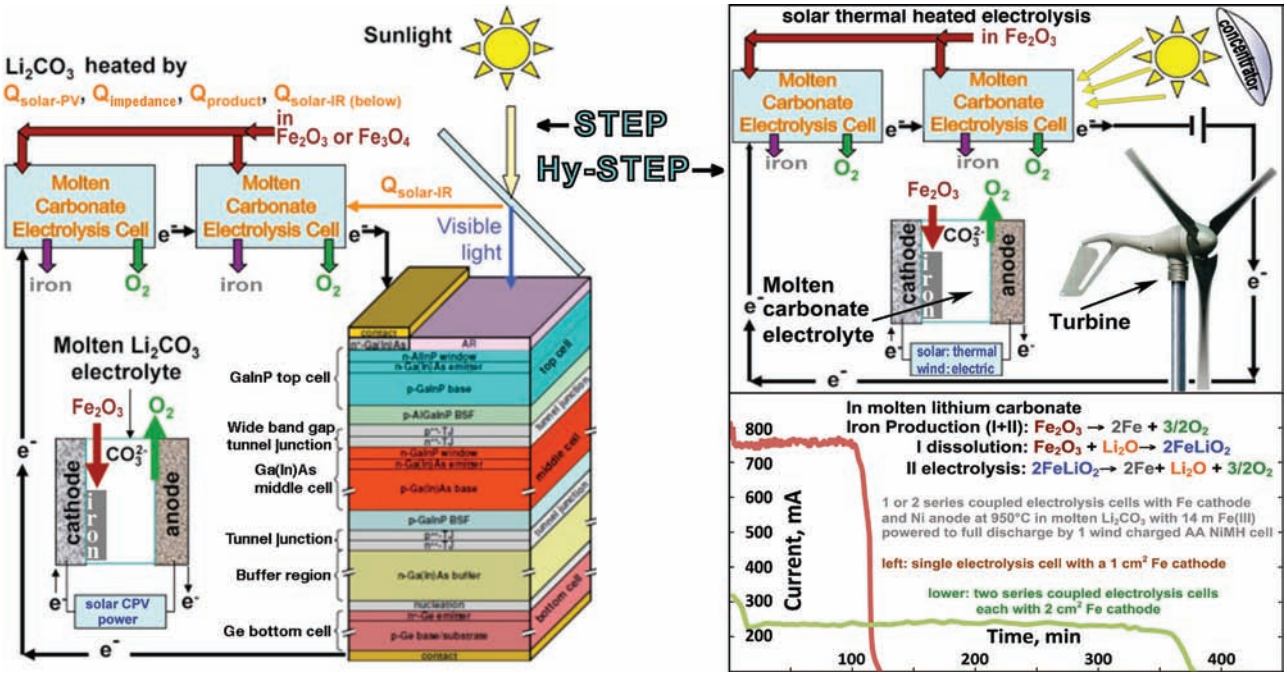

Figure 9. STEP and (wind) Hy-STEP iron. Left: STEP iron production in which two molten carbonate electrolysis in series are driven by a concentrator photovoltaic. The 2.7 V maximum power of the CPV can drive either two 1.35 V iron electrolyses at 800 °C (schematically represented), or three 0.9 V iron electrolyses at 950 °C. At 0.9V, rather than at E°(25 °C) = 1.28V, there is a considerably energy savings, achieved through the application of external heat, including solar thermal, to the system. Right: The Hy-STEP solar thermal/wind production of CO_2 free iron. Concentrated sunlight heats, and wind energy drives electronic transfer into the electrolysis chamber. The required wind powered electrolysis energy is diminished by the high temperature and the high solubility of iron oxide. Bottom: Iron is produced at high current density and low energy at an iron cathode and with a Ni anode in 14 m Fe_2O_3 + 14 m Li_2O dissolved in molten Li_2CO_3. Modified with permission from [6].

kinetics of charge transfer for the equation 12 range of chloride splitting processes. The thermodynamic electrolysis potential for the conversion of NaCl to sodium and chlorine decreases, from 3.24 V at the 801 °C melting point, to 2.99 V at 1027 °C.[3] Experimentally, at 850 °C in molten NaCl, we observe the expected, sustained generation of yellow-green chlorine gas at a platinum anode and of liquid sodium (mp 98 °C) at the cathode. Electrolysis of a second chloride salt, $MgCl_2$, is also of particular interest. The magnesium, as well as the chlorine, electrolysis products are significant societal commodities. Magnesium metal, the third most commonly used metal, is generally produced by the reduction of calcium magnesium carbonates by ferrosilicons at high temperature,[88] which releases substantial levels of carbon dioxide contributing to the anthropogenic greenhouse effect. However, traditionally, magnesium has also been produced by the electrolysis of magnesium chloride, using steel cathodes and graphite anodes, and alternative materials have been invesitgated.[89]

Of significance, here to the STEP process, is the highly endothermic nature of anhydrous chloride electrolysis, such as for $MgCl_2$ electrolysis, in which solar heat will also decrease the energy (voltage) needed for the electrolysis. The rest potential for electrolysis of magnesium chloride decreases from 3.1 V, at room temperature, to 2.5 V at the 714 °C melting point. As seen in **Figure 10**, the calculated thermodynamic potential for the electrolysis of magnesium chloride continues to decrease with increasing temperature, to ~2.3 V at 1000 °C. The 3.1 V energy stored in the magnesium and chlorine room temperature products, when formed at 2.3 V, provide an energy savings of 35%, if sufficient heat applied to the process can sustain this lower formation potential. Figure 10 also includes the experimental decrease in the $MgCl_2$ electrolysis potential with increasing temperature in the lower right portion. In the top portion of the figure, the concurrent shift in the cyclic voltammogram is evident, decreasing the potential peak of magnesium formation, with increasing temperature from 750 °C to 950 °C. Sustained electrolysis and generation of chlorine at the anode and magnesium at the cathode (Figure 10, photo inset) is evident at platinum electrodes. The measured potential during constant current electrolysis at 750 °C in molten $MgCl_2$ at the electrodes is included in the figure.

In the magnesium chloride electrolysis cell, nickel electrodes yield similar results to platinum, and can readily be used to form larger electrodes. The nickel anode sustains extended chlorine evolution without evident deterioration; the nickel cathode may slowly alloy with deposited magnesium. The magnesium product forms both as the solid and liquid (Mg mp 649 °C). The liquid magnesium is less dense than the electrolyte, floats upwards, and eventually needs to be separated and removed to prevent an inter-electrode short, or to prevent a reaction with chlorine that is evolved at the anode. In a scaled up cell configuration (not shown in Figure 10, a larger Ni cathode (200 cm^2 cylindrical nickel sheet (McMaster 9707K35) was employed, sandwiched between two coupled cylindrical Ni sheet anodes

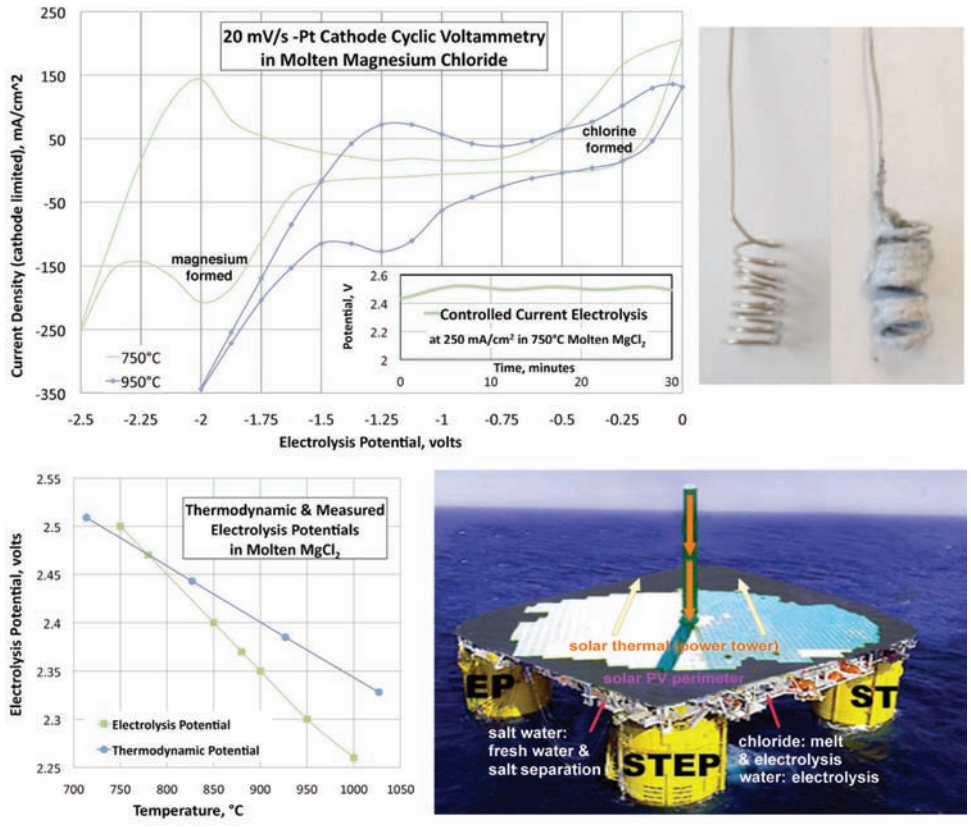

Figure 10. Photograph lower left: coiled platinum before (left), and after (right), $MgCl_2$ electrolysis forming Mg metal on the cathode (shown) and evolving chlorine gas on the anode. Main figure: cathode size restricted cyclic voltammetry of Pt electrodes in molten $MgCl_2$ Inset: The measured full cell potential during constant current electrolysis at 750 °C in molten $MgCl_2$. Lower right: Thermodynamic and measured electrolysis potentials in molten $MgCl_2$ as a function of temperature. Electrolysis potentials are calculated from the thermodynamic free energies components of the reactants and products as $E = -\Delta G(\text{reaction})/2F$. Measured electrolysis potentials are stable values on Pt at 0.250 A/cm^2 cathode.[8] Lower right: A schematic representation of a separate (i) solar thermal and (ii) photovoltaic field to drive both water purification, hydrogen generation, and the endothermic electrolysis of the separated salts to useful products. Modified with permission from [8].

(total 200 cm^2, of area across from the cathode) in a 250 mL alumina (Adavalue) crucible, and sustains multi-ampere currents. The potential at constant current is initially stable, but this cell configuration leads to electrical shorts, unless liquid magnesium is removed.

One salt source for the STEP generation of magnesium and chlorine from $MgCl_2$ are via chlorides extracted from salt water, with the added advantage of the generation of less saline water as a secondary product. In the absence of effective heat exchanger, concentrator photovoltaics heat up to over 100 °C, which decreases cell performance. Heat exchange with the (non-illuminated side of) concentrator photovoltaics can vaporize seawater for desalinization and simultaneously prevent overheating of the CPV. The simple concentrator STEP mode (coupling super-bandgap electronic charge with solar thermal heat) is applicable when sunlight is sufficient to both generate electronic current for electrolysis and sustain the electrolysis temperature. In cases, requiring both the separation of salts from aqueous solution followed by molten electrolysis of the salts, a single source of concentrated sunlight can be insufficient, to both drive water desalinization, and to also heat and drive electrolysis of the molten salts. Figure 10 includes a schematic representation of a Hy-STEP process with separate (i) solar thermal and (ii) photovoltaic field to drive both desalinization and the endothermic carbon dioxide-free electrolysis of the separated salts, or water splitting, to useful products. As illustrated, the separate thermal and electronic sources may each be driven by insolation, or alternatively, can be (i) solar thermal and (ii) (not illustrated) wind, water, nuclear or geothermal driven electronic transfer.

4. STEP Constraints

4.1. STEP Limiting Equations

As illustrated on the left side of Scheme 2, the ideal STEP electrolysis potential incorporates not only the enthalpy needed to heat the reactants to T_{STEP} from $T_{ambient}$, but also the heat recovered via heat exchange of the products with the inflowing reactant. In this derivation it is convenient to describe this combined heat in units of voltage via the conversion factor nF:

$$Q_T \equiv \sum_i H_i(R_i, T_{STEP}) - \sum_i H_i(R_i, T_{ambient}) - \sum_i H_i(C_i, T_{STEP}) + \sum_i H_i(C_i, T_{ambient}); \quad E_Q(V) = -Q_T(J)\,\text{mol})/nF \tag{26}$$

The energy for the process, incorporates E_T, E_Q, and the non-unit activities, via inclusion of Equation 26 into Equation 4, and is termed the STEP potential, E_{STEP}:

$$E_{STEP}(T,a) = [-\Delta G^\circ(T) - Q_T - RT\cdot\ln(\Pi_{i=1\text{ to }x} a(R_i)^{r_i}/\Pi_{i=1\text{ to }y} a(P_i)^{p_i})]/nF;\ E^\circ_{STEP}(a=1) = E^\circ_T + E_Q \tag{27}$$

In a pragmatic electrolysis system, product(s) can be be drawn off at activities that are less than that of the reactant(s). This leads to large activity effects in Equation 27 at higher temperature,[3–6,8,53–55] as the RT/nF potential slope increases with T (e.g., increasing three-fold from 0.0592V/n at 25 °C to 0.183V/n at 650 °C).

The STEP factor, A_{STEP} is the extent of improvement in carrying out a solar driven electrolysis process at T_{STEP}, rather than at $T_{ambient}$. For example, when applying the same solar energy, to electronically drive the electrochemical splitting of a molecule which requires only two thirds the electrolysis potential at a higher temperature, then $A_{STEP} = (2/3)^{-1} = 1.5$. In general, the factor is given by:

$$A_{STEP} = E_{STEP}(T_{ambient}, a)/E_{STEP}(T_{STEP}, a);\ \text{e.g. } T_{ambient} = 298\text{ K} \tag{28}$$

The STEP solar efficiency, η_{STEP}, is constrained by both photovoltaic and electrolysis conversion efficiencies, η_{PV} and $\eta_{electrolysis}$, and the STEP factor. In the operational process, passage of electrolysis current requires an additional, combined (anodic and cathodic) overpotential above the thermodynamic potential; that is $V_{redox} = (1 + z)E_{redox}$, Mobility and kinetics improve at higher temperature and $\xi(T > T_{ambient}) < \xi\ (T_{ambient},)$.[63,67] Hence, a lower limit of $\eta_{STEP}(V_T)$ is given by $\eta_{STEP\text{-}ideal}(E_T)$. At $T_{ambient}$, $A_{STEP} = 1$, yielding $\eta_{STEP}(T_{ambient}) = \eta_{PV}\cdot\eta_{electrolysis}$. η_{STEP} is additionally limited by entropy and black body constraints on maximum solar energy conversion efficiency. Consideration of a black body source emitted at the sun's surface temperature and collected at ambient earth temperature, limits solar conversion to 0.933 when radiative losses are considered,[90] which is further limited to $\eta_{PV} < \eta_{limit} = 0.868$ when the entropy limits of perfect energy conversion are included.[91] These constraints on $\eta_{STEP\text{-}ideal}$ and the maximum value of solar conversion, are imposed to yield the solar chemical conversion efficiency, η_{STEP}:

$$\eta_{STEP-ideal}(T, a) = \eta_{PV}\eta_{electrolysis}A_{STEP}(T, a)$$
$$\eta_{STEP}(T, a) \cong \eta_{PV}\eta_{electrolysis}(T_{ambient}, a)A_{STEP}(T, a);\ (\eta_{STEP} < 0.868) \tag{29}$$

As calculated from Equation 3 and the thermochemical component data[59b] and as presented in Figure 1, the electrochemical driving force for a variety of chemicals of widespread use by society, including aluminium, iron, magnesium and chlorine, significantly decreases with increasing temperature.

4.2. Predicted STEP Efficiencies for Solar Splitting of CO_2

The global community is increasingly aware of the climate consequences of elevated greenhouse gases. A solution to rising carbon dioxide levels is needed, yet carbon dioxide is a highly stable, noncombustible molecule, and its thermodynamic stability makes its activation energy demanding and challenging. The most challenging stage in converting CO_2 to useful products and fuels is the initial activation of CO_2, for which energy is required. It is obvious that using traditional fossil fuels as the energy source would completely defeat the goal of mitigating greenhouse gases. A preferred route is to recycle and reuse the CO_2 and provide a useful carbon resource. We limit the non-unit activity examples of CO_2 mitigation in Equation 15 to the case when CO and O_2 are present as electrolysis products, which yields $a_{O2} = 0.5a_{CO}$, and upon substitution into Equation 27:

$$E_{STEP}(T, a) = E^\circ_{STEP}(T) - (RT/2F)\cdot\ln(N);\ E^\circ(25\,^\circ\text{C}) = 1.333\text{ V};\ N = \sqrt{2}a_{CO_2}a_{CO}^{-3/2} \tag{30}$$

The example of $E_{STEP}(T,a\neq1)$ on the left side of **Figure 11** is derived when N = 100, and results in a substantial drop in the energy to split CO_2 due to the discussed influence of RT/2F. Note at high temperature conditions in the figure, $E_{STEP} < 0$ occurs, denoting the state in which the reactants are spontaneously formed (without an applied potential). This could lead to the direct thermochemical generation of products, but imposes substantial experimental challenges. To date, analogous direct water splitting attempts, are highly inefficient due to the twin challenges of high temperature material constraints and the difficulty in product separation to prevent back reaction upon cooling.[92] The STEP process avoids this back reaction through the separation of products, which spontaneously occurs in the electrochemical, rather than chemical, generation of products at separate anode and cathode electrodes.

The differential heat required for CO_2 splitting, E_Q, and the potential at unit activity, E°_{STEP}, are calculated and presented in the top of Figure 11. E_Q has also been calculated and is included. E_Q is small (comprising tens of millivolts or less) over the entire temperature range. Hence from Equation 27, E°_{STEP} does not differ significantly from the values presented for E_T° for CO_2 in Figure 2. ECO_2split (25 °C) yields $A_{STEP}(T) = 1.333V/E^\circ_{STEP}(T)$ with unit activity, and $A_{STEP}(T) = 1.197V/E_{STEP}(T)$ for the $N = 100$ case. Large resultant STEP factors are evident in the left of Figure 11. This generates substantial values of solar to chemical energy conversion efficiency for the STEP CO_2 splitting to CO and O_2.

A STEP process operating in the $\eta_{PV}\cdot\eta_{electrolysis}$ range of 0.20 to 0.40 includes the range of contemporary 25% to 45% efficient concentrator photovoltaics,[69] and electrolysis efficiency range of 80% to 90%. From these, the CO_2 solar splitting efficiencies are derived from Equations 29 and 30, and are summarized on the right side of Figure 11. The small values of $E_{STEP}(T)$ at higher T, generate large STEP factors, and result in high solar to chemical energy conversion efficiencies for the splitting of CO_2 to CO and O_2. As one intermediate example from Equation 30, we take the case of an electrolysis efficiency of 80% and a 34% efficient photovoltaic ($\eta_{PV}\cdot\eta_{electrolysis} = 0.272$). This will drive STEP solar CO_2 splitting at molten carbonate temperatures (650 °C)

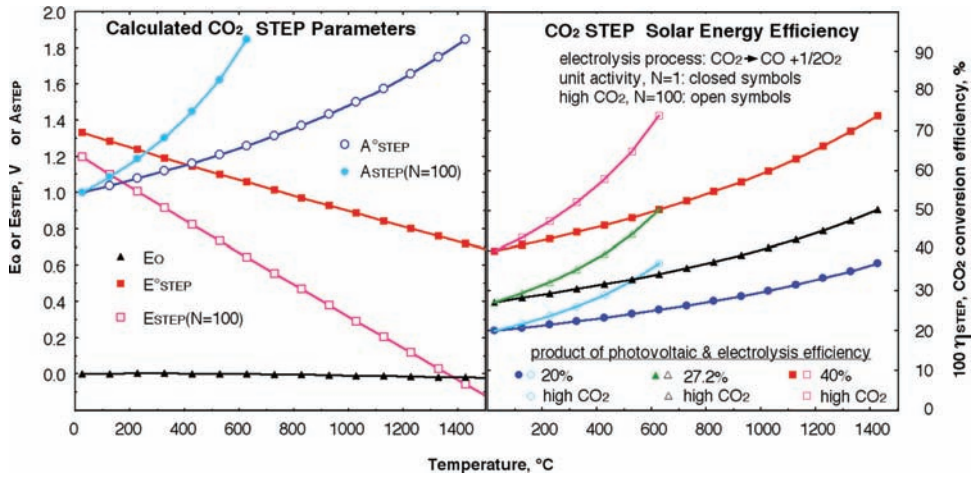

Figure 11. Top: Calculated STEP parameters for the solar conversion of CO_2. Bottom: Solar to chemical conversion efficiencies calculated through Equation 29 for the conversion of CO_2 to CO and O_2. In the case in which the product of the photovoltaic and electrolysis efficiency is 27.2% ($\eta_{PV} \cdot \eta_{electrolysis}$ = 0.272), the STEP conversion efficiency at unit activity is 35%, at the 650 °C temperature consistent with molten carbonate electrolysis, rising to 40% at the temperature consistent with solid oxide electrolysis (1000 °C). Non-unit activity calculations presented are for the case of $\sqrt{2}\ a_{CO2}\ a_{CO}^{-3/2} = 100$. A solar conversion efficiency of 50% is seen at 650 °C when N = 100 (the case of a cell with 1 bar of CO_2 and ~58 mbar CO). Modified with permission from [3].

at a solar conversion efficiency of 35% in the unit activity case, and at 50% when N = 100 (the case of a cell with 1 bar of CO_2 and ~58 mbar CO).

4.3. Scalability of STEP Processes

STEP can be used to remove and convert carbon dioxide. As with water splitting, the electrolysis potential required for CO_2 splitting falls rapidly with increasing temperature (Figure 1), and we have shown here (Figure 2) that a photovoltaic, converting solar to electronic energy at 37% efficiency and 2.7 V, may be used to drive three CO_2 splitting, lithium carbonate electrolysis cells, each operating at 0.9 V, and each generating a 2 electron CO product. The energy of the CO product is 1.3V (Equation 1), even though generated by electrolysis at only 0.9V due to synergistic use of solar thermal energy. As seen in Figure 5, at lower temperature (750 °C, rather than 950 °C), carbon, rather than CO, is the preferred product, and this 4 electron reduction approaches 100% Faradaic efficiency.

The CO_2 STEP process consists of solar driven and solar thermal assisted CO_2 electrolysis. Industrial environments provide opportunities to further enhance efficiencies; for example fossil-fueled burner exhaust provides a source of relatively concentrated, hot CO_2. The product carbon may be stored or used, and the higher temperature product carbon monoxide can be used to form a myriad of industrially relevant products including conversion to hydrocarbon fuels with hydrogen (which is generated by STEP water splitting in Section 3.1), such as smaller alkanes, dimethyl ether, or the Fischer Tropsch generated middle-distillate range fuels of C11-C18 hydrocarbons including synthetic jet, kerosene and diesel fuels.[93] Both STEP and Hy-STEP represent new solar energy conversion processes to produce energetic molecules. Individual components used in the process are rapidly maturing technologies including wind electric,[94] molten carbonate fuel cells,[67] and solar thermal technologies.[95–100]

It is of interest whether material resources are sufficient to expand the process to substantially impact (decrease) atmospheric levels of carbon dioxide. The buildup of atmospheric CO_2 levels from a 280 to 392 ppm occurring over the industrial revolution comprises an increase of 1.9×10^{16} mole (8.2×10^{11} metric tons) of CO_2,[101] and will take a comparable effort to remove. It would be preferable if this effort results in usable, rather than sequestered, resources. We calculate below a scaled up STEP capture process can remove and convert all excess atmospheric CO_2 to carbon.

In STEP, 6 kWh m^{-2} of sunlight per day, at 500 suns on 1 m^2 of 38% efficient CPV, will generate 420 kAh at 2.7 V to drive three series connected molten carbonate electrolysis cells to CO, or two series connected series connected molten carbonate electrolysis cells to form solid carbon. This will capture 7.8×10^3 moles of CO_2 day^{-1} to form solid carbon (based on 420 kAh·2 series cells/ 4 Faraday mol^{-1} CO_2). The CO_2 consumed per day is three fold higher to form the carbon monoxide product (based on 3 series cells and 2 F mol^{-1} CO_2) in lieu of solid carbon. The material resources to decrease atmospheric carbon dioxide concentrations with STEP carbon capture, appear to be reasonable. From the daily conversion rate of 7.8×10^3 moles of CO_2 per square meter of CPV, the capture process, scaled to 700 km^2 of CPV operating for 10 years can remove and convert all the increase of 1.9×10^{16} mole of atmospheric CO_2 to solid carbon. A larger current density at the electrolysis electrodes, will increase the required voltage and would increase the required area of CPVs. While the STEP product (chemicals, rather than electricity) is different than contemporary concentrated solar power (CSP) systems, components including a tracker for effective solar concentration are similar (although an electrochemical reactor, replaces the mechanical turbine). A variety of CSP installations, which include molten salt heat

storage, are being commercialized, and costs are decreasing. STEP provides higher solar energy conversion efficiencies than CSP, and secondary losses can be lower (for example, there are no grid-related transmission losses). Contemporary concentrators, such as based on plastic Fresnel or flat mirror technologies, are relatively inexpensive, but may become a growing fraction of cost as concentration increases.[100] A greater degree of solar concentration, for example 2000 suns, rather than 500 suns, will proportionally decrease the quantity of required CPV to 175 km^2, while the concentrator area will remain the same at 350 000 km^2, equivalent to 4% of the area of the Sahara desert (which averages ~6 kWh m^{-2} of sunlight per day), to remove anthropogenic carbon dioxide in ten years.

A related resource question is whether there is sufficient lithium carbonate, as an electrolyte of choice for the STEP carbon capture process, to decrease atmospheric levels of carbon dioxide. 700 km^2 of CPV plant will generate 5×10^{13} A of electrolysis current, and require ~2 million metric tonnes of lithium carbonate, as calculated from a 2 kg/l density of lithium carbonate, and assuming that improved, rather than flat, morphology electrodes will operate at 5 A/cm^2 (1000 km^2) in a cell of 1 mm thick. Thicker, or lower current density, cells will require proportionally more lithium carbonate. Fifty, rather than ten, years to return the atmosphere to pre-industrial carbon dioxide levels will require proportionally less lithium carbonate. These values are viable within the current production of lithium carbonate. Lithium carbonate availability as a global resource has been under recent scrutiny to meet the growing lithium battery market. It has been estimated that the current global annual production of 0.13 million tonnes of LCE (lithium carbonate equivalents) will increase to 0.24 million tonnes by 2015.[102] Potassium carbonate is substantially more available, but as noted in the main portion of the paper can require higher carbon capture electrolysis potentials than lithium carbonate.

5. Conclusions

To mitigate the consequences of rising atmospheric carbon dioxide levels and its effect on global climate change, there is a drive to replace conventional fossil fuel driven electrical production by renewable energy driven electrical production. In addition to the replacement of the fossil fuel economy by a renewable electrical economy, we suggest that a renewable chemical economy is also warranted. Solar energy can efficiently ube sed, as demonstrated with the STEP process, to form the chemicals needed by society without carbon dioxide emission directly and efficiently. Iron, a basic commodity, currently accounts for the release of one quarter of worldwide CO_2 emissions by industry, which may be eliminated by replacement with the STEP iron process. The unexpected solubility of iron oxides in lithium carbonate electrolytes, coupled with facile charge transfer and a sharp decrease in iron electrolysis potentials with increasing temperature, provides a new route for iron production. Iron is formed without an extensive release of CO_2 in a process compatible with the predominant naturally occurring iron oxide ores, hematite, Fe_2O_3, and magnetite, Fe_3O_4. STEP can also be used in direct carbon capture, and the efficient solar generation of hydrogen and other fuels.

In addition to the removal of CO_2, the STEP process is shown to be consistent with efficient solar generation from a variety of metals, as well as chlorine via endothermic electrolyses. Commodity production and fuel consumption processes are responsible for the majority of industry based CO_2 release, and their replacement by STEP processes provides a path to end the root cause of anthropogenic global warming, as a transition beyond the fossil fuel, electrical, or hydrogen economy, to a renewable chemical economy based on the direct formulation of the materials needed by society. An expanded understanding of electrocatalysis and materials will advance the efficient electrolysis of STEP's growing portfolio of energetic products.

Acknowledgements

The author is grateful to Baouhui Wang and Hongun Wu for excellent experimental contributions to references 4 and 5.

Received: August 18, 2011
Revised: September 13, 2011
Published online:

[1] *On Solar Hydrogen & Nanotechnology*, (Ed: L. Vayssieres), John Wiley and Sons, Weinheim, Germany **2009**.
[2] *The Solar Generation of Hydrogen: Towards a Renewable Energy Future* (Eds: K. Rajeshwar, S. Licht, R. McConnell), Springer, New York, USA **2008**.
[3] S. Licht, *J. Phys. Chem. C* **2009**, *113*, 16283.
[4] S. Licht, B. Wang, S. Ghosh, H. Ayub, D. Jiang, J. Ganely, *J. Phys. Chem. Lett.* **2010**, *1*, 2363.
[5] S. Licht, B. Wang, *Chem. Commun.* **2010**, *46*, 7004.
[6] S. Licht, H. Wu, Z. Zhang, H. Ayub, *Chem. Commun.* **2011**, *47*, 3081.
[7] S. Licht, O. Chityat, H Bergmann, A. Dick, S. Ghosh, H. Ayub, *Int. J. Hyd. Energy* **2010**, *35*, 10867.
[8] S. Licht, B. Wang, H. Wu, *J. Phys. Chem. C* **2011**, *115*, 11803.
[9] G. Ohla, P. Surya, S. Licht, N. Jackson, *Reversing Global Warming: Chemical Recycling and Utilization of CO_2.* Report of the National Science Foundation sponsored 7-2008 Workshop, 17 pages **2009**; full report available at: http://www.usc.edu/dept/chemistry/loker/ReversingGlobalWarming.pdf
[10] C. Graves, S. Ebbsen, M. Mogensen, K. Lackner, *Renewable Sustainble Energy Rev.* **2011**, *15*, 1.
[11] J. Barber, *Chem. Soc. Rev.* **2009**, *38*, 185.
[12] A. Stamatiou, P. G. Loutzenhiser, A. Steinfeld, *Energy Fuels* **2010**, *24*, 2716.
[13] S. Abanades, M. Chambon, *Energy Fuels* **2010**, *24*, 6677.
[14] L. J. Venstrom, J. H. Davidson, *J. Solar Energy Eng. Chem.* **2010**, *133*, 011017–011021.
[15] W. Chueh, S. Haile, *Phil. Trans. Roy. Soc. A* **2010**, *368*, 3269.
[16] J. Miller, M. Allendorf, R. Diver, L. Evans, N. Siegel, J. Stueker, *J. Mater. Sci.* **2008**, *43*, 4714.
[17] S. Licht, *Nature* **1987**, *330*, 148.
[18] S. Licht, D. Peramunage, *Nature* **1990**, *345*, 330.
[19] B. Oregan, M. Gratzel, *Nature* **1991**, *353*, 737.
[20] S. Licht, *J. Phys. Chem.* **1998**, *90*, 1096.
[21] *Semiconductor Electrodes and Photoelectrochemistry*, (Ed: S. Licht), Wiley-VCH, Weinheim, Germany **2002**.
[22] S. Licht, G. Hodes, R. Tenne, J. Manassen, *Nature* **1987**, *326*, 863.
[23] S. Licht, B. Wang, T. Soga, M. Umeno, *Appl. Phys. Lett.* **1999**, *74*, 4055.
[24] S. Yan, L. Wan, Z. Li, Z. Zou, *Chem. Commun.* **2011**, *47*, 5632.

[25] H. Zhou, T. Fan, D. Zhang, *ChemCatChem* **2011**, *3*, 513.
[26] R. Huchinson, E. Holland, B. Carpenter, *Nat. Chem.* **2011**, *3*, 301.
[27] E. E. Barton, D. M. Rampulla, A. B. Bocarsly, *J. Am. Chem. Soc.* **2008**, *130*, 6342.
[28] S. Kaneco, H. Katsumata, T. Suzuki, K. Ohta, *Chem Eng. J.* **2006**, *92*, 363.
[29] P. Pan, Y. Chen, *Catal. Commun.* **2007**, *8*, 1546.
[30] A. B. Murphy, *Solar Energy Mater.* **2008**, *116*, 227.
[31] A. Currao, *Chimia* **2007**, *61*, 815.
[32] a) S. R. Narayanan, B. Haines, J. Soler, T. I. Valdez, *J. Electrochem. Soc.* **2011**, *158*, A167; b) C. Delacourt, J. Newman, *J. Electrochem. Soc.* **2010**, *157*, B1911.
[33] E. Dufek, T. Lister, M. McIlwain, *J. Appl. Electrochem.* **2011**, *41*, 623.
[34] M. Gangeri, S. Perathoner, S. Caudo, G. Centi, J. Amadou, D. Begin, C. Pham-Huu, M. Ledoux, J. Tessonnier, D. Su, R. Schlogl, *Catalysis Today* **2009**, *143*, 4714.
[35] B. Innocent, D. Liaigre, D. Pasquier, F. Ropital, J. Leger, K. Kokoh, *J. Appl. Electrochem.* **2009**, *39*, 227.
[36] A. Wang, W. Liu, S. Cheng, D. Xing, J. Zhou, B. Logan, *Int. J. Hydrogen Energy* **2009**, *39*, 3653.
[37] N. Dong-fang, X. Cheng-tian, L. Yi-wen, Z. Li, L. Jiz-xing, *Chem. Res. Chinese U.* **2009**, *34*, 708.
[38] D. Chu, G. Qin, X. Yuan, M. Xu, P. Zheng, J. Lu, *ChemSusChem* **2008**, *1*, 205.
[39] J. Yano, T. Morita, K. Shimano, Y. Nanmi, S. Yamsaki, *J. Sol. State Electrochem.* **2007**, *11*, 554.
[40] Y. Hori, H. Konishi, T. Futamura, A. Murata, O. Koga, H. Sakuri, K. Oguma, *Electrochim. Acta* **2005**, *50*, 5354.
[41] K. Ogura, H. Yano, T. Tanaka, *Catalysis Today* **2004**, *98*, 414.
[42] a) H. Chandler, F. Pollara, *AICHE Chem. Eng. Prog. Ser.: Aerospace Life Support* **1966**, *62*, 38; b) L. Elikan, D. Archer, R. Zahradnik, *ibid* 28.
[43] a) M. Stancati, J. Niehoff, W. Wells, R. Ash, *AIAA* **1979**, *79-0906*, 262; b) R. Richter, *ibid* **1981**, *82-2275*, 1.
[44] a) J. Mizusaki, H. Tagawa, Y. Miyaki, S. Yamauchi, K. Fueki, I. Koshiro, *Solid State Ionics* **1992**, *126*, 53; b) G. Tao, K. Sridhar, C. Chan, *ibid* **2004**, *175*, 615; c) R. Green, C. Liu, S. Adler, *ibid* 621; d) *ibid* **2008**, *179*, 647.
[45] C. Meyers, N. Sullivan, H. Zhu, R. Kee, *J. Electrochem. Soc.* **2011**, *158*, B117.
[46] P. Kim-Lohsoontorn, N. Laosiripojana, J. Bae, *Current Appl. Phys.* **2011**, *11*, 5223.
[47] S. Ebbesen, C. Graves, A. Hausch, S. Jensen, M. Mogensen, *J. Electrochem. Soc.* **2010**, *157*, B1419.
[48] S. Jensen, X. Sun, S. Ebbesen, R. Knibbe, M. Mogensen, *Int. J. Hydrogen Energy* **2010**, *35*, 9544.
[49] Q. Fu, C. Mabilat, M. Zahid, A. Brisse, L. Gautier, *Energy Environ. Sci.* **2010**, *3*, 1382.
[50] C. M. Stoots, J. E. O'Brien, K. G. Condie, J. Hartvigsen, *Int. J. Hydrogen Energy* **2010**, *35*, 4861.
[51] Q. Fu, C. Mabilat, M. Zahid, A. Brisse, L. Gautier, *Energy Environ. Sci.* **2010**, *3*, 1382.
[52] D. Lueck, W. Buttner, J. Surma, *Fluid System Technologies* **2002**, at:http://rtreport.ksc.nasa.gov/techreports/2002report/600%20Fluid%20Systems/609.html.
[53] S. Licht, *Electrochem. Commun.* **2002**, *4*, 789.
[54] S. Licht, *J. Phys. Chem. B* **2003**, *107*, 4253.
[55] S. Licht, L. Halperin, M. Kalina, M. Zidman, N. Halperin, *Chem. Commun.* **2003**, *2003*, 3006; S. Licht, *Chem. Commun.* **2005**, *2005*, 4623.
[56] A. Fujishima, K. Honda, *Nature* **1972**, *238*, 37.
[57] Z. Zou, Y. Ye, K. Sayama, H. Arakawa, *Nature* **2001**, *414*, 625.
[58] a) S. Licht, B. Wang, S. Mukerji, T. Soga, M. Umento, H. Tributsh, *J. Phys. Chem. B* **2000**, *104*, 8920; b) S. Licht, *J. Phys. Chem. B* **2001**, *105*, 6281.
[59] a) A. J. deBethune, T. S. Licht, *J. Electrochem. Soc.* **1959**, *106*, 616; b) M. W. Chase, *J. Phys. Chem. Ref. Data* **1998**, *9*, 1; data available at: http://webbook.nist.gov/chemistry/form-ser.html
[60] W. E. Wentworth, E. Chen, *Solar Energy* **1976**, *18*, 205.
[61] J. O'M. Bockris, *Energy Options*, Halsted Press, NY **1980**.
[62] T. S. Light, S. Licht, A. C. Bevilacqua, *Electrochem. Solid State Lett.* **2005**, *8*, E16.
[63] T. S. Light, S. Licht, *Anal. Chem.* **1987**, *59*, 2327.
[64] S. Licht, *Anal. Chem.* **1985**, *57*, 514.
[65] S. Licht, K. Longo, D. Peramunage, F. Forouzan, *J. Electroanal. Chem.* **1991**, *318*, 119.
[66] C. Elschenbroich, A. Salzer*Organometallics*. 2nd Ed., Wiley-VCH, Weinheim,) Germany **1992**.
[67] K. Sunmacher, *Molten Carbonate Fuel Cells*, Wiley-VCH, Weinheim, Germany **2007**.
[68] J. L. Pellegrino, *Energy & Environmental Profile of the U.S. Chemical Industry* **2000**, available online at: http://www1.eere.energy.gov/industry/chemicals/tools_profile.html
[69] a) R. R. King, D. C. Law, K. M. Edmonson, C. M. Fetzer, G. S. Kinsey, H. Yoon, R. A. Sherif, N. H. Karam, *Appl. Phys. Lett.* **2007**, *90*, 183516; b) M. Green, K. Emery, Y. Hishikawa, W. Warata, *Prog. Photovoltaics* **2011**, *19*, 84.
[70] J. E. Miller, M. D. Allendorf, R. B. Diver, L. R. Evans, N. P. Siegel, J. N. Stuecker, *J. Mater. Sci.* **2008**, *43*, 4714.
[71] Y. Woolerton, Y. W. Sheard, S. Reisner, E. Pierce, S. W. Ragsdale, F. A. Armstrong, *J. Am. Chem. Soc.* **2010**, *132*, 2132.
[72] E. Benson, C. P. Kubiak, A. J Sathrum, J. M. N. Smieja, *Chem. Soc. Rev.* **2009**, *38*, 89.
[73] *Principles and Applications of Molten Salt Electrochemistry*, (Eds: Z. Zhang, Z. Wang) Chemical Industry Press, Beijing **2006**, p. 191.
[74] T. Kojima, Y. Miyazaki, K. Nomura, K. Tanimoto, K. Density, *J. Electrochem. Soc.* **2008**, *155*, F150.
[75] V. Kaplan, E. Wachtel, K. Gartsman, Y. Feldman, I. Lubormirsky, *J. Electrochem. Soc.* **2010**, *157*, B552.
[76] L. Andrieux, G. Weiss, *Comptes Rendu* **1944**, *217*, 615.
[77] G. M. Haarberg, E. Kvalheim, S. Rolseth, T. Murakami, S. Pietrzyk, S. Wang, *ECS Transactions* **2007**, *3*, 341.
[78] S. Wang, G. M. Haarberg, E. Kvalheim, *J. Iron Res. Int.* **2008**, *15*, 48.
[79] G. M. Li, D. H. Wang, Z. Chen, *J. Mater. Sci. Tech.* **2009**, *25*, 767.
[80] B. Y. Yuan, O. E. Kongstein, G. M. Haarberg, *J. Electrochem. Soc.* **2009**, *156*, D64.
[81] W. Palmaer, J. A. Brinell, *Chem. Metall. Eng.* **1913**, *11*, 197.
[82] F. A. Eustis, *Chem. Metall. Eng.* **1922**, *27*, 684.
[83] E. Mostad, S. Rolseth, S. Thonstad, *J. Hydrometallurgy* **2008**, *90*, 213.
[84] L. Qingeng, F. Borum, I. Petrushina, N. J. Bjerrum, *J. Electrochem, Soc.* **1999**, *146*, 2449.
[85] R. Collongues, G. Chaudron, *Compt. Rend.* **1950**, *124*, 143.
[86] A. Wijayasinghe, B. Bergman, C. Lagergren, *J. Electrochem. Soc.* **2003**, *150*, A558.
[87] A. Lykasov, M. Pavlovskaya, *Inorg. Mater.* **2003**, *39*, 1088.
[88] H. Q. Li, S. S. Xie, *J. Rare Earths* **2005**, *23*, 606.
[89] G. Demirci, I. Karakaya, *J. Alloys Compd.* **2008**, *465*, 255.
[90] C. S. Solanki, G. Beaucarne, *Advanced Solar Cell Concepts*, AER India-2006, **2006**, 256.
[91] A. Luque, A. Marti, *Handbook of Photovoltaic Sci. & Eng.*, (Eds. A. Luque, S. Haegedus), Wiley-VCH, Weinheim, Germany **2003**, 113.
[92] A. Kogan, *Int. J. Hydrogen Energy* **1998**, *23*, 89.
[93] A. Andrews, J. Logan, Fischer-Tropsch Fuels from Coal, Natural Gas, and Biomass: Background and Policy. *Congressional Research Service Report for Congress* **2008**, RL34133, (March 27, 2008); available at: http://assets.opencrs.com/rpts/RL34133_20080327.pdf.
[94] E. Barbier, *Nature* **2010**, *464*, 832.

[95] Power tower solar technologies are described at: brightsourceenergy.com; ausra.com, esolar.com; bengoasolar.com/corp/web/en/our_projects/solana/.
[96] Siemens to build molten salt solar thermal test facility in Portugal, siemens.com, **2011**, at: http://www.siemens.com/press/pool/de/pressemitteilungen/2011/renewable_energy/ERE201102037e.pdf.
[97] See: solarreserve.com, **2011**, at: http://www.solarreserve.com/projects.html.
[98] Parabolic solar concentrator technologies are described at: stirlingenergy.com.
[99] Fresnel solar concentrator technologies are described at: amonix.com, energy innovations.com/sunflower.
[100] R. Pitz-Paal, in *Solar Energy Conversion and Photoenergy Systems*, (Eds. J. B. Galvez, S. M. Rodriguez) EOLSS Publishers, Oxford, UK **2007**.
[101] P. Tans, An accounting of the observed increase in oceanic and atmospheric CO_2 and an outlook for the future. *Oceanography* **2009**, *22*, 26.
[102] W. Tahil, "*The Trouble with Lithium 2; Under the Microscope*", Meridan International Research, Martainsville, France, **2008**, 54.

nature

INTERNATIONAL WEEKLY JOURNAL OF SCIENCE

Volume 330 No.6144 12-18 November 1987 £1.95

PHOTOELECTROCHEMICAL SOLAR CELLS

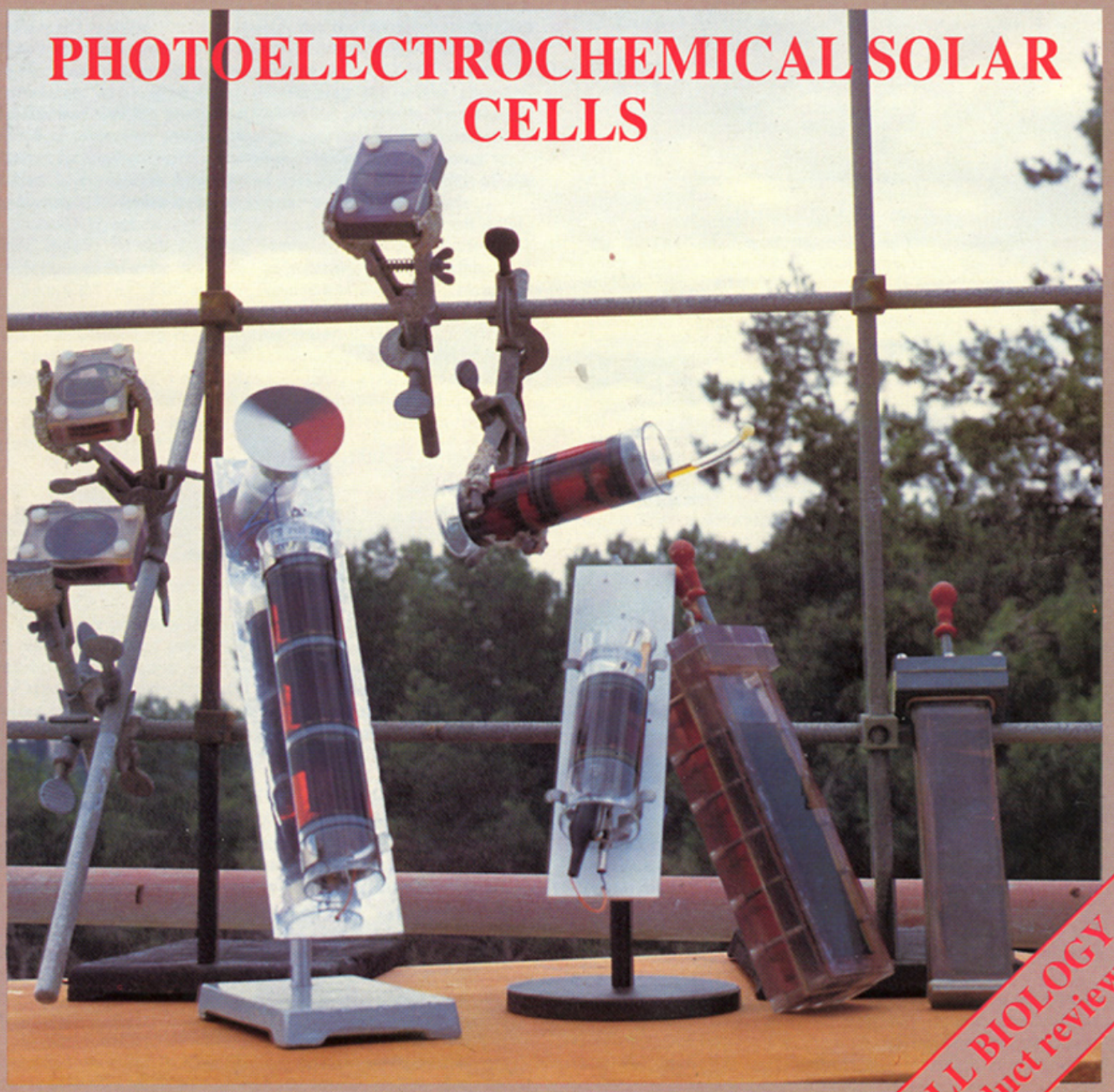

CELL BIOLOGY
Product review

Cover Article: "A Description of Energy Conversion in Photoelectrochemical Solar Cells" by Stuart Licht

nature
12 November 1987
Vol. 330 Issue no. 6144

A variety of liquid solar cells operating from a roof-top laboratory. Each cell contains an aqueous polysulphide electrolyte and an *n*-cadmium chalcogenide semiconductor. The chemical mechanism of energy conversion in these cells is described on page 148.

A description of energy conversion in photoelectrochemical solar cells

Stuart Licht*

Department of Materials Research, The Weizmann Institute of Science, Rehovot 76100, Israel

Photoelectrochemical cells (PECs) provide alternatives to conventional solid-state solar cells. Since the discovery in 1976, the *n*-cadmium chalcogenide/aqueous polysulphide photoelectrochemical cell, *n*-CdX/S_j^{2-} PEC, has been the most studied and in some ways the most promising of these liquid solar cells[1,2], and can combine photoelectrochemical conversion with electrochemical storage[3] in a system competitive in overall efficiency with the best comparable solid-state systems. But despite hundreds of studies, neither the reactive chemical species nor the chemical mechanism of operation is known. Here a complete description of the radiative to electrical energy conversion process in *n*-CdX/S_j^{2-} systems is introduced, accomplished by determining the active chemical species and limiting photoelectrochemical processes. Two distinct chemical processes control energy conversion. Photocurrent is limited by supersulphide adsorption. Maximum photopower utilization is desorption limited and related to the activity of the hydrosulphide, hydroxide and shorter polysulphide species.

Photoelectrochemical studies have often focused on solid-state aspects of the systems, accessing available models for analogous solid-state devices. The polysulphide electrolyte used in the *n*-CdX/S_j^{2-} PEC system, formed by the simple dissolution of a sulphide salt and sulphur in water, is known to be highly complex, containing H^+ and other cations[4], OH^-, H_2S, S^{2-}, the polysulphides (S_j^{2-} ($j = 2$ to 5)) (refs 5,6), supersulphide[7] (S_2^-), thiosulphate ($S_2O_3^{2-}$) and sulphate[6] (SO_4^{2-}). As a result of this complexity the overall mechanism of photoinduced oxidation in the *n*-CdX/S_j^{2-} system has remained unknown, but was generally simplified as

$$S^{2-} + 2h\nu \rightarrow S + 2e^- \quad (1)$$

Only recently has the emphasis shifted to a pure solution-chemistry investigation of *n*-CdX/S_j^{2-} PECs, leading to some of the highest solar-to-electrical conversion efficiencies in PECs[8] and to the demonstration of the long-term stability of thin-film solar cells[9].

This study presents short-circuit photocurrent, I_{sc}, radiative-to-electrical energy conversion efficiency, η, and fill factor, f_f, reflecting the portion of the attainable power accessed, for a *n*-$CdSe_{0.65}Te_{0.35}$ single-crystal photoelectrode immersed in two series of aqueous caesium polysulphide electrolytes, which are measured using a described experimental procedure[4,8]. Caesium, compared with other polysulphide electrolytes, improves *n*-CdX/S_j^{2-} PEC characteristics[4].

Figures 1 and 2 summarize the photoelectrochemical and chemical conditions in *n*-CdX/S_j^{2-} PECs using a series of polysulphide electrolytes with consistent hydrosulphide activities and varying *p*H. These figures include the calculated complex equilibrium distribution of (poly)sulphide chemical species in these electrolytes. In these solutions, at room temperature, spontaneous polysulphide/thiosulphate disproportionation is not significant. Figure 3 summarizes the photoelectrochemical effects in a second series of polysulphide electrolytes containing a nearly constant environment of tetrasulphide and supersulphide.

As Fig. 1 shows, an electrolyte that tends to shift electrolyte composition away from maximum tetrasulphide and supersulphide activities tends to suppress photocurrent. The close linear proportionality of supersulphide activity with short-circuit photocurrent contrasts strongly with the extreme (exponential) variations of most of the sulphide and polysulphide species in solution in Fig. 2. Depletion of the species to be oxidized below an activity level sufficient to utilize photogenerated holes will reduce *n*-CdX/S_j^{2-} photocurrent. These photocurrent losses will tend to be greatest under conditions of maximum band bending (maximum photocurrents). A chemical species whose activity varies linearly with I_{sc} is closely related to the process of photoinduced oxidation in *n*-CdX/S_j^{2-}.

The importance of the adsorption process in *n*-CdX/S_j^{2-} PECs has been well documented[1,2]. Supersulphide, rather than tetrasulphide, is likely to be the direct oxidation participant due to: (1) the more proportional relation of I_{sc} to supersulphide activity, rather than tetrasulphide activity (see Fig. 1); (2) the higher probability of a one-hole, rather than a two-hole, oxidative process; and (3) comparison of the known temperature dependence of the species distribution in the electrolyte with I_{sc}. *n*-CdX/S_j^{2-} I_{sc} increases smoothly with temperature[10]. Supersulphide displays this smooth increase in activity with temperature[7], whereas the polysulphide formation equilibrium constants are temperature-insensitive[5].

* Present address: Department of Chemistry, Room 6-427, Massachusetts Institute of Technology, Cambridge, Massachusetts 02139, USA.

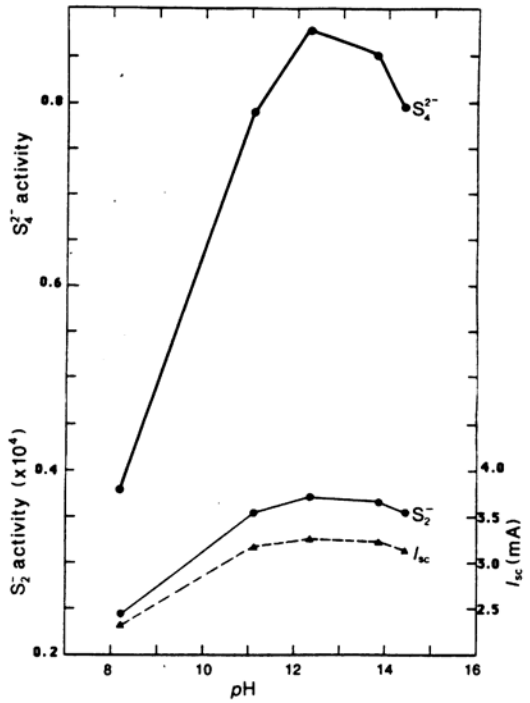

Fig. 1 The variation of supersulphide and tetrasulphide activities and the short-circuit photocurrent I_{sc}, for a 0.15-cm^2 n-$CdSe_{0.65}Te_{0.35}$ single crystal immersed in an aqueous electrolyte containing Cs_2S (1.0 mol per kg H_2O), CsHS (0.8 mol per kg H_2O) and sulphur (3 mol per kg H_2O) at various pH values, under an incident filtered tungsten-halogen illumination of 75 mW cm^{-2}. The crystal was mounted with the (0001) plane exposed, and pretreated with mechanical polishing, chemical etching in aqua regia, rinsing in polysulphide an cyanide solutions to remove excess selenium or tellurium, and photoelectrochemical etching in HCl. A 665-nm cutoff filter eliminated differences in light absorption of polysulphide solutions at shorter wavelengths. The pH was varied from an equilibrium value of 12.35 by addition of either H_2S or CsOH to the solution. Chemical activities were calculated by using equilibrium constants[5,7] at 298 K, in a prescribed manner[6].

Equilibrium concentrations of the supersulphide species are small, $\sim 10^{-5}$ mol kg^{-1} at room temperature, and insufficient to maintain mass transport at the high current densities measured. However, sufficient tetrasulphide will maintain supersulphide activity, preventing supersulphide depletion at the electrode surface and facilitating the adsorption and oxidation of supersulphide on the surface, M:

$$S_{4\,(aq)}^{2-} \rightleftharpoons 2S_{2\,(aq)}^{-} \quad K = (a_{s_2^-})^2 (a_{s_4^{2-}})^{-1} = 2.6 \times 10^6 \cdot 10^{-4{,}533/T(K)} \qquad (2)$$

$$S_{2\,(aq)}^{-} + M \rightleftharpoons S_{2\,(ad)}^{-} \cdot M \qquad (3)$$

$$S_{2\,(ad)}^{-} \cdot M + h^+ \rightarrow S_2 \cdot M \qquad (4)$$

In Fig. 3 the nearly constant I_{sc} is again consistent with a constant S_2^- activity, as in equations (3, 4).

Other data appear consistent with the process proposed in equations (2-4). Tetrasulphide was an important participant in n-CdX/$S_{j\,(aq)}^{2-}$ oxidative processes[11-13]. Loss of polysulphide in solution by disproportionation resulted in PECs of lowered efficiency[6,9]. Hamilton and Woods[14] provided evidence for an adsorbed species containing two sulphur atoms, tentatively identified as disulphide, S_2^{2-}, as active in the electrochemical oxidation of sulphide on gold. Lessner *et al.*[15] suggested that supersulphide was a direct participant in the oxidation of polysulphide on cobalt, but their analysis incorrectly excluded adsorptive processes from their model[16].

A significant increase in f_f, to >0.5, parallels increases in

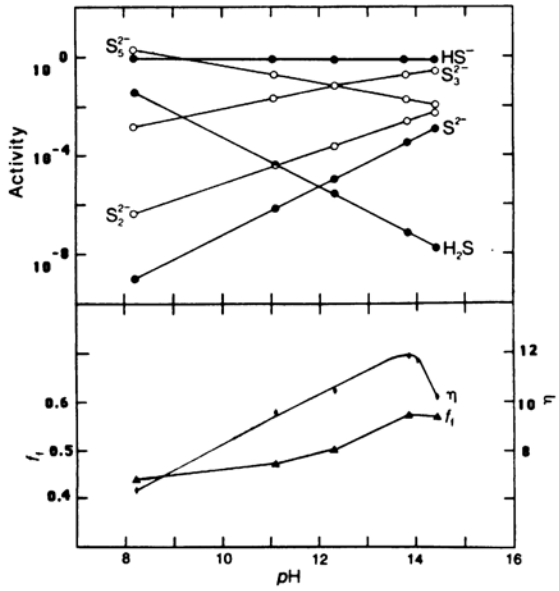

Fig. 2 The variation of fill factor, f_f, solar-electrical conversion efficiency, η, and the distribution of chemical species for a 0.15-cm^2 n-$CdSe_{0.65}Te_{0.35}$ single crystal prepared and measured under the conditions described in the legend to Fig. 1. The polysulphide data are shown as open circles, and the hydrogen sulphide, hydrosulphide and sulphide data are shown as solid circles.

hydroxide, disulphide and trisulphide activities (Fig. 2) and hydroxide and hydrosulphide activity (Fig. 3). The depletion of supersulphide activity has a primary effect on photocurrent (Fig. 1) with no relation to the diminishing f_f seen in Figs 2 and 3. Large f_f are maintained only at hydrosulphide and hydroxide activities >0.5.

At maximum PEC power, band bending is intermediate between the flat band potential and the strong conduction and valence-band bending occurring at I_{sc}. The electrical gradient accelerating holes to the electrode surface is smaller at maximum power than at I_{sc}. As Fig. 3 shows, supersulphide activities are consistently sufficient to maintain high photocurrents. Despite this availability of reductant, the less-reactive holes occurring at maximum power will have a lower probability of favourable (non-corrosive) reaction if the oxidation product tends to accumulate at the electrode surface. As shown, hydroxide and hydrosulphide depletions have a strong effect on f_f, measured at this point of maximum power. This is symptomatic of the different mechanistic roles of supersulphide compared with hydroxide, hydrosulphide and the shorter polysulphide species. The latter species are not directly connected with photocurrent magnitude, but are related to a desorption-dissolution role of these species in the overall oxidative process, according to:

$$S_2 \cdot M + S_{(j-1)\,(aq)}^{2-} \rightleftharpoons S_{(j+1)\,(aq)}^{2-} + M \qquad (5)$$

$$(j-1)S_{(j+1)\,(aq)}^{2-} + HS^- + OH^- \rightleftharpoons jS_{j\,(aq)}^{2-} + H_2O \qquad (6)$$

The various polysulphides, $S_{(j-1)\,(aq)}^{2-}$, will tend to dissolve sulphur (equation (5)). However, a build-up in concentration of the longer polysulphide species will tend to suppress the rate of sulphur dissolution from the surface. This is minimized by the re-equilibration to shorter polysulphide species through equation (6). The sensitive role of hydroxide should be noted. At pH <13 hydroxide depletion retards sulphur dissolution, and f_f is diminished (Fig. 2). But at pH >14, tetrasulphide decreases (Fig. 1) as di- and trisulphide activities dominate[11-13]. This can impose mass-transport limitations on the photocurrent (equations (2-4)).

Cahen *et al.*[17] observed that aqueous electrolytes, which enhance the dissolution of elemental sulphur, enhance photo-

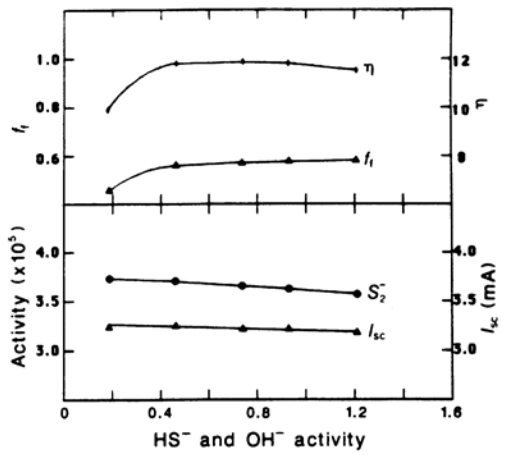

Fig. 3 The short-circuit photocurrent, I_{sc}, solar-electrical conversion efficiency, η, and fill factor, f_f, compared with supersulphide and hydrosulphide (equal to hydroxide) activities, for a 0.15-cm² n-$CdSe_{0.65}Te_{0.35}$ single crystal immersed in aqueous electrolytes containing sulphur (3 mol per kg H_2O) and Cs_2S (1.0–2.3 mol per kg H_2O), under an incident illumination of 75 mW cm^{-2}. Further measurement and calculation details are desribed in the legend to Fig. 1.

electrochemical effects in $CdX/S^{2-}_{j\,(aq)}$ PECs. Moreover, the dissolution of an activated sulphur was related to the presence of hydroxide and hydrosulphide[18] although inconsistencies arose in the analysis of the role of hydroxide and sulphide[19,20].

Now equations (2–6) are incorporated into an overall mechanism for the action of $CdX/S^{2-}_{j\,(aq)}$ PECs. In both dark and photoactive environments $Cd(S_x, Se_y, Te_z)$ materials, when immersed in polysulphide electrolytes, exchange with sulphur at the surface[1,2]

$$CdX_{surface} + S^{2-}_{(j+1)(aq)} \rightarrow CdS_{surface} + XS^{2-}_{j\,(aq)} \quad (7)$$

The resultant CdS surface provides stable sites for photooxidation, and must act as a window for photon absorption in the band-gap optimized space-charge region of the semiconductor, CdX_{sc}. Illumination results in useful electrical work and/or chemical fuel production, described here by the following primary process, including equilibration and adsorption of supersulphide,

$$S^{2-}_{4\,(aq)} \rightleftharpoons 2S^{-}_{2\,(aq)} \quad (8)$$

$$S^{-}_{2\,(aq)} + CdS_{surface}\cdot\cdot CdX_{sc}\cdot\cdot CdX_{bulk} \rightleftharpoons S^{-}_{2\,(ad)}\cdot CdS_{surface}\cdot\cdot CdX_{sc}\cdot\cdot CdX_{bulk} \quad (9)$$

photoexcitation and separation of electron-hole pair, within the semiconductor,

$$S^{-}_{2\,(ad)}\cdot CdS_{surface}\cdot\cdot CdX_{sc}\cdot\cdot CdX_{bulk} + h\nu \rightarrow S^{-}_{2\,(ad)}\cdot CdS_{surface}\cdot\cdot CdX_{sc}(h^+\cdot e^-)\cdot\cdot CdX_{bulk} \quad (10)$$

$$S^{-}_{2\,(ad)}\cdot CdS_{surface}\cdot\cdot CdX_{sc}(h^+\cdot e^-)\cdot\cdot CdX_{bulk} \rightarrow S^{-}_{2\,(ad)}\cdot CdS_{surface}(h^+)\cdot\cdot CdX_{sc}\cdot\cdot CdX_{bulk}(e^-) \quad (11)$$

supersulphide oxidation and external work,

$$S^{-}_{2\,(ad)}\cdot CdS_{surface}(h^+)\cdot\cdot CdX_{sc}\cdot\cdot CdX_{bulk}(e^-) \rightarrow S_2\cdot CdS_{surface}\cdot\cdot CdX_{sc}\cdot\cdot CdX_{bulk} + e^-_{external} \quad (12)$$

charge balance by reduction at a counter electrode involving either polysulphide reduction, a chemical product or fuel production[21], or electrochemical storage[3,22],

$$e^-_{external} + R \rightarrow R^- \quad (13)$$

and dissolution of sulphur enhanced by re-equilibration to shorter polysulphides,

$$S_2\cdot CdS_{surface}\cdot\cdot CdX_{sc}\cdot\cdot CdX_{bulk} + S^{2-}_{(j-1)\,(aq)} \rightleftharpoons S^{2-}_{(j+1)\,(aq)} + CdS_{surface}\cdot\cdot CdX_{sc}\cdot\cdot CdX_{bulk} \quad (14)$$

$$(j-1)S^{2-}_{(j+1)\,(aq)} + HS^- + OH^- \rightleftharpoons jS^{2-}_{j\,(aq)} + H_2O \quad (15)$$

Processes deleterious to continued photooxidation can be consistently described as adverse to the overall mechanism for the action of $CdX/S^{2-}_{j\,(aq)}$ PECs presented in equations (7–15). These include polysulphide disproportionation[6], which will remove polysulphide from solution,

$$S^{2-}_5 + 3OH^- \rightarrow S_2O^{2-}_3 + 3HS^- \quad (16)$$

a shift of the polysulphide equilibrium away from tetrasulphide[11–13],

$$4S^{2-}_{4\,(aq)} + H_2O \rightleftharpoons 3S^{2-}_{5\,(aq)} + HS^- + OH^- \quad (17)$$

$$2S^{2-}_{4\,(aq)} + HS^- + OH^- \rightleftharpoons 3S^{2-}_{3\,(aq)} + H_2O \quad (18)$$

$$3S^{2-}_{3\,(aq)} + HS^- + OH^- \rightleftharpoons 2S^{2-}_{2\,(aq)} + H_2O \quad (19)$$

or the enhancement of supersulphide desorption,

$$S^{-}_{2\,(ad)}\cdot CdS_{surface}\cdot\cdot CdX_{sc}\cdot\cdot CdX_{bulk} \rightarrow S^{-}_{2\,(aq)} + CdS_{surface}\cdot\cdot CdX_{sc}\cdot\cdot CdX_{bulk} \quad (20)$$

electron–hole pair recombination[23],

$$S^{-}_{2\,(ad)}\cdot CdS_{surface}\cdot\cdot CdX_{sc}(h^+\cdot e^-)\cdot\cdot CdX_{bulk} \rightarrow S^{-}_{2\,(ad)}\cdot CdS_{surface}\cdot\cdot CdX_{sc}\cdot\cdot CdX_{bulk} + \text{heat} \quad (21)$$

photo-induced corrosion of the semiconductor[24],

$$CdX + 2h^+ \rightleftharpoons Cd^{2+}{}_{(aq)} + X \quad (22)$$

increased dark reactions, indicative of reduction at the semiconductor surface,

$$S_2\cdot CdS_{surface}\cdot\cdot CdX_{sc}\cdot\cdot CdX_{bulk} \rightarrow S^{-}_{2\,(ad)}\cdot CdS_{surface}(h^+)\cdot\cdot CdX_{sc}\cdot\cdot CdX_{bulk} \quad (23)$$

or reduction at an alternative material, M, with access to both semiconductor and electrolyte,

$$S_2\cdot M + e^- \rightarrow S^{-}_{2\,(ad)}\cdot M \quad (24)$$

and competition to sulphur dissolution, related to depletion of shorter polsulphide species,

$$S^{2-}_{(j+1)\,(aq)} + CdS_{surface} \rightarrow S_2\cdot CdS_{surface} + S^{2-}_{(j-1)\,(aq)} \quad (25)$$

$$jS^{2-}_{j\,(aq)} + H_2O \rightarrow (j-1)S^{2-}_{(j+1)\,(aq)} + HS^- + OH^- \quad (26)$$

This study emphasizes the need for an understanding of solution-chemistry effects in interpreting photoelectrochemical systems. Determination of the reactive chemical species and relevant chemical steps for energy conversion in n-CdX/S^{2-}_j PECs, demonstrated here, can be applied to create more accurate modelling of these and other liquid solar cells[20,23,25–27].

I thank R. Tenne, Weizmann Institute, Rehovot, Israel, and R. Triboulet and C. Levy-Clement, Laboratoire de Physique de Solides, Meudon, France, for providing crystals.

Received 26 May; accepted 20 August 1987.

1. Hodes, G. in *Energy Resources through Photochemistry and Catalysis* (ed. Gratzel, M.) 421–465 (Academic, New York, 1983).
2. Hodes, G., Fonash, S. J., Heller, A. & Miller, B. in *Advances in Electrochemistry and Electrochemical Engineering* Vol. 13 (ed. Gerischer, H.) 113B–158B (Wiley, New York, 1985).
3. Licht, S., Hodes, G., Tenne, R. & Manassen, J. *Nature* **326**, 863–864 (1987).
4. Licht, S., Tenne, R., Flaisher, H. & Manassen, J. *J. electrochem. Soc.* **133**, 52–59 (1986).
5. Giggenbach, W. *Inorg. Chem.* **13**, 1724–1730 (1974).
6. Licht, S., Hodes, G. & Manassen, J. *Inorg. Chem.* **25**, 2486–2489 (1986).
7. Giggenbach, W. *Inorg. Chem.* **10**, 1306–1308 (1971).
8. Licht, S. *et al. Appl. Phys. Lett.* **46**, 608–610 (1985).
9. Licht, S. *J. phys. Chem.* **90**, 1096–1099 (1986).
10. Muller, N. & Cahen, D. *Solar Cells* **9**, 229–245 (1983).

11. Licht, S. & Manassen, J. *J. electrochem. Soc.* **132,** 1076–1081 (1985).
12. Licht, S., Manassen, J. & Hodes, G. *J. electrochem. Soc.* **133,** 272–277 (1986).
13. Licht, S. & Manassen, J. *J. electrochem. Soc.* **133,** 277–280 (1986).
14. Hamilton, I. C. & Woods, R. *J. appl. Electrochem.* **13,** 783–794 (1983).
15. Lessner, P., Winnick, J., McLarnon, F. R. & Cairns, E. J. *J. electrochem. Soc.* **133,** 2517–2522 (1986).
16. Licht, S. *J. electrochem. Soc.* **134,** (in the press).
17. Lando, D., Manassen, J., Hodes, G. & Cahen, D. *J. Am. chem. Soc.* **101,** 3969–3971 (1979).
18. Frese, K. W. Jr & Canfield, D. G. *J. electrochem. Soc.* **131,** 2614–2618 (1984).
19. Licht, S. *J. electrochem. Soc.* **132,** 2801–2802 (1985).
20. Licht, S. & Marcu, V. *J. electroanalyt. Chem.* **210,** 197–204 (1982).
21. Smotkin, E. S. *et al. J. phys. Chem.* **91,** 6–8 (1987).
22. Bratin, P. & Tomkiewicz, M. *J. electrochem. Soc.* **129,** 2469–2473 (1982).
23. Flaisher, H. & Tenne, R. *J. phys. Chem.* **87,** 3061–3068 (1983).
24. Marcu, V., Tenne, R. & Rubinstein, I. *J. electrochem. Soc.* **133,** 1143–1148 (1986).
25. Orazem, M. E. & Newman, J. *J. electrochem. Soc.* **131,** 2569–2574 (1984).
26. Orazem, M. E. & Newman, J. *J. electrochem. Soc.* **131,** 2574–2582 (1984).
27. Benito, R. M. & Nozik, A. J. *J. phys. Chem.* **89,** 3429–3434 (1985).